Atomic-scale structure and surface reactions of water and ammonia on ruthenium

Dissertation

Ingeborg Staß

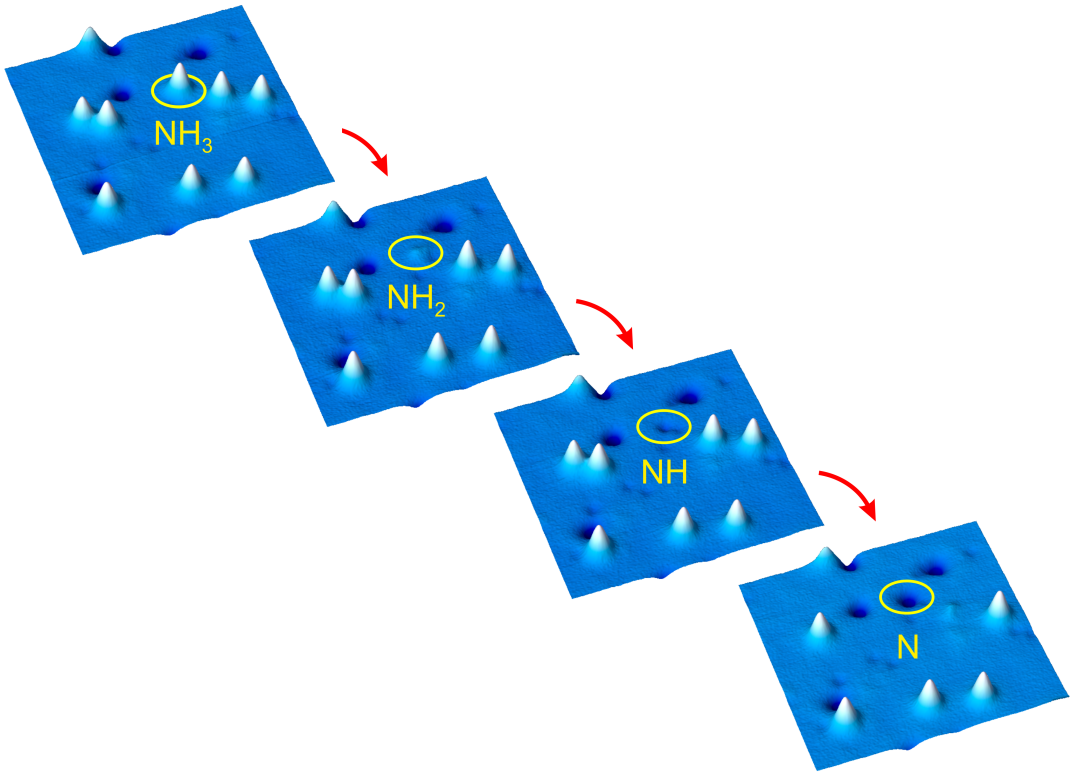

submitted to
Fachbereich Physik
Freie Universität Berlin

May 2010

Diese Arbeit wurde in der Arbeitsgruppe von Prof. Dr. José Ignacio Pascual am Fachbereich Physik der Freien Universität Berlin angefertigt. Die Experimente wurden in der Gruppe von Prof. Dr. Miquel Salmeron am Lawrence Berkeley National Laboratory in Berkeley, Kalifornien (USA) durchgeführt.

Erstgutachter: Prof. Dr. José Ignacio Pascual
Zweitgutachter: Prof. Dr. Wolfgang Kuch

Datum der Disputation: 14. Juli 2010

Contents

Kurzfassung

In dieser Arbeit werden Einzelmolekül-Chemie an Ammoniak sowie Wasserbenetzung und Eiswachstum auf reinem und beschichtetem Ru(0001) mittels Rastertunnelmikroskopie durchgeführt.

Ein einzelnes Ammoniak-Molekül wird Schritt für Schritt in einem Tunnelkontakt dehydrogenisiert, d.h. NH_2, NH und N werden auf Ruthenium generiert und die Adsorptionsplätze von NH_3 und N bestimmt. Außerdem werden Komplexe aus NH_3, die von bis zu drei Wasserstoff-Atomen umgeben sind, beobachtet und Anzeichen für Formierung und Spaltung von Ammoniak-Dimeren erhalten. Die Experimente deuten darauf hin, dass die Dehydrogenisierung durch einen elektrischen Feld-Effekt geschieht. Unterschiedliche Feldstärken sind zum Überwinden der Dissoziations-Schwelle notwendig, je nach angelegter Spannungs-Polarität zwischen Spitze und Probe. Dichtefunktionaltheoretische Berechnungen in Kombination mit Moleküldynamik-Simulationen ergeben, dass eine Erhöhung des elektrischen Feldes bei positiver Probenspannung ein Aufweichen der Inversions-Mode von Ammoniak induziert. Dies führt zu einer verstärkten Oberflächen-Molekül-Wechselwirkung und einem Aufweiten der H-N-H Winkel, was letztlich die Dissoziierung bewirkt. Negative Polarität verursacht eine Verringerung der Oberflächen-Molekül-Wechselwirkung durch ein Aufweichen der N-Ru-Streckschwingung. Desorption des Moleküls ergibt sich für kleine negative Felder, hingegen wird Dissoziierung erst bei größeren Feldern ermöglicht.

Wasserbenetzung und Eiswachstum werden auf reinem Ru(0001) zwischen 110 und 145 K charakterisiert. Die erste Lage bildet oberhalb von 130 K gemischte Wasser-Hydroxyl-Cluster, welche sich unterscheidbar auf der Oberfläche ausrichten. Die bei der partiellen Dissoziiering freigesetzten Wasserstoff-Atome bilden eine geordnete Struktur zwischen den und innerhalb der Wasser-Hydroxyl-Cluster. Überraschenderweise sind die Hexamere der zweiten Wasserlage 30° rotiert relativ zur ersten, was Wechselwirkungen suggeriert, die nicht auf Wasserstoff-Brückenbindungen basieren. Jenseits der zweiten Lage tritt Wachstum von kompakten Eis-Clustern auf.

Die Adsorption von Wasser auf O(2x1)-bedecktem Ru(0001) führt zu einer wohlgeordneten (4x2) Überstruktur oberhalb von 140 K. Der erwartete hydrophobe Charakter der O(2x1)-Oberfläche wird während der Wasser-Adsorption stark modifiziert aufgrund struktureller Veränderungen der Sauerstoff-Lage, und eine Benetzungs-Schicht wird beobachtet. Die durch die Wasser-Adsorption hervorgerufene Sauerstoff-Wabenstruktur bleibt metastabil, nachdem das Wasser desorbiert ist, und sie kehrt bis nahe 260 K nicht in die stabile lineare 2x1-Struktur zurück.

Bei Graphen-Wachstum durch Ru-Stufen-Ätzen werden die geätzten Ru-Atome unter die Graphen-Schicht injiziert. Eine geringe Konzentration injizierter Ru-Atome bewirkt Versetzungs-Netzwerke in der Ru-Schicht unter dem Graphen. Wasser adsorbiert anfangs an den Grenzen der dreiecksförmigen Überstruktur. Größere Wasser-Bedeckungen führen zu erhöhtem Wachstum zum Zentrum der Dreiecke hin. Ein Trend zu vollständiger Benetzung wird festgestellt.

Abstract

In this thesis, single-molecule ammonia chemistry as well as water wetting and ice growth on pristine and precovered Ru(0001) are investigated by scanning tunneling microscopy (STM).

An individual ammonia molecule is successively dehydrogenated within the STM junction, thus NH_2, NH and N are generated on ruthenium, and the adsorption sites of NH_3 and N are determined. Besides, complexes of NH_3 surrounded by up to three hydrogen atoms are observed, and indication for ammonia dimer formation and splitting obtained.

The experiments suggest that dehydrogenation occurs due to electric-field effects. Different electric-field strengths are required to overcome the dissociation threshold, depending on the bias polarity that is applied between tip and sample. Density functional theory calculations in combination with molecular dynamics simulations find that the increasing electric field of a positively biased sample induces softening of the ammonia's umbrella mode, resulting in an enhanced molecule-surface interaction and widening of the H-N-H angles, which eventually causes dissociation. Negative polarity leads to a decrease in molecule-surface interaction by softening of the N-Ru stretch mode. This triggers desorption of the molecule at smaller fields, whereas dissociation becomes favorable at larger fields.

Water wetting and ice growth are characterized on pristine Ru(0001) between 110 and 145 K. The first layer forms mixed water-hydroxyl clusters above 130 K, exhibiting a distinct alignment on the surface. Hydrogen atoms, liberated due to partial dissociation, form an ordered structure between and inside the water-hydroxyl clusters. Surprisingly, the second-layer water hexamers are rotated by 30° relative to the first layer, suggesting non-H-bonding interactions between first and second layer. Beyond the second layer, growth of compact ice clusters occurs.

Water adsorption on Ru(0001) precovered by O(2x1) induces a well-ordered (4x2) superstructure at temperatures of 140 K. The expected hydrophobic character of the O-(2x1) covered surface is strongly modified during water adsorption due to structural changes of the O adlayer, and a wetting layer is observed. The oxygen honeycomb structure induced by the adsorption of water remains metastable after water desorption and does not revert to the stable linear 2x1 structure until temperatures close to 260 K.

Graphene growth by Ru step etching injects the etched Ru atoms under the graphene sheet. Low concentration of injected Ru atoms induces dislocation networks in the Ru layer underneath the graphene. Water initially adsorbs at the boundaries of the triangular dislocation superstructure. Larger coverages lead to enhanced water growth towards the centers of the triangles. A trend towards complete surface wetting is observed.

Introduction

> *Gentlemen, in a letter on an oeconomical constant battery which you did me the honour to publish in your number for the present month [...] I ventured to suggest the more extensive employment of the porous septum as an instrument of analysis for voltaic combinations. [...] The following experiments instituted with this view may not be uninteresting to your readers; [...] solutions separated by a diaphragm and connected by platinum plates. [...] The same sheets of platinum were exposed to atmospheres of common air and of similar gases, i.e. both to oxygen or both to hydrogen, but without affecting the galvanometer. The platinum in the hydrogen was made the positive, and that in the oxygen the negative electrode of a* single *voltaic pair, the water now rose [...] in the hydrogen tube and proportionally in the oxygen. I hope by repeating this experiment in series, to effect decomposition of water by means of its composition. – W. R. Grove (1839)* [Gro39]

In an environmentally sustainable world, zero-carbon-emission solutions need to replace conventional fossil fuel technologies. Nowadays transportation accounts for huge amounts of nocuous CO_2 emission into the atmosphere. One may thus want to seek that "in the twenty-first century, transportation – cars, trains and ships – will all be driven by electric motors powered by electricity derived from fuel cells" [Boc00]. Both water (H_2O) and ammonia (NH_3) constitute potential energy carriers for fuel cells within a hydrogen economy. While two third of the earth's surface is covered by water, ammonia is cheap and abundant as well, and offers a 45 % higher volumetric hydrogen density than liquid hydrogen. The latter is of crucial importance when choosing the adequate material as an energy carrier for *on-board* vehicular hydrogen storage, and becomes even more appealing when realizing that no greenhouse gases are emitted upon ammonia decomposition [Kle08].

In order to decipher the reaction mechanisms that lead to the desired hydrogen abstraction, an atomic-scale understanding of catalytic processes is required. This essentially means for us that we have to take the nano road towards the hydrogen highway.

Yet water is way more than a hydrogen carrier. It is the 'matrix of life', central to Earth and atmospheric sciences and many technologies – and no one really understands it [Bal08]. In its liquid phase a random, fluctuating, three-dimensional network of hydrogen bonds holds it together [Bal03]. In contrast, crystalline ice is governed by fixed hydrogen bonds whose arrangement features distinct phases. The first layer of adsorbed water molecules at a surface thus sets the course as a structural template that guides ice growth and mediates aqueous interfacial chemistry [Fei10].

In this context, hydrogen abstraction reactions and water wetting in conjunction with ice growth on the catalytic Ru(0001) surface are addressed in this thesis. Scanning tunneling microscopy (STM) at low temperatures and under ultra-high vacuum

(UHV) provides the ideal setting to investigate the fundamental mechanisms of these phenomena, as STM accomplishes spatial resolution on the atomic scale paired with the ability to manipulate matter atom-by-atom. Due to the extreme vacuum and temperature conditions, perturbing effects like surface contamination and diffusion processes of the adsorbates can be controlled.

Our first scope is the reaction mechanism for ammonia decomposition over the Ru surface at the single-molecule scale. The goal is a controlled and successive dehydrogenation of a single ammonia molecule by STM manipulation, i.e., the step-wise generation of NH_2, NH and N, respectively, and their identification by adsorption site and image simulations. Besides, complexes of ammonia and hydrogen as well as ammonia dimers are formed, and their adsorption configuration is determined.

To obtain an understanding of the underlying processes that cause ammonia dehydrogenation, we study by STM jointly with density functional theory (DFT) calculations and molecular dynamics (MD) simulations the effect that an electric field imposes on an ammonia molecule within the STM junction. We find that different electric-field strengths are required to overcome the dissociation threshold, depending on the bias polarity that is applied between tip and sample. This is reflected in distinct reaction mechanisms. Increasing electric fields induce a geometrical instability of the adsorbed ammonia, leading to a softening of certain vibrational modes of the molecule and ultimately triggering processes like dissociation and desorption.

Secondly, we are interested in the interactions of water with surfaces and with itself. Water growth on precious metal surfaces may or may not involve partial dissociation of the water molecules. Here we observe intact as well as mixed water-hydroxyl clusters on ruthenium, depending on annealing temperature and duration, and we assign their adsorption geometry.

Another aspect that we investigate is the question whether an ice-like wetting layer exists. Unexpectedly, we find the second water layer's hexamers rotated by 30° relative to the first layer, a fact that has not been observed for any phase of ice. Such an arrangement of water molecules does not seem to favor hydrogen-bonding between the two layers. Similar weak bonding configurations are likely in bulk water, where thermal agitation disrupts the tetrahedral structure. Beyond the second water layer, ice nucleation is observed. We imaged clusters, several layers in height, on top of an incomplete first and second layer.

Most metal surfaces are covered by an oxide film and a water layer at ambient conditions. Since chemisorbed oxygen on metal surfaces forms well-ordered and atomically flat overlayers, this kind of surface can be used to study the initial interaction of water molecules with surface oxygen. We investigate whether or not wetting occurs on Ru(0001) precovered by O(2x1). While the O(2x1) surface is supposed to be hydrophobic, we find the O adlayer strongly modified upon water adsorption, which enables surface wetting.

A material that is less delicate at ambient conditions than atomically clean ruthenium, is Ru precovered by graphene. We observe that a particular graphene growth mode by Ru step etching leads to intercalated Ru atoms, creating unique dislocation networks. When exposing the reconstructed surface to water, we find that water wetting starts at the boundaries of the triangular dislocation network and grows towards the centers of the triangles at larger coverages.

1 Introduction to scanning tunneling microscopy

In this chapter I am going to introduce both experimental as well as theoretical concepts of scanning tunneling microscopy (STM). I start with a brief description of the principles behind STM, followed by an overview of several approaches to theoretically describe this technique. Then the setup as it was used for experiments is presented in detail, and an introduction into the investigated surfaces, adsorbates and the manipulation mechanisms by STM is given.

In 1986 Gerd Binnig and Heinrich Rohrer were awarded the Nobel Prize in Physics for inventing the scanning tunneling microscope that enabled imaging a surface with atomic resolution in real space for the first time [Bin82, Bin82b, Bin83].

Scanning tunneling microscopy is based on the quantummechanical tunneling effect. It is operated by placing a conductive tip over a conductive surface, a few Ångstrøm apart, and applying a voltage on the order of 1 V. There is a potential barrier present that is higher than the electron energy due to the non-zero distance or vacuum between tip and sample, but yet the (exponentially decaying) wave functions of tip and surface do overlap and give rise to a certain tunneling probability, such that a tiny current on the order of pA or nA can be detected. Decreasing the tip-sample distance by 1 Å leads to a tunneling current approximately one order of magnitude larger.

In *constant-current* mode (as opposed to *constant-height* mode), an image is obtained by scanning the surface line by line such that a constant current is kept, i.e., by controlling the height of the tip over the surface, see Fig. 1.1. Tip height as a function of position on the sample generates an image which represents basically the topography of the surface. To be more precise, the tip is kept at a contour of constant local density of states (LDOS), close to the Fermi energy, see section 1.1.3.

The tip is driven in x-, y- and z-direction by piezoelectric crystals that deform mechanically (extending or contracting) dependig on the applied voltage. It is not the piezo crystals that limit the resolution, but mechanical and electronic oscillations and noise. Low temperatures are favorable as they prevent diffusion as well as the setup itself from drifting significantly.

1.1 Theoretical concepts

STM is based on the quantummechanical tunneling effect, i.e., the probability for electrons to tunnel through a potential barrier that cannot be overcome by the laws that govern classical physics. A few approaches to describe such a metal-vacuum-metal contact are presented in the following, starting with the one-dimensional potential barrier, and including Bardeen and Tersoff-Hamann theory. A brief introduction into density functional theory is also added.

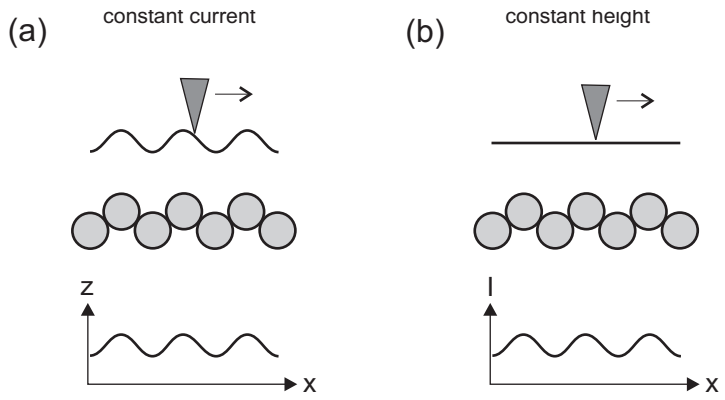

Figure 1.1: (a) In constant-current mode, the height of the STM tip is recorded relative to the surface, while keeping the tunneling current constant. (b) One can also obtain an equivalent image by keeping the height constant and measuring the current (constant-height mode).

1.1.1 One-dimensional model for tunneling

The easiest way to describe a one-dimensional potential barrier is by taking a barrier as shown in Fig. 2.14. Considering the electrons of a metal as moving freely, they can be desccribed by plane waves.

Solving the stationary Schrödinger-equation for this particular potential is standard in quantum mechanics (see also [Fow28]).The transmission coefficient represents the probability for an electron to tunnel through the potential barrier, and is proportional to the tunneling current.

$$I \sim T \sim \exp(-2\kappa d) \tag{1.1}$$

d being the distance between the electrodes and

$$\kappa = \hbar^{-1}\sqrt{2m_e\Phi} = const \tag{1.2}$$

Φ is the work function of the electrodes and m_e the electron mass [Han87, Sch98]. I decays exponentially with rising distance between the metals. Considering a typical work function for a metal of $\Phi = 4 - 5$ eV, the current drops by one order of magnitude, if the distance between electrodes is increased by 1 Å. This strong coupling of tunneling current and distance is crucial for STM: Tiny variations in tip height are detected and guarantee excellent spatial resolution [Han87].

Introducing the Fermi energy E_F, the above model can be extended. E_F is the energy of the highest occupied electron state in the metal. In Fig. 1.3 the metal electrodes are now replaced by tip and sample. If they are made out of different materials, they have different work functions as well. For large tip-sample distances, there is no tunneling current, see Fig. 1.3 (a). By approaching the two electrodes to one another, tunneling contact is created and the two Fermi levels equal, while shifting vacuum potentials, see Fig. 1.3 (b). Now, a voltage is applied between tip and sample, and thus their Fermi levels shift with respect to each other such that electrons tunnel from occupied tip states into unoccupied states of the sample, see Fig. 1.3 (c) [Wie94].

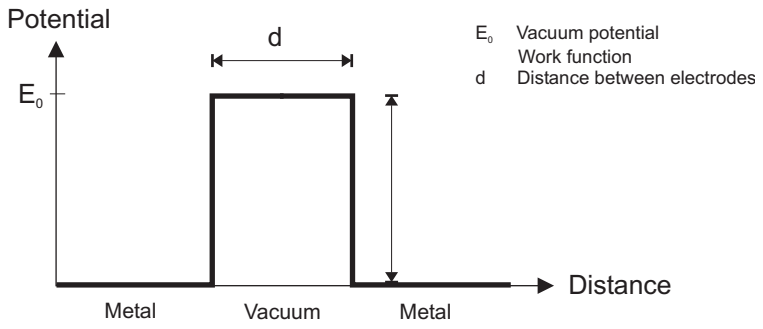

Figure 1.2: Simple representation of the potential for a metal-vacuum-metal junction in order to calculate the resulting tunneling current.

1.1.2 Bardeen's approach

Inspired by the tunneling current that had passed a thin oxide layer, separating two metals [Gia60, Gia60b], Bardeen calculated the tunneling probability, regardless of the dimension in 1961 [Bar61]. Bardeen's approach is to bring the two metals into tunneling contact at time t_0, i.e., by turning on a constant perturbation potential V. The Hamiltonian H_0 of the unperturbed system is now modified into $H = H_0 + V$ for $t \geq t_0$, and $V \ll H_0$ is assumed, i.e., the perturbation is small. First-order time-dependent perturbation theory leads to Fermi's Golden Rule for the transmission amplitude (tunneling matrix element) $M_{\mu\nu}$, with $|M_{\mu\nu}|^2$ proportional to the transition probability of the unperturbed state ψ_μ of one electrode to the unperturbed state ψ_ν of the other. This results in

$$M_{\mu\nu} = -\frac{\hbar^2}{2m} \int_S (\psi_\mu^* \bigtriangledown \psi_\nu - \psi_\nu \bigtriangledown \psi_\mu^*) \, \mathrm{d}\tau. \tag{1.3}$$

Conservation of energy of the tunneling electrons was assumed, too, i.e., $E_\mu = E_\nu$, for E_μ the energy corresponding to ψ_μ. The integral is over any plane S in the barrier region, that is passed by the total tunneling current. [Han87, Sch98]. To calculate the tunneling current (in one direction), $|M_{\mu\nu}|^2$ has to be multiplied by the average occupancy of ψ_μ of one electrode and the average non-occupancy of ψ_ν (of the other electrode) by using their Fermi functions, as electrons tunnel from occupied into unoccupied states. Summing over all remaining states, while accounting for conservation of energy for the electrons, gives rise to

$$I = \frac{2\pi e}{\hbar} \sum_{\mu\nu} f(E_\mu) \left[1 - f(E_\nu + eU)\right] |M_{\mu\nu}|^2 \, \delta(E_\mu - E_\nu). \tag{1.4}$$

U is the applied bias and f the Fermi function. Taking the limits of low temperature and small bias voltage ($U \leq 10$ meV), this equation transforms into [Ter83]

$$I = \frac{2\pi}{\hbar} e^2 U \sum_{\mu\nu} |M_{\mu\nu}|^2 \, \delta(E_\nu - E_F) \, \delta(E_\mu - E_F). \tag{1.5}$$

1.1.3 Formalism by Tersoff and Hamann

A first quantitative theory of Scanning tunneling microscopy was provided by Tersoff and Hamann in 1983 [Ter83]. Tunneling through vacuum is realized between a real

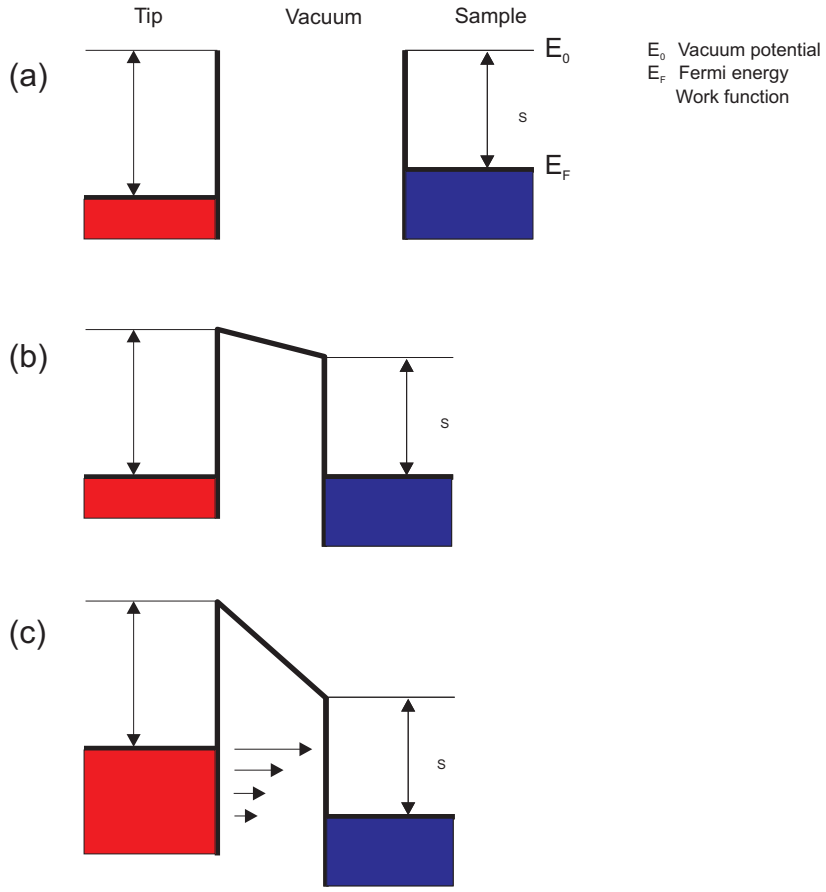

Figure 1.3: Energy diagram for tip and sample for the case of a one-dimensional potential [Wie94]. (a) Large tip-sample distances do not lead to a tunneling contact, (b) a tunneling contact has been established, (c) applying a voltage finally leads to tunneling electrons.

surface and a model tip that terminates in a locally spherical apex, see Fig. 1.4.

To calculate $M_{\mu\nu}$ for the given boundary conditions, the wave functions ψ_μ of tip and ψ_ν of surface need to be specified. Mathematically ψ_ν can be expanded into wave functions, propagating parallel to the surface and decaying exponentially normal to it. ψ_μ is approximated towards the surface as being s-like. The work function for tip and sample is assumed to be equal. Inserted into Bardeen's equation (Glg. 1.3), this leads to

$$M_{\mu\nu} \sim \psi_\nu(\vec{r_0}) \tag{1.6}$$

with $\vec{r_0}$ defined as in Fig. 1.4. Thus, by using equation 1.5

$$I \sim U\ D_S(E_F) \sum_\nu |\psi_\nu(\vec{r_0})|^2\, \delta(E_\nu - E_F) \tag{1.7}$$

with $D_S(E_F)$ the density of states per unit volume of the tip at E_F. Defining

$$\rho(\vec{r_0}, E_F) \equiv \sum_\nu |\psi_\nu(\vec{r_0})|^2\, \delta(E_\nu - E_F) \tag{1.8}$$

the local density of states (LDOS) of the surface at E_F at the position of the tip, hence

$$I \sim U\ D_S(E_F)\ \rho(\vec{r_0}, E_F)\,. \tag{1.9}$$

For low temperatures and small voltages ($U \leq$10 meV) STM accordingly measures contours of constant surface LDOS [Ter85]. Note that I not just depends on the tip-sample distance d (see chapter 1.1.1), which would correspond to a topographical image, but rather the surface LDOS is the the relevant parameter here. Remember that Tersoff and Hamann only considered s-like wave functions. For larger R (see Fig. 1.4), this model is thus less suited. However, as long as the tip is built from a single atom or a small amount of atoms with well-defined center $\vec{r_0}$, this formalism is adequate [Han87]. By choosing ψ_ν and typical values for the constants in equation 1.7, one can estimate for small voltages

$$I \sim \exp(-2\kappa d),$$

which is the same result as suggested by equation 1.1.

If molecular adsorbates are involved, Tersoff-Hamann theory cannot be applied. For one reason, there is the assumption of a weak interaction between tip and sample which is not necessarily given in the presence of an adsorbate. In addition, when assuming the tip being formed by a small amount of atoms, the lateral interactions between tip and adsorbate are taken into account unsufficiently. Instead molecular orbital calculations of the charge distributions of free molecular states close to the Fermi level were presented [Lip89], while using Hückel's method, see [Hak94]. However, the approach to look at free molecules, is pretty rough. Yet another Ansatz takes the *Jellium* model as well as Bardeen's formalism, and assumes tip and sample as planar metal electrodes with a chemisorbed molecular adsorbate attached to it each [Lan86, Lan86b].

Our approach of choice is density functional theory, combined with molecular dynamics, as explained below.

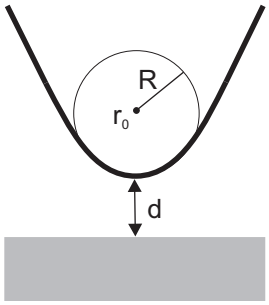

Figure 1.4: Schematic of the tunneling geometry by Tersoff and Hamann [Ter83]. The tip is assumed to be locally spherical at the position closest to the surface. The circle's center is labeled $\vec{r_0}$ and the radius of curvature R.

1.1.4 Density functional theory

Density functional theory (DFT) has become the primary tool for calculation of electronic structure in condensed matter, molecules, and other finite and heterogeneous systems [Hoh64, Koh99].

The fundamental principle of DFT is that any property of a system of many interacting particles can be viewed as a functional of the ground state density $n_0(\vec{r})$. In other words, one scalar function of position $n_0(\vec{r})$, determines all the information about the system, which is otherwise given by many-body wavefunctions of the system.

In order to understand advantages given by DFT for studying real systems, one would start from describing the basic Hamiltonian for the system of electrons and nuclei,

$$H = -\frac{\hbar^2}{2m_\mathrm{e}}\sum_i \nabla_i^2 + \sum_{i,I}\frac{Z_I\, e^2}{\left|\vec{r_i}-\vec{R_I}\right|} + \frac{1}{2}\sum_{i\neq j}\frac{e^2}{|\vec{r_i}-\vec{r_j}|} - \sum_I \frac{\hbar^2}{2M_I}\nabla_I^2 + \frac{1}{2}\sum_{I\neq J}\frac{Z_I\, Z_J\, e^2}{\left|\vec{R_I}-\vec{R_J}\right|}, \tag{1.10}$$

where electrons are denoted by lower case subscripts and nuclei, with charge Z_I and mass M_I, denoted by upper case subscripts. In the time-independent case, the many-body wavefunction $\psi\left(\vec{r_1},\vec{r_2},\vec{r_3},...,\vec{r_N}\right)$ of the system satisfies the time-independent Schrödinger equation

$$H\left|\psi_m\right\rangle = E\left|\psi_m\right\rangle \tag{1.11}$$

The ground state wavefunction ψ_0 is the state with the lowest energy, which can be determined, in principle, by minimizing the total energy with respect to all parameters in $\psi\left(\vec{r_1},\vec{r_2},\vec{r_3},...,\vec{r_N}\right)$. The problem is, however, that the exact solution is not feasible for any system of practical interest. In order to overcome this difficulty, one has to invoke various approximations, which make solution of equation 1.11 possible, and maintain accurate description of the physical properties. Density functional theory has been proven to be the most successful approximation, culminating in the Nobel Prize given to Walter Kohn in 1998 "*for his development of the density functional theory*".

The approach of density functional theory is to replace the difficult interacting many-body system obeying the Hamiltonian of equation 1.10 with a different *auxiliary* (Kohn-Sham) system that can be solved more easily [Koh65]. Such a system

describes non-interacting particles, while physically important many-body effects are included into an *exchange-correlation functional of the density*. Accuracy of this approach is limited only by the approximations in the exchange-correlation functional, and it was demonstrated that reasonable approximations can be made, like the local density approximation (LDA) or various gradient approximations (GGA), which describe accurately many condensed matter and molecular systems.

The solution of the ground state of a system is obtained by solving a system of Kohn-Sham Schrödinger-like equations:

$$(H^{\sigma}_{KS} - \epsilon^{\sigma}_{i})\ \psi^{\sigma}_{i}(\vec{r}) = 0 \tag{1.12}$$

where the ϵ^{σ}_{i} are the eigenvalues for spin σ, and H^{σ}_{KS} is the effective Hamiltonian (in Hartree atomic units)

$$H^{\sigma}_{KS}(\vec{r}) = -\frac{1}{2} \bigtriangledown^{2} + V^{\sigma}_{KS}(\vec{r}) \tag{1.13}$$

with

$$V^{\sigma}_{KS}(\vec{r}) = V_{ext}(\vec{r}) + V_{Hartree}(\vec{r}) + V^{\sigma}_{xc}(\vec{r}) \tag{1.14}$$

where $V_{ext}(\vec{r})$ is the external potential due to the nuclei and any other external field, $V_{Hartree}(\vec{r})$ is the classical Coulomb interaction of the electron density $n(\vec{r})$ with itself, and $V^{\sigma}_{xc}(\vec{r})$ is the exchange-correlation potential, which includes many-body effects by approximating them using local or semi-local functionals of the density.

One of the most efficient ways for solving the system of Kohn-Sham equations is to use pseudopotentials and plane-waves basis sets [Pay92]. Once the system of Kohn-Sham equations is solved and the ground state electron density $n_0(\vec{r})$ is obtained, many important physical properties can be obtained by calculating response of the ground state to various perturbations [Mar04]. One example of such properties is given by the "Hellmann-Feynman theorem", which allows direct evaluation of forces on all ions of the system from the ground state of the system

$$\vec{F}_{I} = -\frac{\partial E}{\partial \vec{R}_{I}} \tag{1.15}$$

Direct evaluation of forces within DFT allows to perform molecular dynamics simulations using the basic Newton's equations of motion. For a set of nuclei treated as classical masses with an interaction energy $E[\{\vec{R}_{I}\}]$ dependent upon the set of positions of the nuclei $\{\vec{R}_{I}\}$, the equations of motion are

$$M_{I}\ \ddot{\vec{R}}_{I} = -\frac{\partial E}{\partial \vec{R}_{I}} = \vec{F}_{I}[\{\vec{R}_{I}\}] \tag{1.16}$$

Whereas DFT is a *zero-Kelvin* theory, molecular dynamics allow *ab initio* quantummechanical simulations for systems at *nonzero* temperatures [Pay92].

1.2 Experimental details

1.2.1 The setup

The experiments were performed by means of a home-built scanning tunneling microscope, operated at liquid helium temperature in an ultra high vacuum environ-

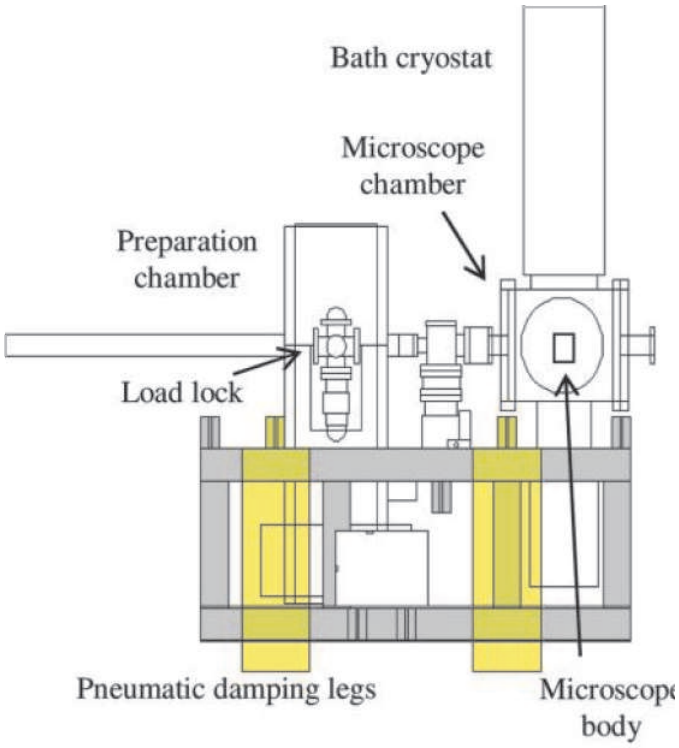

Figure 1.5: Schematic diagram of the STM system [Shi08].

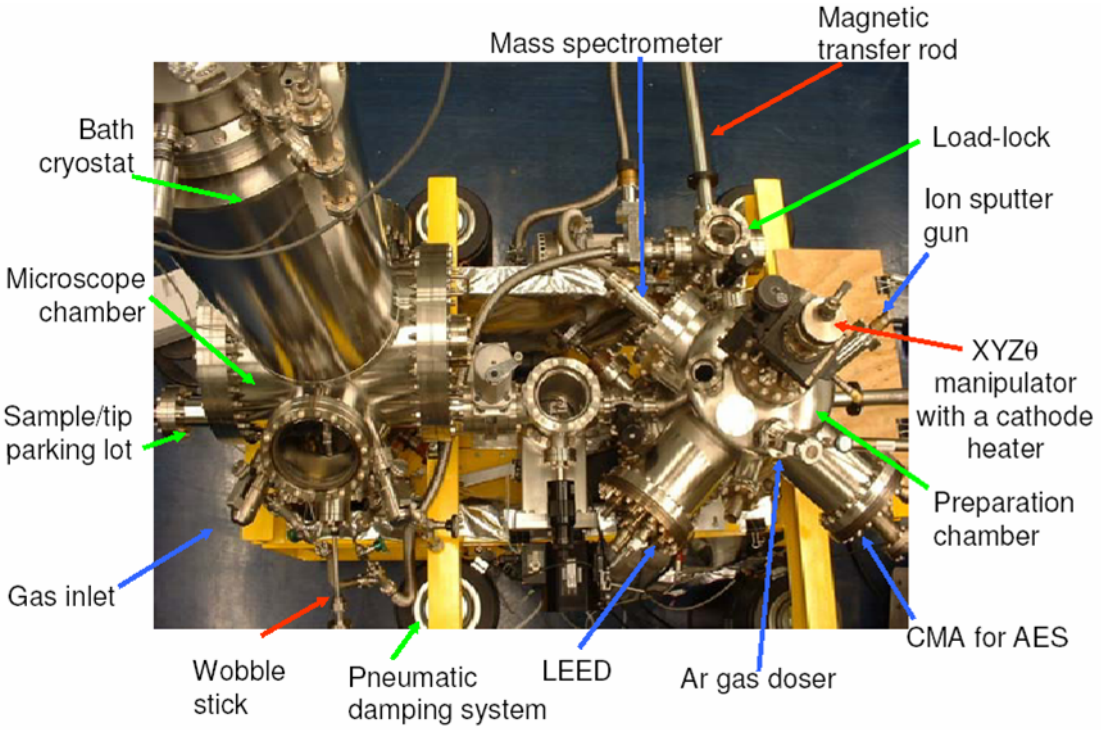

Figure 1.6: Picture of the instrument, with microscope (left) and preparation chamber (right).

ment ($p < 1 \cdot 10^{-10}$ torr) [Shi08], [Shi07]. The UHV system is divided into two main chambers, the microscope and the preparation chamber, the latter being equipped with standard surface science preparation and characterization techniques, see Fig. 1.5 and 1.6: There is an ion sputter gun that we used for sample preparation, a cathode heater for electron bombardment of sample and tip, and gases such as argon, oxygen, and ammonia. Low Electron Energy Diffraction (LEED), Cylindrical Mirror Analyzer (CMA) for Auger Electron Spectroscopy (AES), and quadrupole mass spectrometer as characterization tools are also situated in the preparation chamber. A bath cryostat is part of the microscope chamber, and its inner helium dewar has a volume of 8.5 L. The outer dewar holds 18 L of nitrogen. Gold-plated copper shields, that house the microscope scanner, are attached underneath, in thermal contact to the helium and the nitrogen dewar, respectively (custom-built by Cryo Vac). Both shields feature a shutter for sample and tip transfer into the scanner. Molecular deposition can be performed through an orifice of the shutter, while the shutter itself is closed. To avoid rest gas contamination and warming up of the scanner, the orifice has in turn a shutter.

The heart of the instrument is the scanner. It is located in a ceramic body out of macor and shows a modified Pan design [Wit97], [Pan99], see Fig. 1.7 (a). The sample is mounted on top of a tube piezo that sits on a sapphire prism, see Fig. 1.7 (b) and (c). Coarse approach works by six shear-piezo stacks that walk the prism up or down due to slip-stick motion, with the third pair of piezo stacks pressed against a Molybdenum spring plate on the front side, see Fig. 1.7 (d-f). Note that the tip position is stationary, whereas the sample is moved up or down. For scanning, the tube piezo is used. On top of the tube piezo (i.e., underneath the sample), there are also a silicon diode for measuring the temperature and a resistive heater with a range from LHe to room temperature. If the macor body is clamped to the Helium shield, tip and sample reach LHe temperature. Otherwise, the microscope hangs on three suspension springs, for vibrational isolation while being operated, and the temperature rises to ~ 6 K.

The sample holder is machined out of tantalum, which is the same material as the wires that are used to fix the sample onto the holder, see Fig. 1.8 (a). This prevents gradients in thermal expansion coefficients that would occur due to the large temperature range that the sample holder is exposed to (from 1800 K during annealing to 6 K in the microscope) and would lead to the sample getting loose. Either spot welding of the Ta wires to the sample holder or twining around screws was applied.

The tip holder is made out of stainless steel and has a tube that holds the Pt-Rh tip (30% Rh), see Fig. 1.8 (b). After etching the Pt-Rh wire by molten $NaNO_3$ (sodium nitrate) and NaCl salts, it was annealed by electron bombardment. Final preparation was performed by gentle tip-surface contacts and voltage pulses ≤ 10 V in situ.

Tip and sample transfer from atmospheric conditions into UHV happens via a loadlock that is attached to the preparation chamber. Transfers are performed by magnetic rods, a manipulator that also keeps the cathode heater, as well as a wobble stick (for transfer into the microscope).

On the microscope chamber, there is also a "parking lot" for storing up to six samples/tips, and there are mini cylinders for molecule deposition (water, ammonia etc.) that are connected to the vacuum by a leak valve.

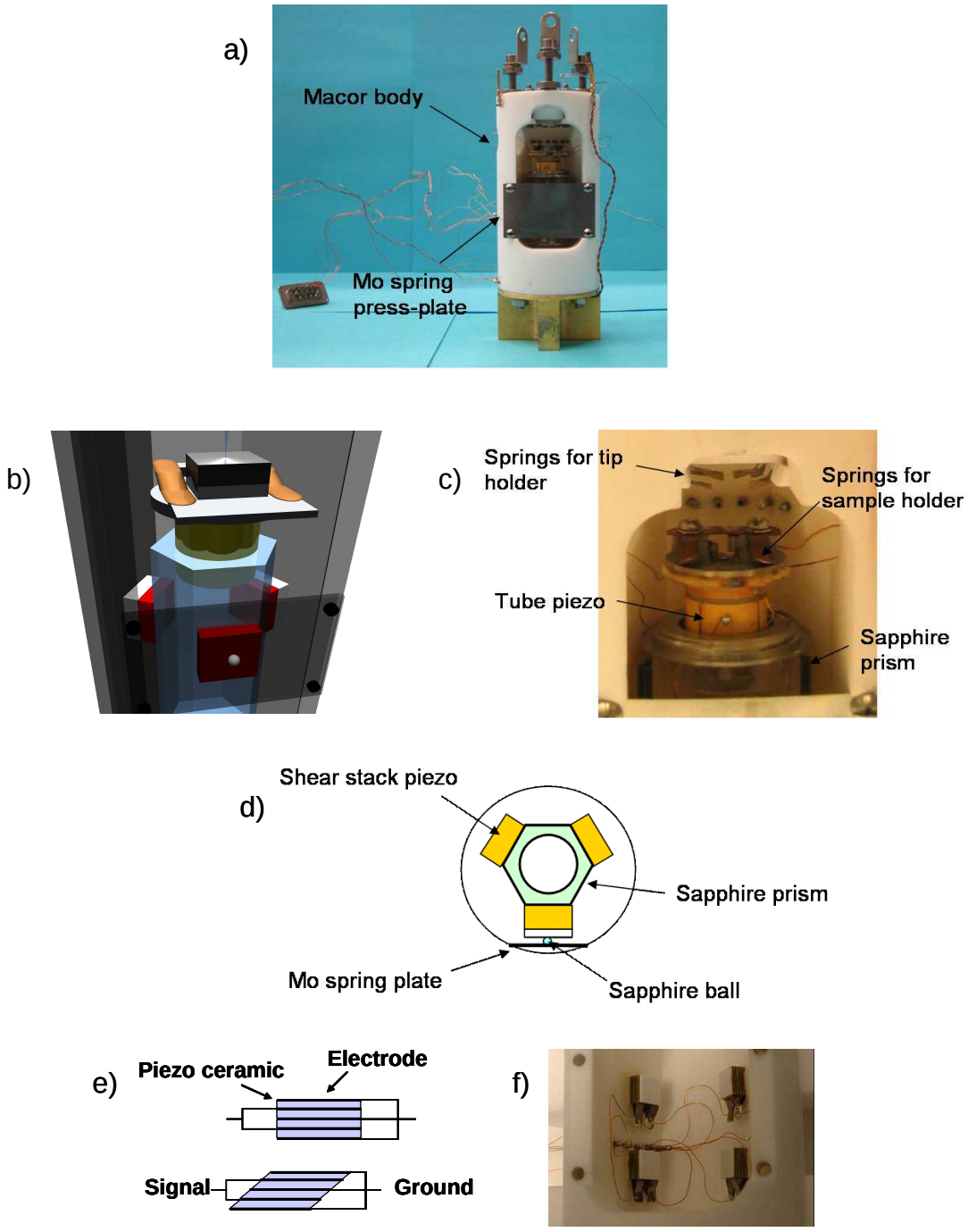

Figure 1.7: (a) The microscope scanner is located inside a macor ceramic body. (b) Schematic drawing of the scanner. The scanner is the moving part of the microscope. Up and down motion is performed by means of the sapphire prism that is walked by an inertia motor. Scanning is achieved by the tube piezo, with the sample on top, while the tip is stationary. (c) Picture of the scanner (no sample and tip mounted). (d) Cross-section view on shear-piezo stacks and sapphire prism used for coarse approach. (e) Working principle of a shear-piezo stack. By applying voltages to every other electrode, separated by piezo ceramic material, the stack shears. (f) Shear-piezo stacks realize the coarse approach by slip-stick motion of the sample towards the tip.

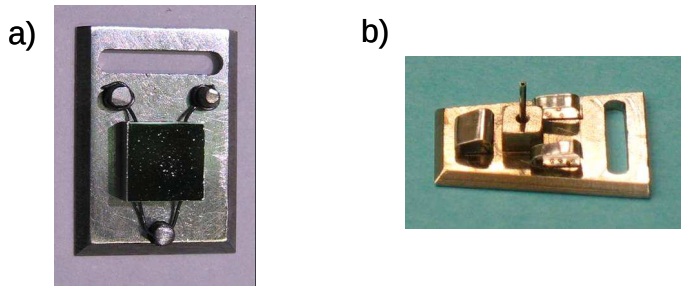

Figure 1.8: (a) Sample holder with ruthenium crystal. One way of mounting the crystal is fixing it by Ta wires that are twined around screws. (b) Tip holder out of stainless steel (no tip mounted in tip tube on the picture).

To maintain the ultra high vacuum, two ion getter pumps along with titanium sublimation pumps (in both chambers) and a turbomolecular pump (between the two chambers and separable by gate valves) are in use. Additionally, the shields of the cryostat serve as cryo pumps.

Commercial controller electronics (RHK 100), together with its standard tunneling current preamplifyers (gain 10^8 or 10^9) that were occasionally replaced by an external preamp ("Femto", gain 10^7, 10^8 or 10^9), was used.

For optimum performance, the microscope must not be perturbed by any kind of vibrations (from the building or the instrument itself), mechanical and electrical noise. To decouple the microscope body mechanically at the best, it is suspended by stainless steel springs. Three magnets, fixed at the cryostat shield, eddy-current damp the body. Also, the inner cryostat is hung like a pendulum relative to the outer cryostat. And pneumatic damping legs isolate the entire UHV system against low-frequency floor and building vibrations, see Fig. 1.6.

Right after tip-sample approach into tunneling regime, the images are distorted by piezo creep and thermal drift, which stabilizes after 1-2 hours. Images at a tunneling current setpoint of $\sim$ 1-2 pA could be reached.

1.2.2 Properties of the investigated systems

In the following section, basic properties of the Ru(0001) surface are presented, along with the sample preparation techniques that we used to achieve an atomically clean surface.

Further, the molecules ammonia and water are introduced, and the way how we adsorbed them onto the surface, is described. Also, the preparation of precovered Ru surfaces, i.e., O(2x1) as well as graphene on Ru(0001) is specified.

The Ru(0001) surface

Ruthenium (Ru) is a precious metal, and element N° 44 of the periodic table. It is part of the Platinum group, besides Rhodium, Palladium, Osmium, Iridium, and Platinum, as these metals have similar physical and chemical – in particular catalytic – properties (see Fig. 1.9). As a 4d transition metal with a ground state electron configuration of $[Kr]4d^7 5s^1$, the ruthenium single crystal is catalytically active.

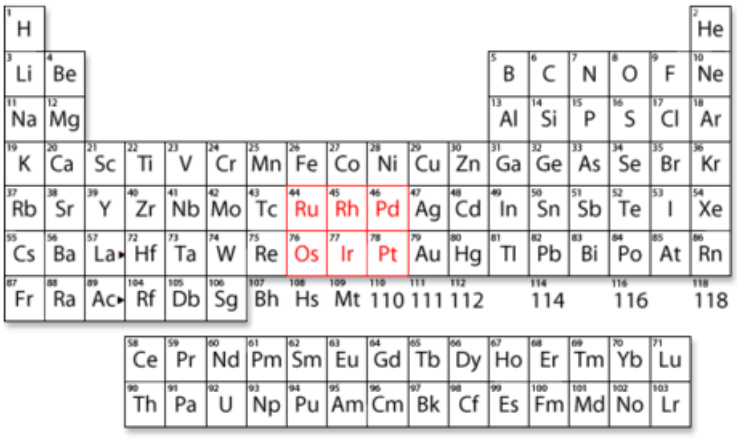

Figure 1.9: The Platinum group on the periodic table comprises Ru, Rh, Pd, Os, Ir, and Pt.

The crystal structure is hexagonally close-packed (hcp), that implies an ABAB... layer stacking, with a distance of $\frac{c}{2} = 2.14$ Å between the two layers A and B [Ash76], see Fig. 1.10 (a). For our experiments, we used the hcp Ru(0001) face, which is flat, see Fig. 1.10 (b). One can distinguish between the three-fold coordinated hcp and fcc hollow sites on the surface, the latter being the sites with no Ru atom in the underlying layer. The lattice constant a of this surface is 2.70 Å [Ash76], see Fig 1.10. Based on the comparatively low corrugation of this surface, atomic resolution by STM requires high tunneling current setpoints of >10 nA or a chemically modified tip, see Fig. 1.11 (a). Such images with atomic resolution reveal the orientation of the surface crystallographic directions.

After exposure to air, the ruthenium crystal was repeatedly sputtered by Argon ions at 1keV and a pressure of $3 \cdot 10^{-5}$ torr for 20-30 min, and subsequently annealed at 1600 K for three minutes. Further cleaning included several annealing and cooling cycles between 800 K and 1800 K in a partial oxygen atmosphere of $4 \cdot 10^{-8}$ torr, in order to deplete the first subsurface layers from carbon contamination, which is a common bulk impurity of ruthenium. The excess oxygen on the surface was removed by a short annealing period (20-30s) at 1700 K in ultra-high vacuum to desorb the remaining oxygen. After the annealing procedure, the sample was transferred to the cryostat and cooled down to 6 K. Since it is known that a small amount of preadsorbed molecules on the order of a few percent can have a drastic effect on the

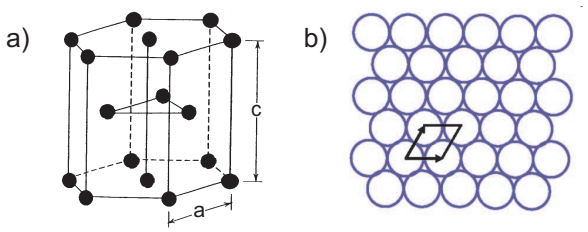

Figure 1.10: (a) The hexagonal close-packed (hcp) crystal structure. (b) The hexagonal Ru(0001) surface.

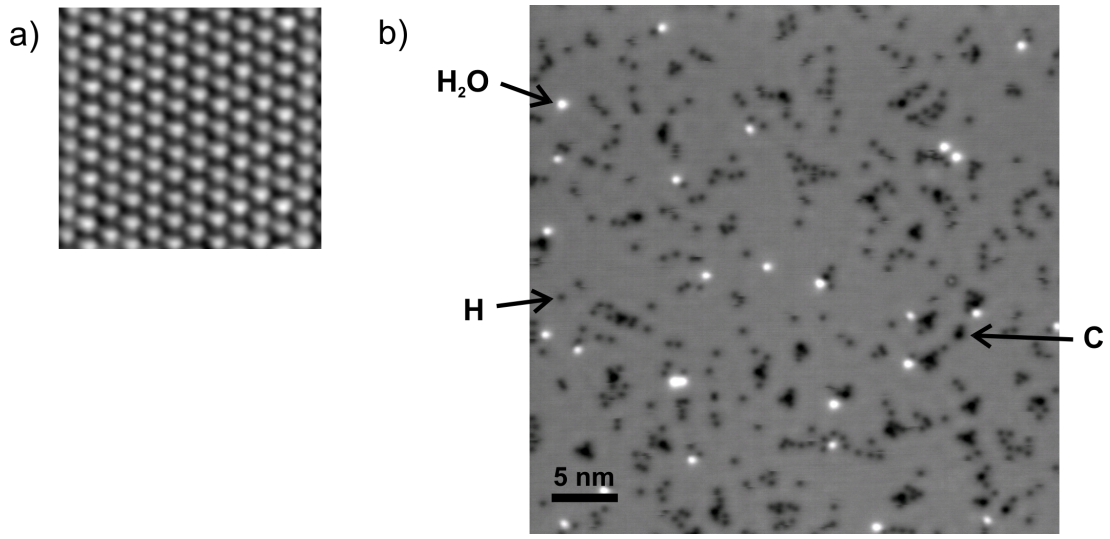

Figure 1.11: (a) Atomic resolution on Ru(0001) by STM, 3 nm x 3nm, 8 mV, 87 pA. (b) This STM image shows the "clean" Ru surface, with a few carbon atoms segregated from the bulk, and water and hydrogen contaminations that were adsorbed from the background. Scanning parameters 8 mV, 97 pA.

behavior of the adsorbed molecules, it is important to characterize the surface prior to their adsorption to determine its degree of cleanliness [Cla04, Hen02]. By STM, we observe extended terraces with a width on the order of tens up to hundreds of nanometers. Fig. 1.11 (b) shows a typical image acquired at 6K on a flat terrace. Some remaining impurities are present that appear as depressions (black spots), which we know from previous studies to be carbon (from segregation from the bulk during cleaning) and hydrogen (from background adsorption) [Shi08]. Water, also from background adsorption, appears as a protrusion (white spots). On ruthenium, hydrogen interacts strongly with the tip and diffuses easily when scanning at bias voltages above 80mV [Shi08, Shi08b]. The impurity coverage of our surfaces is typically below 1 % of a monolayer (carbon contamination below 0.2% of a monolayer and a hydrogen contamination below 1% on the surface).

The molecules

Ammonia is the NH_3 molecule, formed by a nitrogen atom and three hydrogen atoms that are arranged in a trigonal pyramidal geometry in the gas phase, having a bond angle of 107.8°, see Fig. 1.12. The position of the hydrogen atoms can be inverted relative to the nitrogen atom. While three of the five valence electrons of the nitrogen atom bind to the hydrogen atoms, the nitrogen lone pair remains unpaired which makes ammonia a proton acceptor. Ammonia is a polar molecule with a dipole moment of 1.42 D in the gas phase.

For our experiments, we used 99.99% anhydrous ammonia. Due to its toxicity, even at short exposures, measures for a safe handling of ammonia in the lab had to be taken, in order to prevent acute health effects like irritation of eyes, respiratory tract and skin. For dosing the sample in UHV, we mounted a mini cylinder (out of stainless steel and with a volume of 50 cm^3) onto the UHV chamber, that had to be

Figure 1.12: (a) The ammonia molecule NH_3 and (b) the water molecule H_2O.

filled with ammonia at $\sim$ 30 psi, see Fig. 1.14. The total release of this ammount of ammonia into the lab room would not result in any adverse health effect. Filling the mini cylinder, is the crucial step. Once filled, the ammonia remains in the mini cylinder for about a year, because just small amounts of ammonia are being consumed for each dosage. To ensure a high gas purity, the ammonia should not be contaminated by rest gases, while passing through the cross-shaped flange and valves, see Fig. 1.14. First, we baked and pumped mini cylinder, cross and valves to obtain high vacuum, and therefore clean stainless steel walls. Afterwards, we ran several "flush and pump" cycles, i.e., flushing ammonia from a lecture bottle (170g liquefied ammonia with vapor pressure of 8.75 atm at 21°C) into cross flange and mini cylinder to gradually substitute rest gas molecules (that are adsorbed on the stainless steel walls) by ammonia molecules. After a final flush, i.e., the actual filling of the mini cylinder, the cross flange and the connecting stainless steel tube between lecture bottle and cross were pumped, and the lecture bottle removed.

The deposition of the ammonia molecules onto the sample under UHV conditions, was performed by passing the ammonia through nozzles that pointed towards the sample (inside the UHV chamber), and by controlling a leak valve. This procedure was either realized in the preparation chamber at RT, or in the microscope chamber in situ, i.e., while the sample was kept at 6K inside the scanner. In the latter case, the door of the microscope was closed, and only the shutter for the dosing hole was open. Dosing time and pressure were calibrated by STM imaging.

Water is a planar molecule that has the chemical formula H_2O, see Fig. 1.12. It shows a bond angle of 104.45° between the two covalent O-H bonds, and it exhibits two electron lone pairs. A water molecule can accept two and donate two hydrogen atoms, when bonding to other water molecules. Its dipole moment results in 1.85 D.

Both, liquid water and ice form hydrogen bonds between adjacent oxygen and hydrogen atoms. Even though hydrogen bonding is a weak interaction, it is yet powerful by means of crystal formation. At ambient conditions water shows an anomaly when freezing: ice is approximately 10 % less dense than liquid water, i.e., it is expanding when freezing. At 4°C liquid water reaches its greatest density and by decreasing the temperature towards the freezing point it becomes less dense as the water molecules begin to form the hexagonal crystals of ice that are less compact.

Ice is known for plenty of different phases, depending on pressure and temperature. In Fig. 1.13, a scheme of hexagonal crystalline ice I_h, the predominant phase on Earth, is illustrated. Ice I_h shows characteristic bilayer stacking. The atomic arrangement minimizes electron-electron repulsion in a tetrahedrally bonded, hexagonal-close-packed "wurtzite" structure. Thanks to tetrahedral bonding, the crystal forms a stack of bilayers. Each oxygen atom in a bilayer forms hydrogen bonds with three nearest neighbors in a plane 0.92 Å below it, and a fourth with

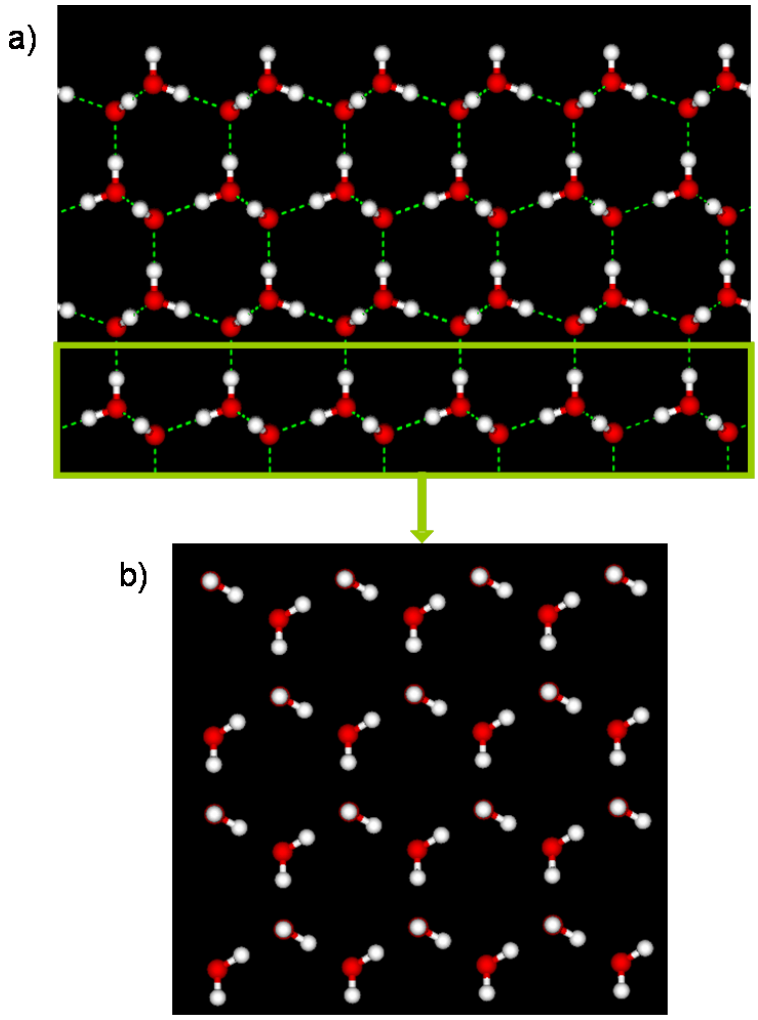

Figure 1.13: Naturally occurring ice I_h crystallizes in a tetrahedrally bonded, hexagonal-close-packed "wurtzite" structure by forming a stack of bilayers. (a) side view (hydrogen up), (b) top view on one bilayer.

an equidistant O atom 2.76 Å above in the neighboring bilayer, i.e., establishing a two acceptor - two donor configuration. Fig. 1.13 (a) shows the side view of the bilayered crystal and (b) the top view on one bilayer. The lattice constant of ice I_h is of 4.5 Å, close to $\sqrt{3}$ times the interatomic spacing of group VIII metals (4.69 Å for Ru and 4.76 Å for Pd) [Fei10]. Apart from ordered, crystalline forms of ice, amorphous states of water (amorphous solid water) exist as well.

For our setup we purified liquid water (deuterium depleted 99.99995 atom %H), contained in a glass tube, by repeated cycles of freezing, pumping, and thawing prior to introduction into the microscope chamber through a leak valve with an attached nozzle pointing towards the sample. While dosing, the sample was kept either at 50 or 100K, followed by annealing to temperatures between 110K and 145K at a rate of 10-20 K/min.

Precovered Ru surfaces

O(2x1) on Ru(0001) is a surface reconstruction, where 50% of the surface is covered by oxygen atoms. Their adsorption sites are hcp hollow sites, and the oxygen

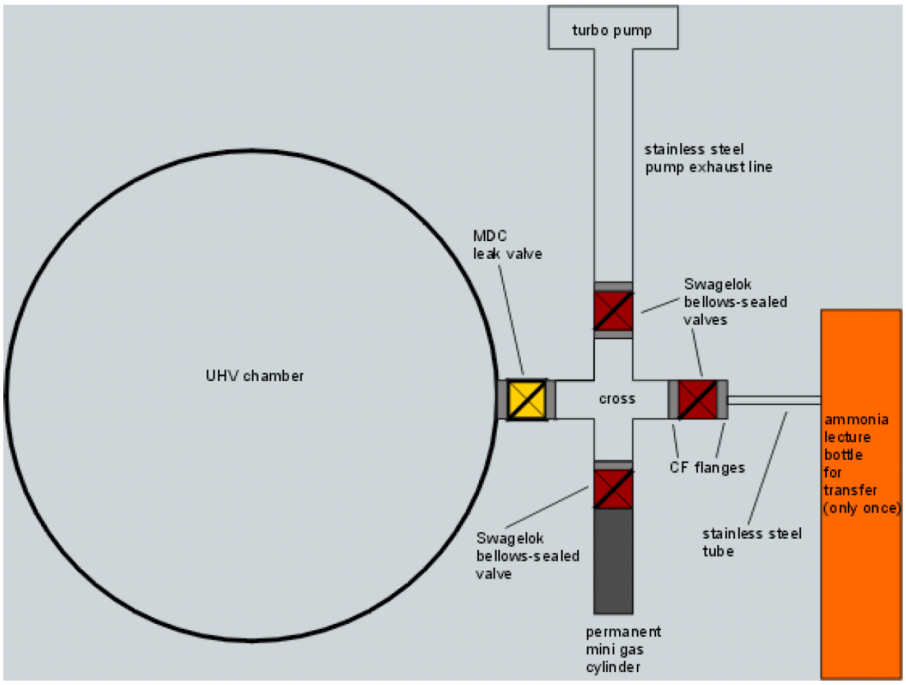

Figure 1.14: Experimental setup used for ammonia preparation on the UHV chamber.

atoms form rows along one lattice direction of the surface, every other row being vacant (within a given domain).

Above room temperature, molecular oxygen dissociatively adsorbs onto Ru(0001). To achieve a highly ordered oxygen reconstructions with large 2x1 domain formation, heating of the surface is needed. The saturation coverage for O(2x1) is thus 0.5 ML [Mei97].

Exposing the clean Ru surface to 60 L (600s at $1{\cdot}10^{-7}$ torr) of oxygen at 820 K, followed by 10 min annealing at 930 K, leads to well ordered p(2x1) oxygen domains. After this preparation the sample was transferred to the STM for imaging and dosing water. Water was dosed in situ through a tubular doser at sample temperatures between 140 K and 200 K.

Graphene is a single layer of graphite. This means, it is a planar and strictly two-dimensional material that shows a honeycomb structure of sp^2 bonded carbon atoms, with a carbon-carbon bond length of 1.42 Å. Graphene is a basic building block for graphitic materials of all other dimensionalities, i.e., 0D buckyballs, 1D nanotubes and 3D graphite, see Fig. 1.15 [Gei07].

In contrast to free-standing graphene, on Ru(0001) graphene interacts with the underlying metal due to a strong electronic coupling between monolayer graphene and the adjacent metal[Sut09]. There are effects caused by the fact that graphene is adsorbed on a surface, e.g., buckling of the graphene [Win09], or the occurence of Moiré patterns in STM images [Mar07].

We grew graphene on Ru(0001) by segregation of carbon from the bulk, when annealing at 1800 K for 30 s. Under these conditions, graphene did not cover the entire surface but consisted of islands, separated by several micrometers.

Alternatively, graphene can be grown by dissociative adsorption of hydrocarbons,

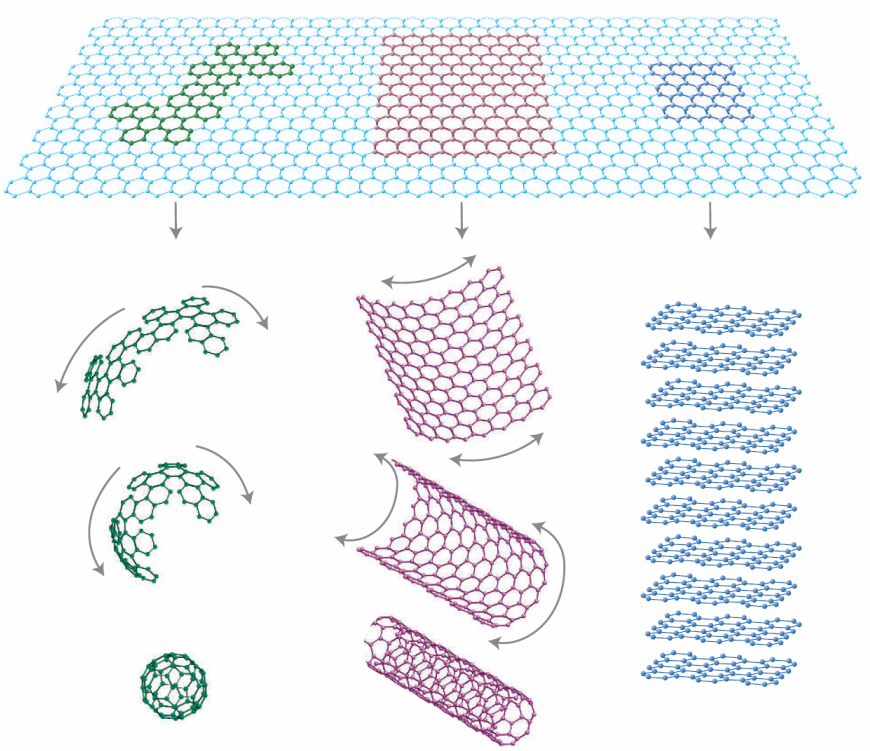

Figure 1.15: Graphene as a basic building block of all graphitic forms: 0D buckyballs, 1D nanotubes, 3D graphite [Gei07].

such as ethylene, upon the heated Ru surface (750-1000 K) [Log08, Log09b].

1.2.3 Electron and field-induced manipulation of adsorbed molecules using STM

High lateral resolution, combined with high energy resolution, allows using the STM for single-molecule chemistry experiments. For example, by applying a certain bias voltage to the atomically sharp tip, the STM can be used as a tool to manipulate the adsorbed molecule, e.g., to induce diffusion, desorption, change in configuration, to break or create chemical bonds of the adsorbate, or to change its charge state [Bar99, Cro93, Eig90, Rep04, Kim02, Pas03, Hla00, Str91, Qiu04].

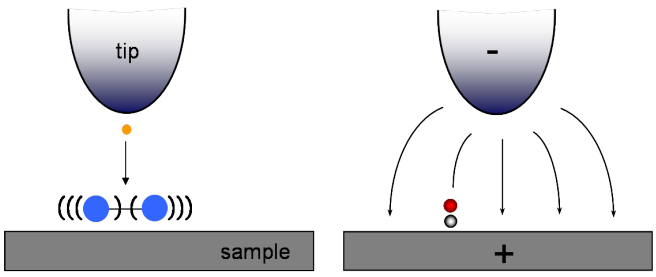

Figure 1.16: Electron tunneling (left) and field induced manipulation (right) within a tunneling junction composed of STM tip, adsorbate molecule and surface.

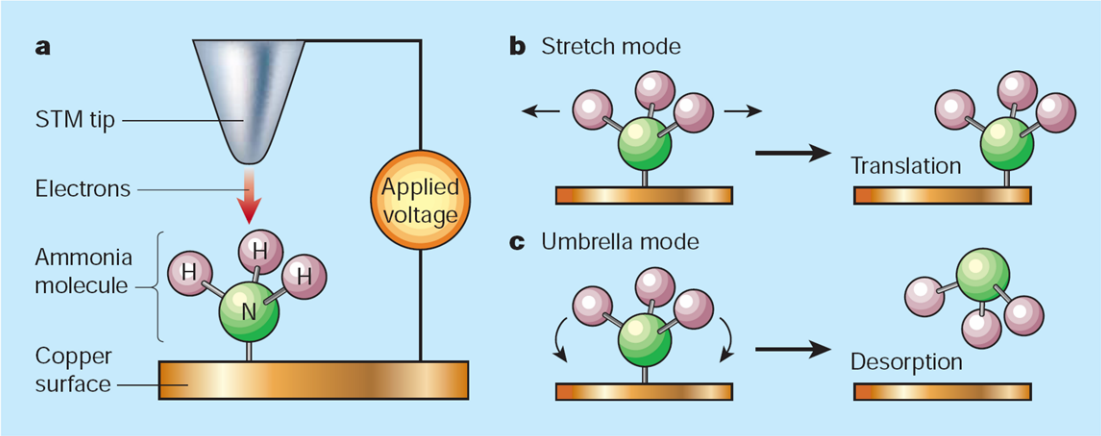

Figure 1.17: By tuning the energy of tunneling electrons emerging from an STM tip, one can selectively excite a vibrational mode within an ammonia molecule on a Cu surface. Excitation of the N-H stretch mode causes translation, whereas selecting the umbrella mode of the molecule leads to its desorption [Pas03].

In our case, diffusion, desorption and dissociation of single ammonia molecules were observed upon applying short voltage pulses between the tip and the molecule under study.

Tunneling electrons from an STM tip can be applied to induce diffusion and desorption reactions of an adsorbed molecule, as shown in Fig. 1.17: The N-H stretch or the umbrella (inversion) mode of an individual ammonia molecule on a Copper surface is selectively activated by adjusting electron tunneling current and energy to result in a translation or a desorption mechanism, respectively. On Ru(0001) the symmetric and antisymmetric N-H stretch modes were measured by high-resolution electron energy loss spectroscopy (HREELS) at ν_s= 407 meV and ν_a= 421 meV, the umbrella modes at δ_s= 133 to 143 meV and δ_a= 197 meV and the Ru-NH_3 stretch mode $\nu_\perp$ = 42 meV [Par88].

Exciting intramolecular vibrations via inelastic tunneling may also lead to dissociation of a molecule, as was shown for oxygen molecules on a Platinum surface [Sti97], see Fig. 1.16. Upon applying three different bias voltages a single excitation, a multiple-step excitation, or multiple excitations among the levels lead to dissociation, see Fig. 1.18 (a). In the case of inelastic tunneling, the minimum voltage for dissociation, i.e., the dissociation threshold, depends on the specific energy that is needed to excite a certain molecular vibration. It does *not* depend on the distance between tip and sample.

An electric field can also trigger a dissociation event (see Fig. 1.16), e.g., by inducing a dipole in the adsorbate or by reducing the potential barrier height which increases the probability for a reaction [May06]. Moreover, it was observed that electric fields, caused by an STM tip, can interact with a vibrational mode of a molecule that is adsorbed in the tunneling junction, changing the energy of the mode as a function of the applied electric field and modifying the binding characteristics of the molecule [Yan08]. It is important to keep in mind that the threshold voltage is proportional to the tip-sample distance for an electric field effect of a plate-capacitor geometry, see Fig. 1.18 (b).

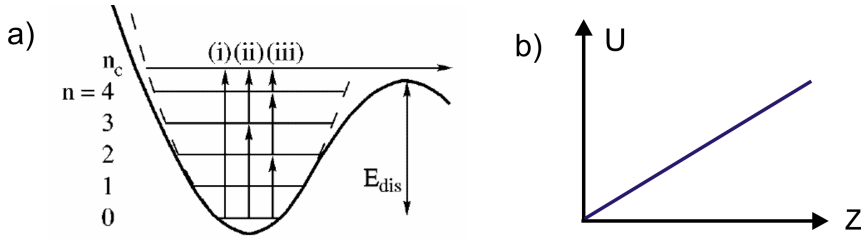

Figure 1.18: (a) Potential energy well for inelastic electron tunneling: three sets of excitations among the levels lead to dissociation for three different biases, either via a single multiple-step excitation (i) or via multiple excitations (ii) and (iii) [Sti97]. (b) For an electric field effect the threshold voltage U for a dissociation event is proportional to the tip-sample distance z, when assuming a plate-capacitor geometry for tip and sample.

We realized our setup for manipulation experiments by using the RHK controller with either the RHK tunneling current preamplifyer (gain 10^8 or 10^9, respectively) or an external preamp ("Femto", gain 10^7, 10^8 or 10^9). When studying dissociation induced by the STM tip, we proceeded as follows:

After taking an image, we placed the tip over a molecule with a specific height z_0, which may correspond to the chosen current setpoint of the previous image. Now, the feedback loop was opened and the tip retracted from its starting position by a distance Δz (on the order of nanometers), and a voltage pulse of a few milliseconds up to 1 min was applied between tip and sample above the molecule (see Fig. 1.19). Due to the open feedback loop Δz was kept constant during the pulse. What we were particularly interested in was to determine the threshold voltage required to dissociate a molecule at a given Δz. While applying the voltage pulse, we also recorded the current (over time) that was measured between tip and sample.

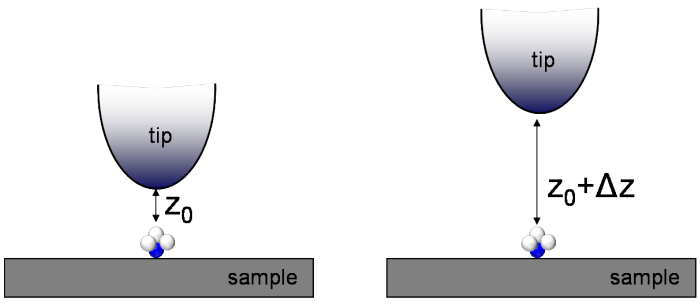

Figure 1.19: Schematic of the manipulation mechanism. From a starting height z_0 over an adsorbed ammonia molecule, the tip is retracted by a distance Δz, before a voltage pulse is applied.

2 Single-molecule ammonia chemistry on ruthenium

As a hydrogen carrier with high hydrogen storage capability, ammonia has the potential to carry energy for fuel cells [Tho06, Kle08, Cho01]. To extract the hydrogen, ammonia needs to be decomposed (or *dehydrogenated*). Decomposition has to happen in a controlled way with nitrogen as the only exhaust gas, while gaining three hydrogen atoms from every ammonia molecule. The ammonia decomposition reaction is endothermic, and is thus conventionally thermally activated over a catalyst surface. Commercially, Ni on alumina is the catalyst of choice for ammonia decomposition. However, promoted Ru is currently the best known catalyst for this reaction, with temperatures for sufficiently high conversion above 300°C. As the equilibrium conversion depends on the temperature and the reaction is endothermic, this leads to a rising ammonia equilibrium concentration with decreasing temperature, e.g., at 425°C and 1 bar, the ammonia conversion is 98-99 %. For low temperature fuel cells such as polymer electrolyte membrane (PEM) fuel cells, unconverted ammonia causes a problem because it reacts with the electrolyte, which thereby deactivates. To ensure continuous operation, the ammonia concentration must be reduced below 1 ppm.

Previous work on ammonia dehydrogenation, including on Ru surfaces, has been achieved by Gerhard Ertl, who was awarded the Nobel prize in Chemistry in 2007 *"for his studies of chemical processes on solid surfaces"*. He applied thermal desorption spectroscopy (TDS), low-energy electron diffraction (LEED) and high resolution electron energy loss spectroscopy (HREELS) among other techniques to study the thermal decomposition of ammonia and the vibrational modes of its constituents [Jac00], [Die96], see also chapter 1.2.3. Note that these studies did not aim at the single-molecule scale.

On the other hand selective dehydrogenation of single molecules, such as phthalocyanine and methylaminocarbyne, was conducted by STM, by applying voltage pulses [Zha05, Kat07]. There, the goal was to tailor a specific product rather than investigating the effect that leads to dissociation.

Further the vibrational properties within an adlayer of ammonia on Ru(0001) were investigated and a drastic red shift of its umbrella mode was measured with increasing coverage and interpreted as a Stark shift due the electric fields produced by the static NH_3 dipoles within the adlayer. As a consequence of the electric field the ammonia molecule opens its H-N-H angle and a softening of the umbrella mode occurs [Wid99].

Theory-wise, a huge contribution in the context of ammonia synthesis reactions was made by Jens Nørskov's group [Hon05]. Especially relevant to this thesis is their assignment of the adsorption sites to the different NH_x species on Ru(0001), see Tab. 2.1 [Log03].

In this chapter we study in detail and at the single-molecule scale, the reaction

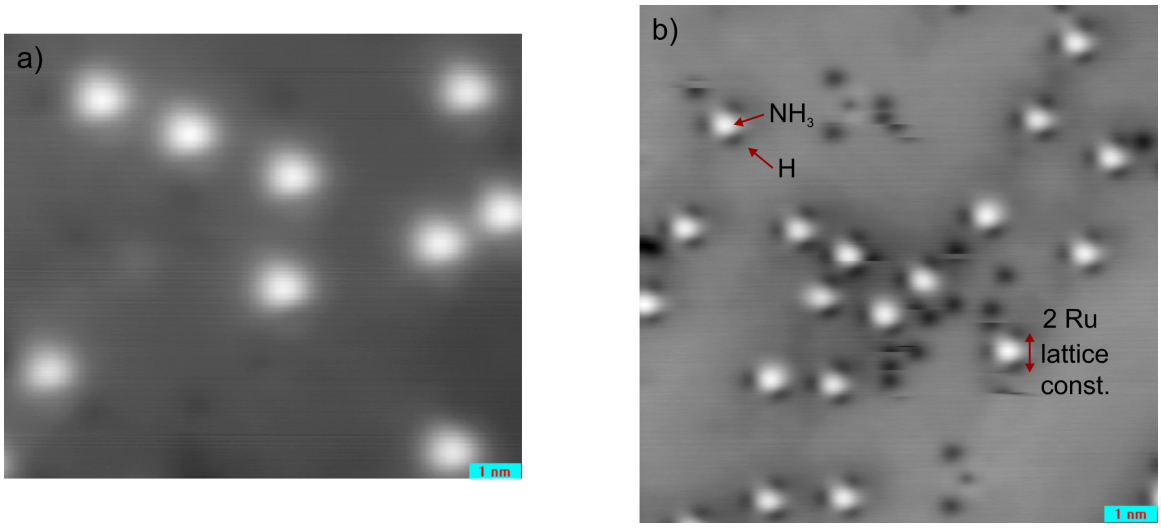

Figure 2.1: (a) STM image of individual ammonia molecules on Ru(0001), 63 mV, 15 pA. (b) Ammonia (bright spots) surrounded by hydrogen atoms (depressions). Each two hydrogen atoms align along a surface direction, separated by two Ru lattice constants, 75 mV, 17 pA.

mechanism for ammonia decomposition over a Ru catalyst surface. Our goal is the controlled and successive dehydrogenation of a single ammonia molecule, and the understanding of the dissociation process step-by-step.

2.1 Adsorption and identification of NH_x species

Ammonia on Ru(0001) was deposited either in-situ at low temperature while the sample was residing in the STM, or at room temperature in the preparation chamber. Both temperature regimes are below the dissociation temperature of ammonia on ruthenium, and thus we did not observe any differences. Ammonia molecules on Ru have never been imaged by STM before, see Fig. 2.1 (a). A single ammonia molecule appears as a bright protrusion, with an apparent height of +48 to +58 pm.

Ab-initio calculations and STM simulations of ammonia and other species on Ru(0001), that are going to be presented throughout this chapter, were performed by J. Cerdá (Instituto de Ciencia de Materiales de Madrid (Spain)). The method used for calculations and simulations is attached at the end of this chapter. Assuming

Table 2.1: Experimental and theoretical adsorption sites for H and NH_x on Ru(0001) from the literature, i.e., prior to this study.

Species	Adsorption Site Theory		Adsorption Site Experiment	
H	fcc	[Log03, Son07]	fcc	[Shi08, Kos04]
N	hcp	[Log03, Son07]	hcp	[Tro96, Sch97]
NH	hcp	[Log03, Son07]	?	
NH_2	bridge/fcc	[Log03]/[Son07]	?	
NH_3	on-top	[Log03]	?	

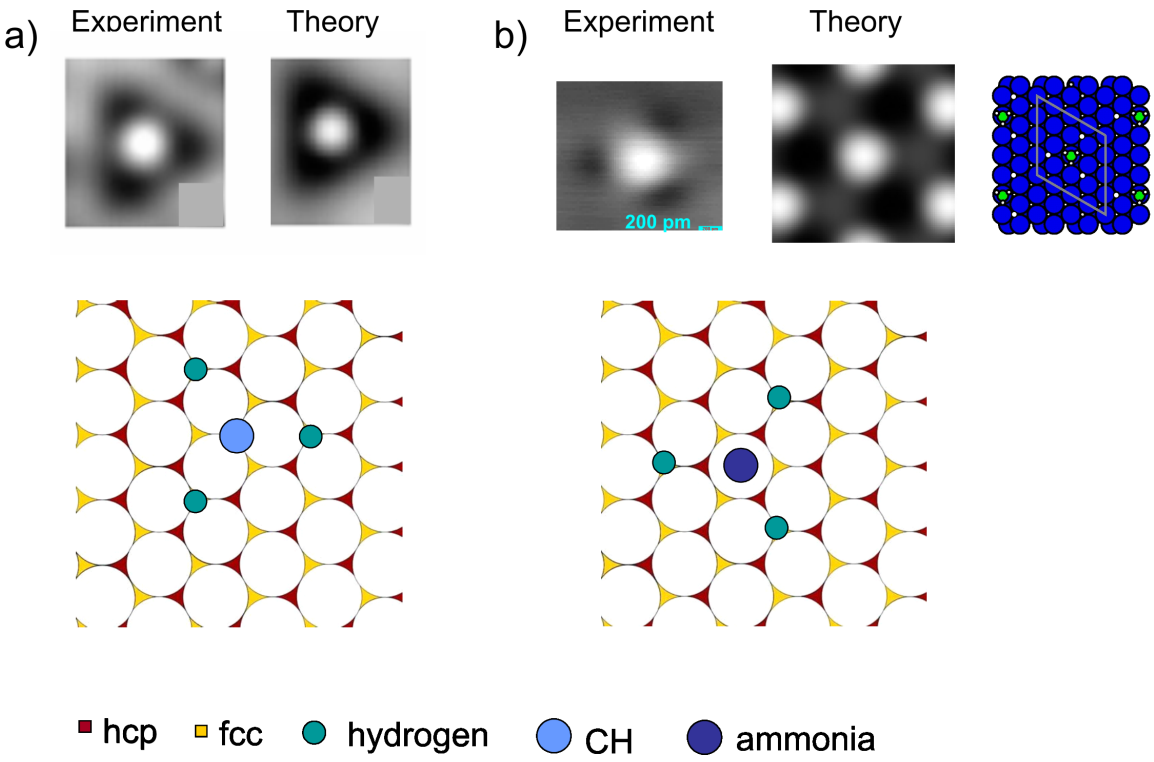

Figure 2.2: Experimental and simulated STM images of CH and ammonia surrounded by 3H on Ru(0001). (a) Complex of CH+3H [Shi08b], (b) NH_3+3H (the experimental image is a detail of Fig. 2.1 (b)). While CH adsorbs at an hcp hollow site, ammonia sits on-top. The 3H adsorb at fcc sites in both geometries.

the ammonia molecule adsorbed on-top with its hydrogen pointing first layer Ru atoms, the simulated image resembles nicely the experimental data, and with 50 pm in height also features the same apparent height as the experimental image, see Fig. 2.6 (a). Note that the DFT energies for the orientation of the NH_3 molecule relative to the substrate are close, i.e., the energy difference between the orientation mentioned above and a configuration with the hydrogen pointing towards fcc/hcp sites is small.

Depending on the hydrogen concentration that is present in the background pressure of the UHV chamber, and due to the fact that ruthenium is a reactive surface on which hydrogen dissociatively adsorbs, we observe zero to three hydrogen atoms that surround an ammonia molecule, see Fig. 2.1 (b). In combination with atomic-resolution images of the Ru surface (see Fig. 1.11 (a)), we know that each two hydrogen atoms align along a surface direction, and adsorb at fcc sites, two lattice spacings apart. A similar geometrical configuration was observed for CH+3H, see Fig. 2.2 (a) [Shi08b]. In the case of ammonia, the surrounding hydrogen atoms diffused when scanning with voltages above the excitation threshold of the H-Ru streching mode, i.e., 85 meV [Kos04], whereas ammonia was stable at typical scanning conditions. Fig. 2.2 (b) shows a zoomed image into one of the experimentally observed NH_3+ 3H complexes. The simulated image next to it in Fig. 2.2 (b) qualitatively matches the measured one, although the three hydrogens at nearest neighbor fcc sites are not resolved individually but appear as a rather large hole.

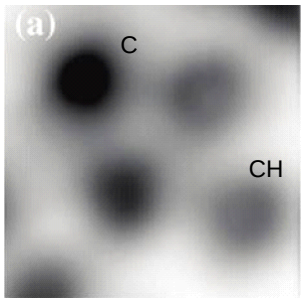

Figure 2.3: CH, the hydrogenated species, shows a weaker corrugation than the carbon atom [Shi08].

Overall, the (4x4) unit cell does not seem large enough to obtain a "perfect" agreement with the experimental data. However, simulations for a (6x6) supercell would be very time-consuming.

In Fig. 2.3 we see the different imaging contrast that CH and C exhibit. It can be clearly seen that C appears much darker than the hydrogenated species. Further, it is known that both species, C and CH, adsorb at an hcp site [Shi08]. We shall find an analogy to these observations when studying N and NH.

As our goal was to dehydrogenate a single ammonia molecule step-by-step, we started by taking an image, and chose an intact ammonia molecule. For the series in Fig. 2.5 we then placed the tip over this particular molecule and applied a voltage of 3 V for 1 ms. In the subsequent image, we identified a different species with a weaker imaging contrast, i.e., +6 to +12 pm, which we will later assign NH_2. Another 3 V pulse of 1 ms duration leads to a third species, i.e., NH. This time, the contrast is a depression of -7 to -13 pm. Yet another such pulse gives rise to a fourth species of -27 to -31 pm that we will identify with N. Additional voltage pulses were applied to the fourth species, and no further change of its shape was observed. This indicates that each pulse leads to the dissociation of one hydrogen atom until, after three pulses, NH_3 is completely dehydrogenated, leaving behind a N atom on the Ru surface. The step-by-step dehydrogenation of ammonia was highly reproducible.

We thus observe a decreasing corrugation, starting with NH_3 and ending with N, see Tab. 2.2. Only in the case of atomic nitrogen there is STM data available from the literature that we can compare our measured height of N/Ru(0001) with: in Fig. 2.4, the corresponding STM image is shown, recorded at room temperature. The nitrogen atoms appear as depressions of -30 to -40 pm, in agreement with our value of -27 to -31 pm. The adsorption site is a hcp hollow site [Tro96]. For the NH_2 site there has been no experimental evidence so far, mainly because it is not stable at room temperature [Log03]. The adsorption site for NH and NH_3 on Ru(0001) have not been determined by experiments either.

Table 2.2: Apparent heights of NH_x species. Heights do not depend on bias polarity for experimental scan parameters of typically ± 36mV, 12pA. The theoretical parameters are +50 mV, 100 pA.

Species	**NH_3**	**NH_2**	**NH**	**N**
Height Exp	+48 to +58 pm	+6 to +12 pm	-7 to -13 pm	-27 to -31 pm
Height Theo	+50 pm	+22 pm	-15 pm	-35 pm

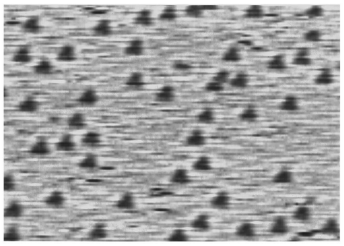

Figure 2.4: The height profile of N atoms is -30 to -40 pm, and their adsorption site is an hcp-hollow site. Image parameters: 86Å x 54Å, -0.6V, 30nA [Tro96].

In the following we present STM image simulations of all NH_x species. The most stable adsorption sites of each species were theoretically obtained in agreement with Nørskov's group [Log03]: N and NH at an hcp site, NH_2 at a bridge and NH_3 at an atop site. Fig. 2.6 shows images for all NH_x, simulated at V = +50 mV and I = 100 pA by using clean Pt(100) tips. The apparent heights of the species increase with rising x (x = 0 - 3), ranging from -35 pm for N, over -15 pm for NH, +22 pm for NH_2 to +50 pm for NH_3.

This matches our experimental results pretty well (see also Tab. 2.2), as the calculated apparent height for NH_3 is within the measured range, and the ones for NH and N are very close. The only exception is NH_2, with its theoretical height being larger by a factor of 2-3. Thus, the good agreement between calculations and experiments are strong evidence that indeed successive dehydrogenation of ammonia was achieved.

When taking a look at the full width at half maximum (FWHM) of the cross sections, we see that the experimental sections are larger by a factor of ~ 2, compared to the calculated plots (an exception is NH where both cross sections agree). This can be explained by considering that the experimental image reflects the convolution with a tip that probably is not highly symmetric, whereas for the simulations a perfect Pt(100) tip was assumed.

Note that there also occurs diffusion and desorption, while applying these voltage pulses. An example for dissociation combined with diffusion is given in Fig. 2.5 when NH_2 was generated: The position of NH_2 had changed with respect to the one of the previously intact ammonia molecule.

A good way to confirm the assignment of the different NH_x species that we made experimentally, is to determine their adsorption sites. Of particular relevance is the knowledge of initial and final configuration for the dehydrogenation reaction, as these states are of crucial importance for the theoretical description of the dehydrogenation process (see chapter 2.2). In Fig. 2.7, the same scan frame is shown three times: the left image (a) was taken without atomic resolution of the Ru lattice, whereas the center one (b) is atomically resolved. In order to achieve atomic resolution, the tunneling current setpoint had to be changed drastically. Starting at a bias of 8 mV and a tunneling current of 237 pA (Fig. 2.7 (a)), we increased the current until obtaining clear resolution of the Ru lattice, namely at 13 nA. However, at such high currents, the ammonia molecules diffuse while scanning, and we cannot determine their adsorption site directly. On the contrary, the nitrogen does not diffuse at 13 nA. Besides, there is an unknown contaminant on the surface (tiny gray spots on the two images in (a) and (b)) that also remain immobile. In Fig. 2.7 (b) we see

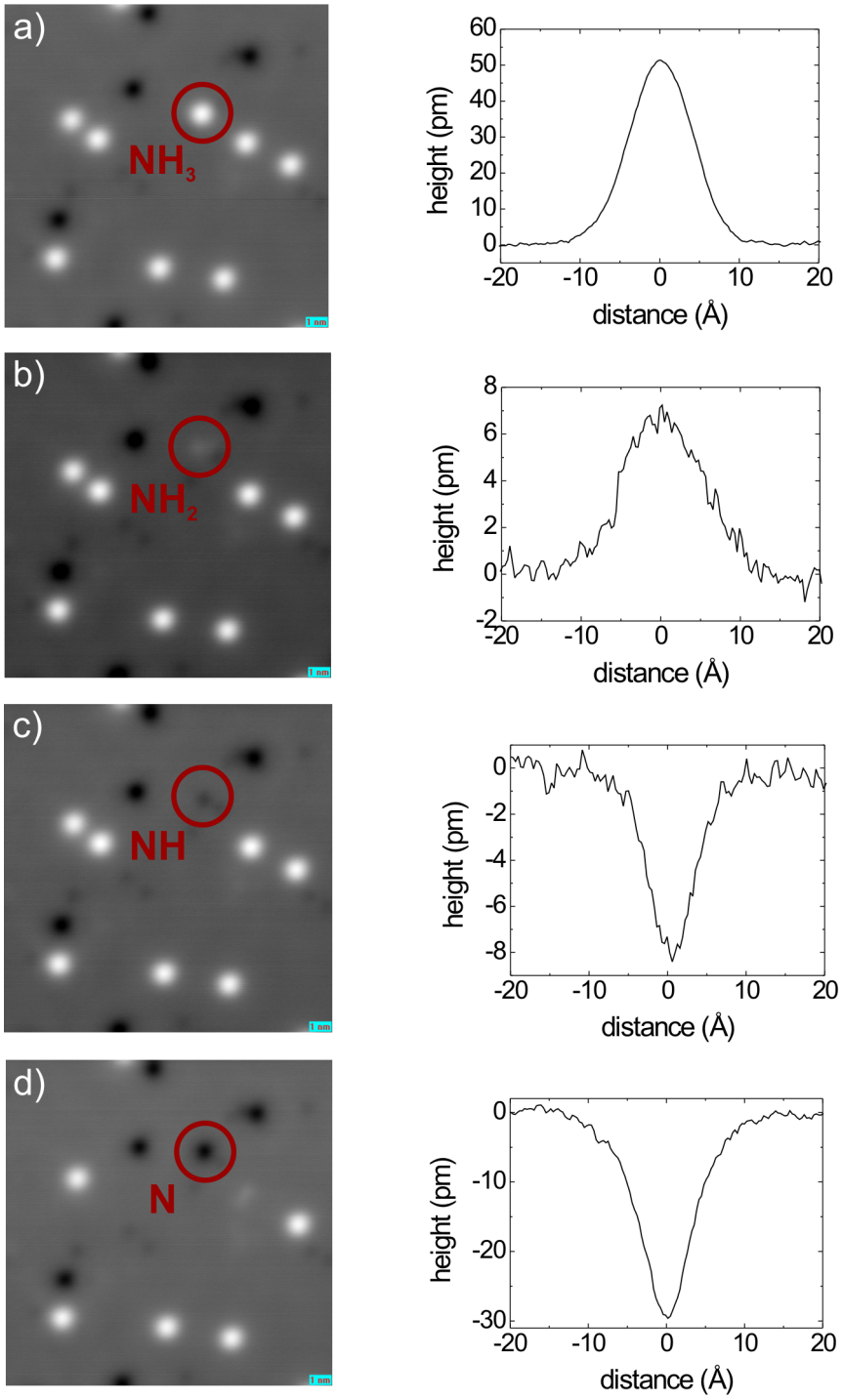

Figure 2.5: Successive dehydrogenation of a single ammonia molecule on Ru(0001) by applying voltage pulses of 3 V for a duration of 1 ms (left column). The right column displays height profiles (cross sections), taken of the encircled NH_x species. Starting with an intact ammonia molecule, the voltage pulse leads to NH_2 with a decreased apparent height. Further pulses produce NH and N, respectively, which show depressions in contrast, with N being the deepest. The scanning parameters are 30 mV, 252 pA, 15 nm x 15 nm.

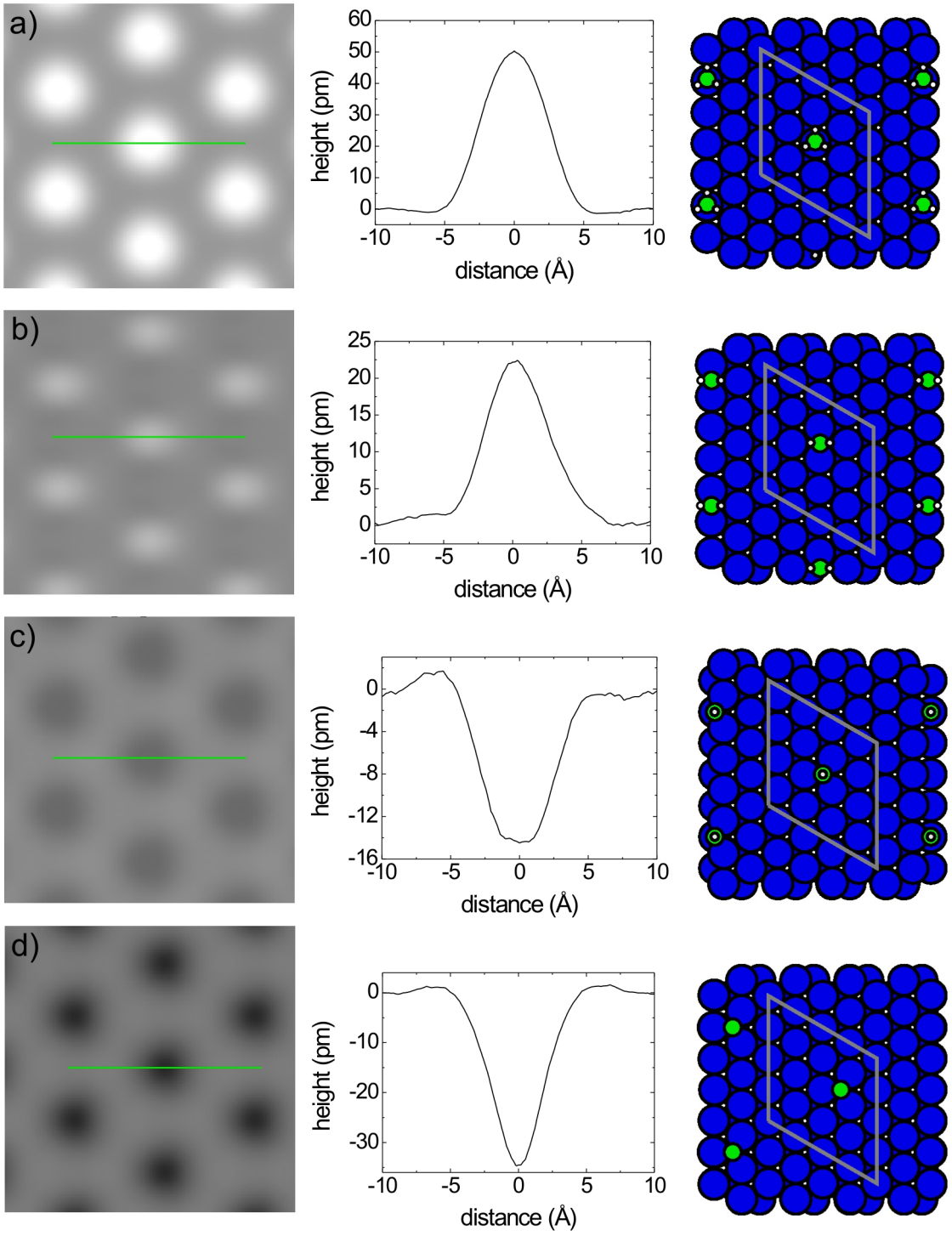

Figure 2.6: Simulated STM images of all NH_x species (left column), along with their height profiles (center column) and adsorption geometries (right column). The most stable adsorption sites obtained for each species are in agreement with Nørskov's group [Log03]: NH_3 at an on-top site, NH_2 at bridge, and N and NH at hcp sites. The apparent heights of the NH_x species increase with rising x (x = 0 - 3), ranging from -40 pm for N to +50 pm for NH_3. V = +50 mV, I = 100 pA , and use of a clean Pt(100) tip.

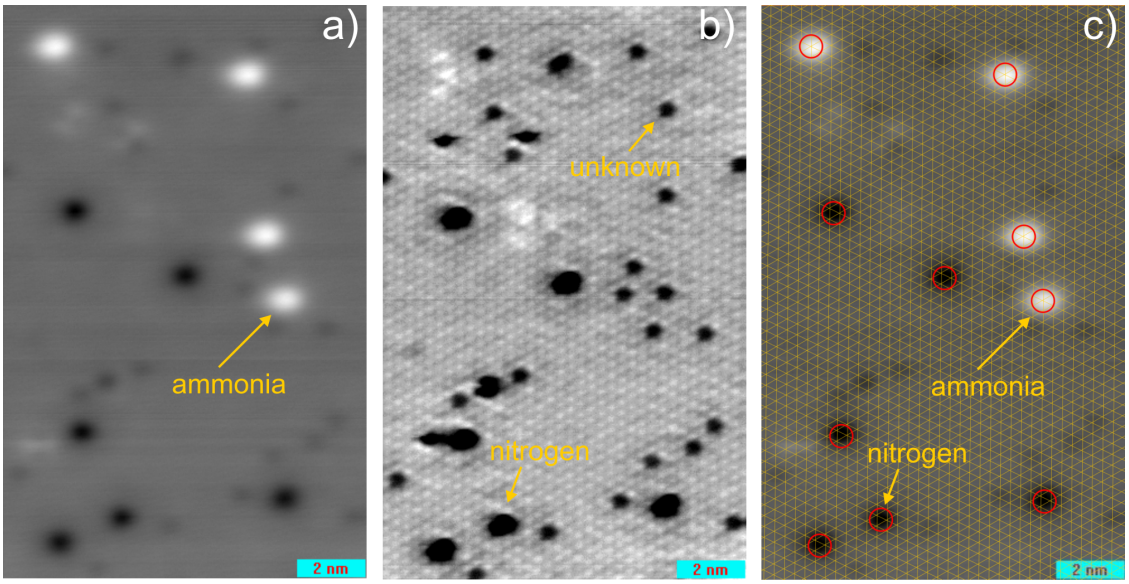

Figure 2.7: Ammonia and nitrogen without (a) and with atomic resolution (b) of the underlying Ru lattice. Scanning parameters are 8 mV, 237 pA for (a) and 8 mV, 13 nA for (b). While both species can be imaged easily at 237 pA in (a), the ammonia molecules diffuse at 13 nA in (b). In (c) the Ru lattice is superimposed on (a) by taking the on-top adsorption site of the unidentified contaminant species as a reference.

that these contaminants adsorb on-top. Due to their small dimensions, we will use them as a reference for the construction of a lattice that we superimpose on Fig. 2.7 (a). The result is shown in Fig. 2.7 (c). We find that ammonia adsorbs on-top, as predicted by theory, and the atomic nitrogen sits in fact on a three-fold hollow-site. From [Tro96] it is known that this hollow site is an hcp site.

In terms of assigning NH and NH_2 their adsorption sites from STM images, we do not have data that allows for determining the sites unambiguously. Sometimes however, the tip apex exhibits a distinct chemical composition, which is reflected in a modified imaging contrast, see Fig. 2.8. From such images, it can be deduced that NH_2 tends to align with one molecular axis along the surface directions (compare to Fig. 1.11 (a)). However, the adsorption sites for NH_2 as well as for NH are known from DFT calculations by J. K. Nørskov's group. Accordingly NH_2 and NH adsorb on a bridge and on an hcp hollow site, respectively [Log03].

Now, we come back to the analogy of N and NH to C and CH that was mentioned earlier in this chapter: in fact we observe in both cases a weaker corrugation for the hydrogenated species. We also know, that N and C, both adsorb at hcp hollow-sites. This might be further indication that NH adsorbs at an hcp site, as does CH.

We also have indication for ammonia dimer formation and splitting on Ru(0001). In our STM images we occasionally observe bright protrusions that appear higher than individual ammonia molecules. Examples are given in Fig. 2.9, on the right image in (a) and on the left image in (b), marked by a circle. When applying a voltage pulse of -5.75 V for 60 s in (a), with the position of the tip marked by the cross, we observe on the right image a single ammonia molecule at the position where the very bright protrusion once had resided. We tentatively identify this process with ammonia dimer formation. This process is reversed in (b), where a dimer is

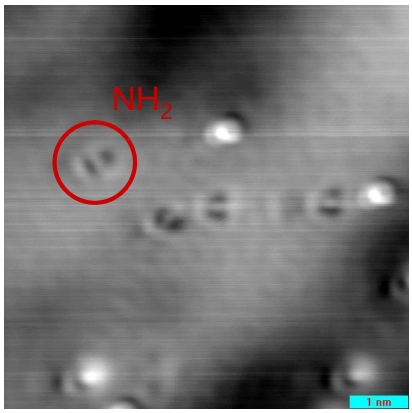

Figure 2.8: NH_2 imaged with a chemically modified tip (apex composition unknown). By comparison to Fig. 1.11 (a) it can be seen that NH_2 favors alignment of one molecular axis along the surface directions. Scanning parameters 15 mV, 21 pA.

split when applying a pulse of +8 V for a duration of 60 s. The dimer shows an apparent height of 80 pm, which is thus by a factor of ~ 1.5 greater than the height of an individual ammonia molecule. Such relatively large voltages applied over the duration of 1 min do not just locally influence the species that is located underneath the tip, but lead to diffusion, desorption and dissociation processes in the vicinity of the tip position. Such effects might be caused by the electric field between tip and sample, as will be discussed in further detail for the case of dissociation in chapter 2.2.

Fig. 2.10 (a) shows the simulated image of two ammonia molecules forming a dimer. The calculated height of 120 pm exceeds the height of a single ammonia molecule by a factor of two, as is also illustrated by the simulated image of a single ammonia molecule in (b), using the same z-scale for the two images. In the literature dimer configurations were proposed, e.g., on Pt(111) and Ni(111) [Off06, Dia09]. The mechanism that leads to ammonia dimer formation/splitting on Ru is currently under study.

In conclusion, we successively dehydrogenated an individual ammonia molecule adsorbed on Ru(0001) by means of voltage pulses within an STM junction and imaged all NH_x (x = 0, 1, 2, 3) species. Images were also simulated and match nicely the experimental data. The experimentally determined adsorption sites for initial and final state of the dehydrogenation reaction were found to be the on-top site for NH_3 and the hcp hollow site for N, in agreement with DFT calculations.

NH_3 surrounded by zero to three hydrogen atoms were observed, with hydrogen at fcc sites and each two of them two Ru lattice spacings apart. Besides, indication for ammonia dimer formation and splitting was presented, along with the dimer's adsorption configuration on ruthenium.

Theoretical method

In order to simulate STM images, DFT calculations were performed first to obtain the optimized geometries and electronic structures for a given adsorption model and for different tip structures. Our density functional theory based calculations have been performed with the SIESTA code [Sol02] under the Generalized Gradient Ap-

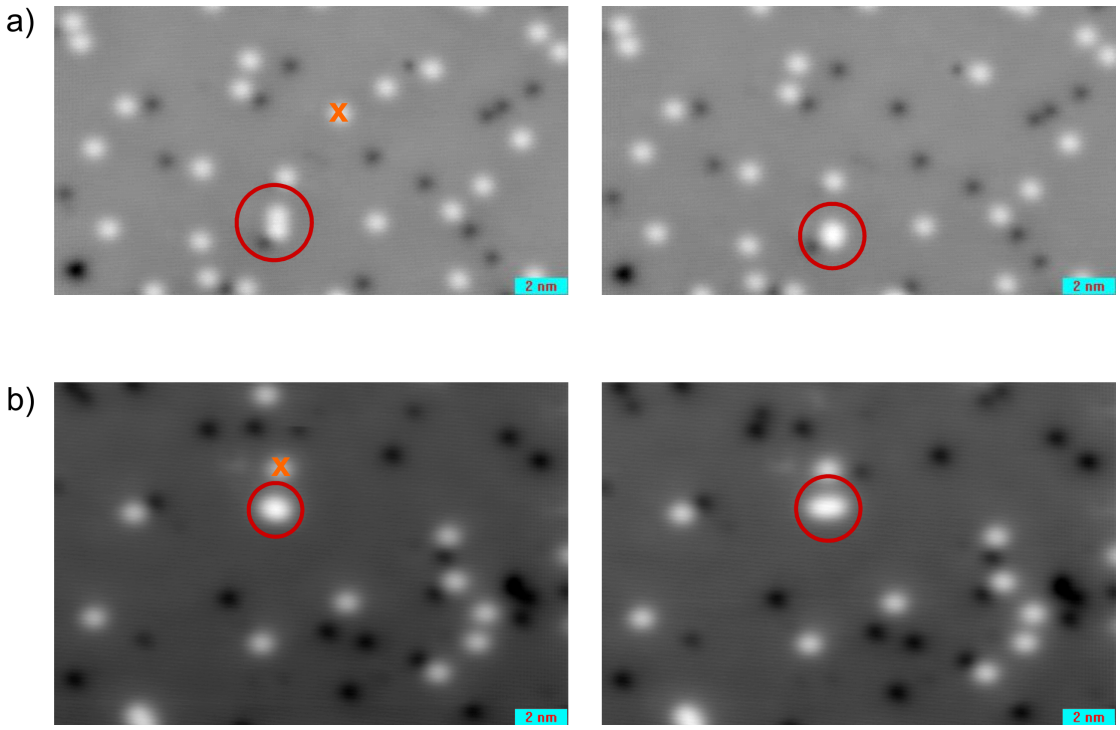

Figure 2.9: Ammonia dimer formation and splitting by voltage pulses. (a) A dimer is formed of two individual ammonia molecules after applying a voltage pulse at the position marked by x, pulse of -5.75 V for 60 s, (b) a pulse of +8 V for 60 s over x leads to ammonia dimer splitting. Scan parameters for all images: 36 mV, 12 pA.

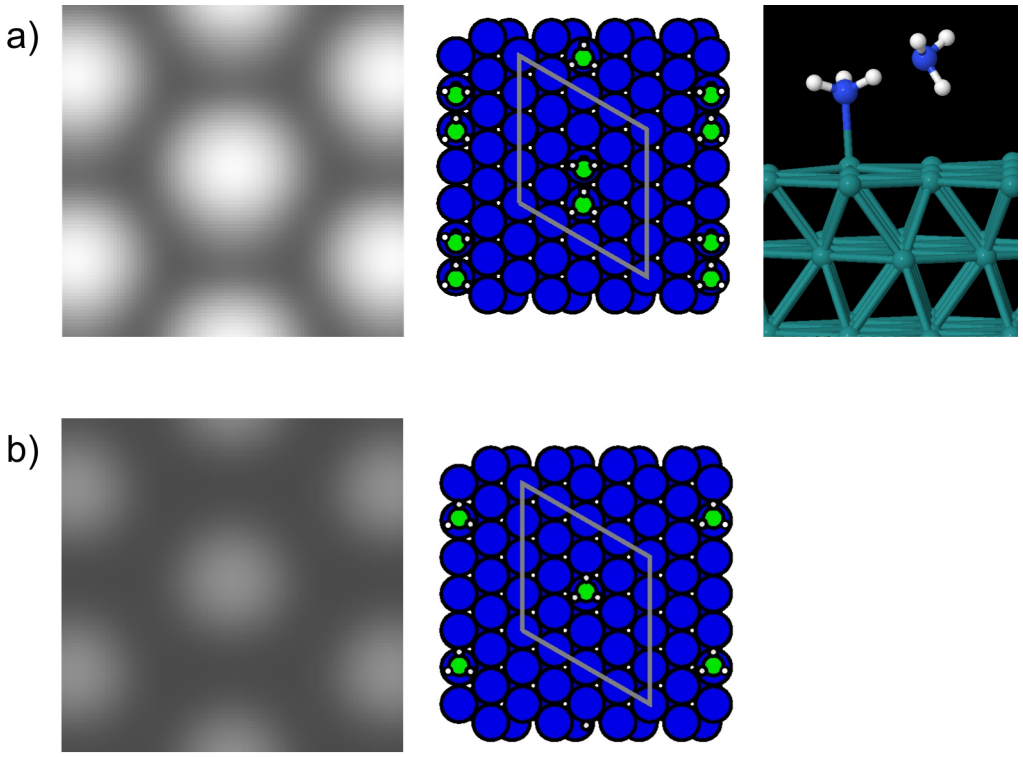

Figure 2.10: (a) Simulated ammonia dimer, compared to single ammonia molecule in (b). The dimer's contrast is brighter which corresponds to a greater apparent height.

proximation (GGA) [Per96] for the exchange-correlation part. Isolated species were modeled by slab geometries containing up to eight Ru layers along the [0001] direction with a p(4x4) unit cell. Norm-conserving pseudopotentials of the Troulliers-Martin type are employed to describe the core electrons, while the Atomic Orbital (AO) basis set was described by Double-Zeta Polarized (DZP) numerical orbitals strictly localized – we set the confinement energy to 100 meV. Real space three-center integrals are computed over a 3D grid with a resolution of 200 Rydbergs. Metastable adsorption structures are obtained after relaxing the different proposed models to local minima until forces on atoms are smaller than 0.05 eV/Å. In the minimization process, only the molecule and the first two substrate layers are allowed to relax, leaving the rest of atoms in the slab fixed to their bulk positions. For the STM image simulations we have employed the GREEN code which goes beyond the usual Tersoff- Hamann approach by explicitly considering the tip at the same level as the surface. The formalism has been described in detail elsewhere [Cer97, Jan08]. Here, we model a sharp metallic tip by a one-atom ended Pt(100) oriented pyramid stacked below a Pt(100) surface – i.e. a semi-infinite tip electrode. The other electrode comprises the molecule stacked on top of the Ru(0001) surface. The elastic current flowing from tip to sample was calculated by adjusting the apex-sample normal distance at each pixel until the desired current value was obtained. All simulations were performed assuming 100 pA fixed tunneling current and +50 mV sample bias voltage, which are typical tunneling conditions used in the experiments.

2.2 Dehydrogenation process of ammonia

In this chapter the effects of an applied electric field leading to dissociation of the NH_3 molecule are elucidated and contributing reaction mechanisms are discussed in detail.

2.2.1 Experimental evidence

As described in the previous chapter, we successfully dissociated individual ammonia molecules on Ru(0001). The questions that raise are: What kind of process favors the dissociation? Is it electronically or vibrationally induced? Does it depend on the electric field?

When applying voltage pulses over a distinct molecule, we observe that the pulse does not necessarily effect the dissociation of this particular molecule. Neighboring molecules are affected as well. Such a non-localized interaction is a first indication for an electric field-dependance of the dissociation process. Then we studied the dependence of threshold voltage for dissociation versus tip-sample distance (see chapter 1.2.3). We took into account all kinds of dissociation: starting with ammonia and leading to NH_2, NH or N, as the different dissociation products were generated by very similar threshold voltages. Recall that in case of an electric field effect, we expect a linear dependence of threshold voltage versus Δz (the distance that the tip was retracted), whereas we would not see such a dependence for a vibrational excitation. In Fig. 2.11 (a) the threshold voltages were measured for different Δz, for a positively as well as for a negatively biased sample, with voltage pulses applied for periods of 1 ms to 60 s. We clearly see a linear dependence of threshold voltage versus Δz, thus indicating an electric-field effect. Fig. 2.11 (b) links the tip polarity to the differently colored lines in (a) by means of a color code. Zero of the Δz axis does not mean that tip and sample are in contact, as Δz simply describes the retraction length from a starting point that represents a certain tip-sample distance. Slight deviations in threshold voltage are caused by different tip shapes, and are reflected in error bars. The lines for the two polarities in (a) have different slopes. If the sample is positively biased, we find a critical field for dissociation of 0.11 ± 0.01 V/Å. For a negatively biased sample, the required field has to be about three times as big, namely -0.30 ± 0.01 V/Å.

Our aim here was *not* studying the regime of very small tip-sample distances. We cannot rule out that in this regime, the data would exhibit a nonlinear behavior. However, for the shown Δz, we observed the smallest threshold voltage of ≈ 3V at $\Delta z = 0$ nm resulting in currents of several tens of nA, which corresponds to a tunneling resistance on the order of 1 GΩ. Tip retraction by 1 nm, leads to threshold voltages of 4.5 to 5 V with tunnelings currents of 10 to 200 pA. For larger Δz, the currents were lower than the noise level of ~ 1 pA, and could not be detected, i.e., the probability for electron tunneling was close to zero.

2.2.2 Electric-field dependance

Our experiments suggest that the applied electric field resulting from the STM tip induces dissociation of NH_3 on Ru(0001), hence density functional theory calculations were performed by A. Sisto and A. T. Zayak of J. B. Neaton's group at Lawrence Berkeley Lab to understand the experimental observations of this reaction in more

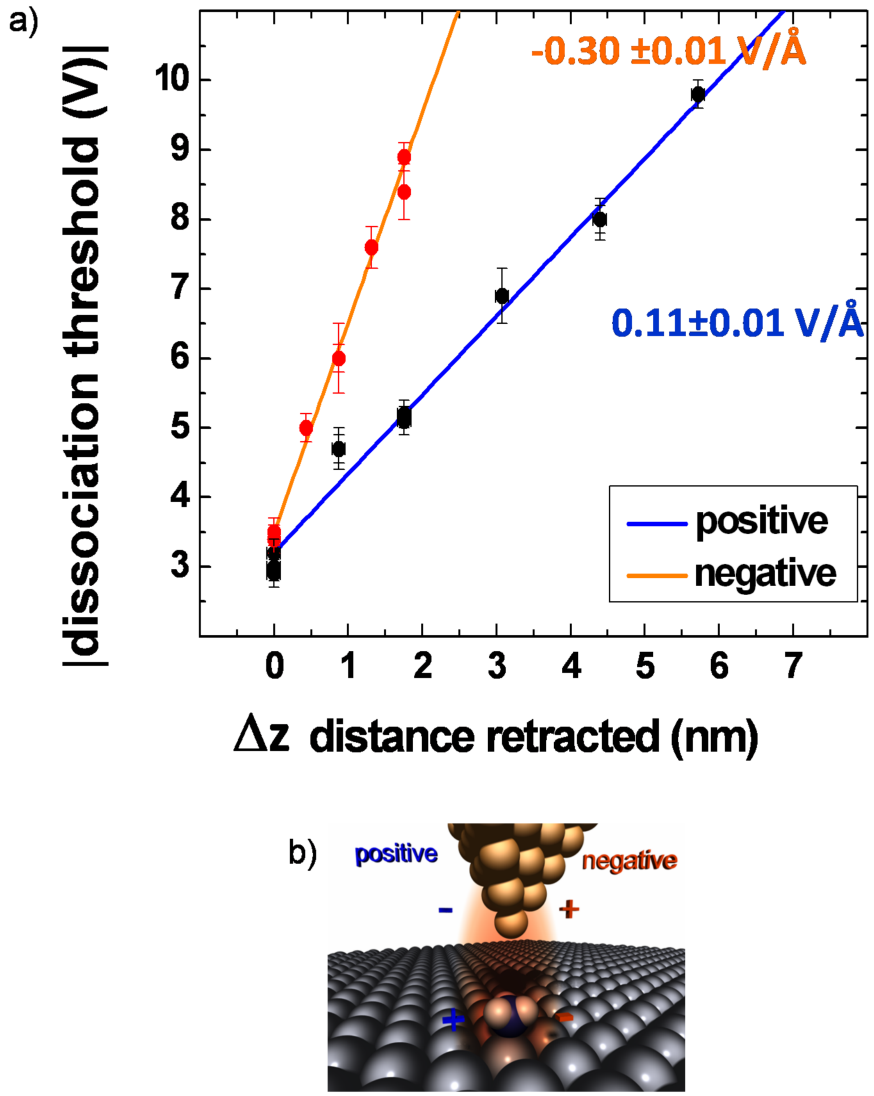

Figure 2.11: (a) The threshold voltage for dissociation of ammonia versus retracted distance Δz between tip and sample is plotted for a positively and a negatively biased sample. For the shown Δz, we find a linear dependence which suggests an electric-field induced dissociation process. Different slopes of the two lines represent different critical fields that are needed to overcome the dissociation threshold. In the case of a negatively biased sample, the required field has to be three times larger than for a positive sample bias. (b) Polarities for the tip-sample geometry with same blue and orange colors for positively and negatively biased sample, respectively, as used for the plot above.

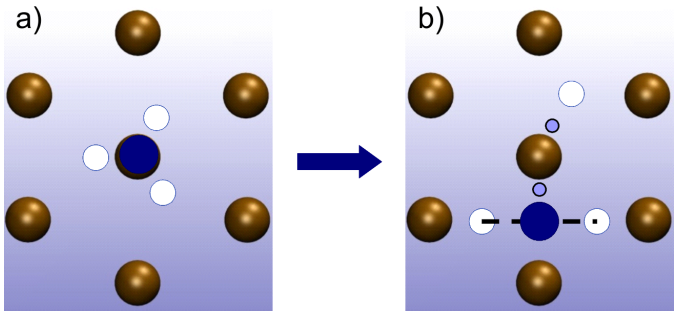

Figure 2.12: (a) The initial on-top site is a stable binding site for ammonia on Ru(0001), as calculated by DFT. (b) After dissociation, NH_2 moves to a bridge site and the hydrogen atom to a fcc hollow site. A linearly interpolated dissociation pathway is sketched.

detail. Dissociation thresholds were calculated, as well as the energy barrier along different potential reaction pathways in order to explain the initial dissociation.

DFT has been successful in accurately describing ground-state properties such as atomic geometry, lattice constants, vibrational spectra, etc. [Pay92]. Furthermore, DFT has been shown to accurately determine the reaction characteristics of NH_3 synthesis and dissociation over a Ru catalyst [Hon05, Hel09] and in analyzing vibrational excitation from inelastic electron tunneling [Lor00, Lor00b].

Density functional theory is used as implemented in the Vienna Ab-initio Simulations Package (VASP) [Kre93b, Kre94, Kre96, Kre96b], with the exchange-correlation functional in the PBE form [Per96], and PAW pseudopotentials [Blö94, Kre99]. The system is modeled as a periodic Ru slab with a coverage of $1NH_3/nm^2$. The approximation of a Ru surface as a 4 layer slab is validated quantitatively by identifying a change of less than 0.1 eV in NH_3 binding energy relative to an 8 layer slab. Periodic boundary conditions are used with a 4x4 Ru supercell with 20 Å of vacuum in the direction normal to the surface (z-direction). The plane-wave energy cutoff is set to 500 eV for relaxations and self-consistent total energy calculations. A Monkhorst-Pack integration scheme is used with a 2x2x1 k-point grid and Gaussian smearing, with a width of 0.1 eV. To model the external electric field from the STM tip, we used an external sawtooth potential varying along the z axis.

The effects of an applied electric field on the reaction pathway are examined jointly with MD simulations and static calculations. MD was done at 100 K, enabling to visualize the dissociation process on a time scale much smaller than experimentally

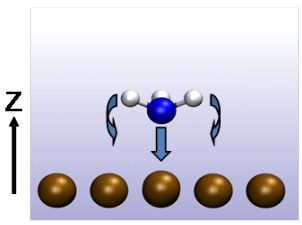

	NH_3 on-top no field	NH_3 on-top E=0.1 V/Å
r(N-Ru) (Å)	2.22	2.07
α(H-N-H)	108.6	117.6

Figure 2.13: Change in initial state with electric field: the NH_3 molecule is pulled towards the Ru surface and a widening of the H-N-H bond angle is observed.

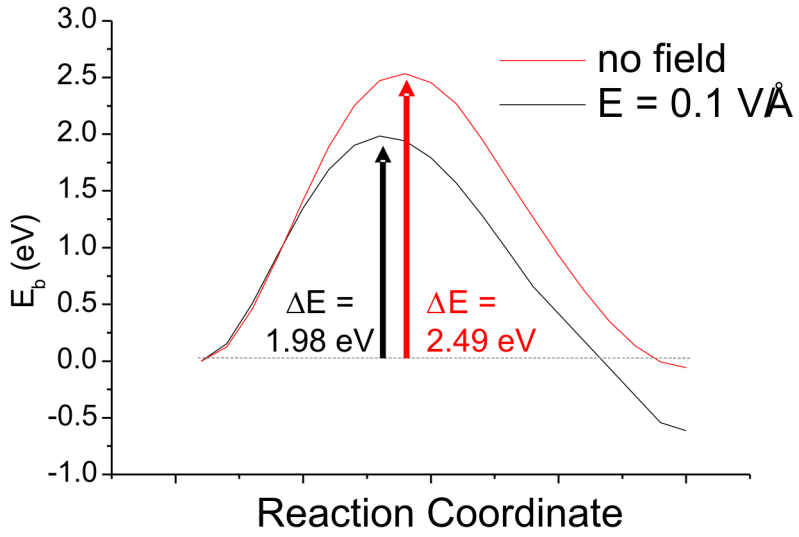

Figure 2.14: Potential energy barrier for dissociation of NH_3 along the linearly interpolated reaction pathway with and without electrical field. In the plot the initial state is to the left and the final state to the right. The chosen field of E = 0.1 V/Å reduces drastically the potential energy barrier by $\sim$ 500 meV.

observed (on the order of femtoseconds). The reason for rising the temperature in MD to 100 K (compared to 6-7 K of our experiment) is that such low temperatures are not feasible in MD due to elevated computing time when kinetics are slow. The resulting trajectory of dissociated ions is used to conduct static calculations to determine the changes in energy between the NH_3 molecule, and the dissociated constituents after applying the electric field.

Adsorption geometry

In order to explain the dehydrogenation process, the geometries for NH_x adsorption were calculated first. The calculated adsorption sites are consistent with Nørskov's results, see Fig. 2.12, and it is shown that NH_3 on-top, with its hydrogen atoms pointing towards the fcc hollow sites, constitutes a stable binding site, with a binding energy of 0.66 eV. Dissociation leads to NH_2 + H, where NH_2 is adsorbed at a bridge site and the split hydrogen at a fcc site. Further dissociation results in NH adsorbed at a hcp hollow site. The positions of the two H atoms relative to NH or each other do not significantly affect the total energy as long as they occupy fcc sites. The self-consistent total energy difference between the NH_2 and NH products relative to the NH_3 on-top site are then 0.1 and 0.2 eV, respectively, with the products at lower energies than the intact NH_3 molecule.

Positively biased sample

Ab initio molecular dynamics is used to characterize the dissociation pathway of the NH_3 molecule. An applied electric field modifies its initial state: the geometry of

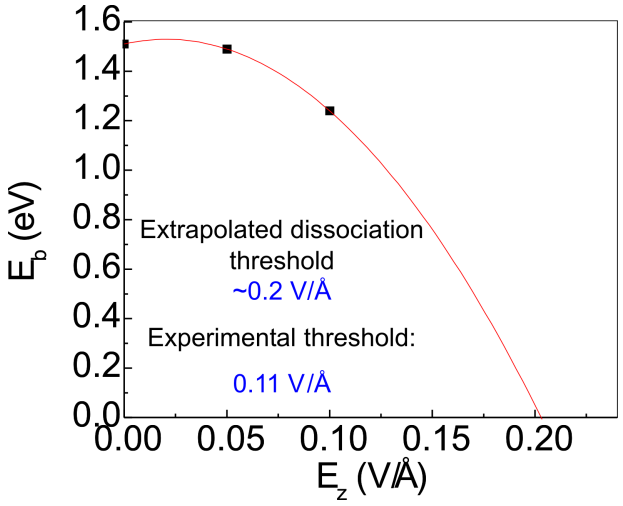

Figure 2.15: The potential barrier corresponding to the minimum energy pathway between the initial and final states is calculated using a nudged elastic band method. By extrapolation a tentative dissociation threshold of $\sim$ 0.2 V/Å for the NH_3 molecule is suggested.

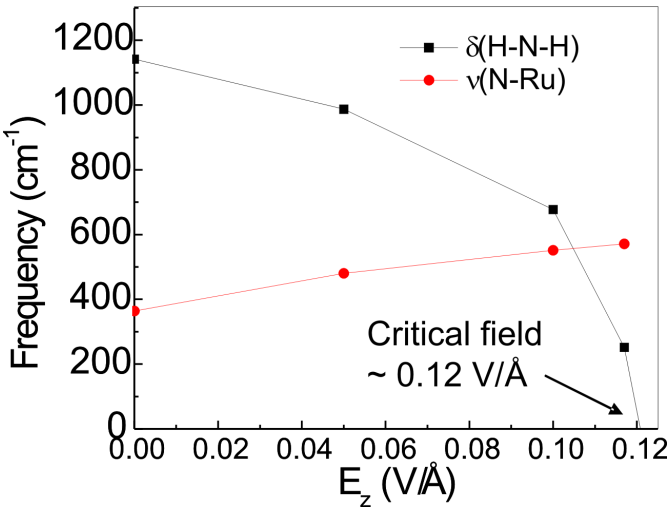

Figure 2.16: Electric field dependence of the two most contributing vibrational modes to dissociation: While the N-Ru stretching mode exhibits a slight hardening, the H-N-H umbrella mode softens tremendously. Beyond a critical field of ~ 0.12 V/Å a hybrid vibrational mode, i.e., the coupling of umbrella and N-Ru stretch mode, is formed such that the H atoms oscillate between Ru and N.

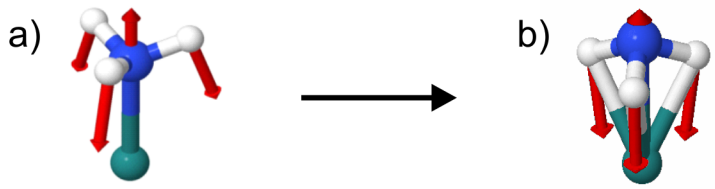

Figure 2.17: Hybrid vibrational mode formed at fields larger than 0.12 V/Å. (a) No field and (b) E = 0.15 V/Å

the perturbed system changes by widening of the H-N-H bond angle and a decrease in N-Ru bond length, relative to the unperturbed structure. E. g., a field of E = 0.1 V/Å results in an ammonia H-N-H bond angle of 117.6° and a N-Ru bond length of 2.07 Å, compared to 108.6° and 2.22 Å, if no field is applied, see Fig. 2.13.

As a proof of principle, the reaction pathway is first approximated by linear interpolation between relaxed initial and final states, as shown in Fig. 2.12. The potential barrier along this reaction pathway for an unperturbed and and a perturbed system was calculated, as can be seen in Fig. 2.14. The chosen field of E = 0.1 V/Å reduces drastically the potential energy barrier by $\sim$ 500 meV. Note that the final state is more stable than the initial state.

A more sophisticated approach is to modify the linear dissociation path and adopt it to the force profile along the way by aiming at the minimum energy path. This was done within a nudged elastic band calculation [Mar02]. Due to field-induced change in equilibrium geometry (widening of H-N-H bond angle and a decrease in N-Ru bond length) alternate pathways are created for different field strengths. In Fig. 2.15 the energy barrier is plotted versus the applied electric field. Extrapolation suggests a tentative dissociation threshold of 0.2 V/Å, in good agreement with the experimental value of 0.11±0.01 V/Å.

Within a stability analysis the relative contribution of each vibrational mode was calculated by projecting the MD dissociation trajectory onto the eigenvectors of each vibrational mode. It was found that the N-Ru stretching mode and the umbrella mode contribute significantly to the initial dissociation pathway of NH_3. Hence the field-induced change in equilibrium geometry drives the softening of the umbrella mode (and a slight hardening of the N-Ru stretching mode). The critical field of $\sim$ 0.12 V/Å indicates the field at which the umbrella mode eigenvectors disappear, corresponding to a change in orientation of the molecule. A hybrid vibrational mode, i.e., the coupling of umbrella and N-Ru stretch mode, is formed for fields larger than that such that the H atoms oscillate between Ru and N, eventually leading to dissociation, see Fig. 2.16 and 2.17.

Outlook: Negatively biased sample

Unlike the positively biased sample, calculations for the negative polarity are work in progress, namely we do understand what is happening at relatively weak fields, but the case of stronger fields is still unresolved.

For negative bias a softening of the N-Ru stretching mode of NH_3 with increasing field is proposed, whereas the umbrella mode remains relatively stable, see Fig. 2.18.

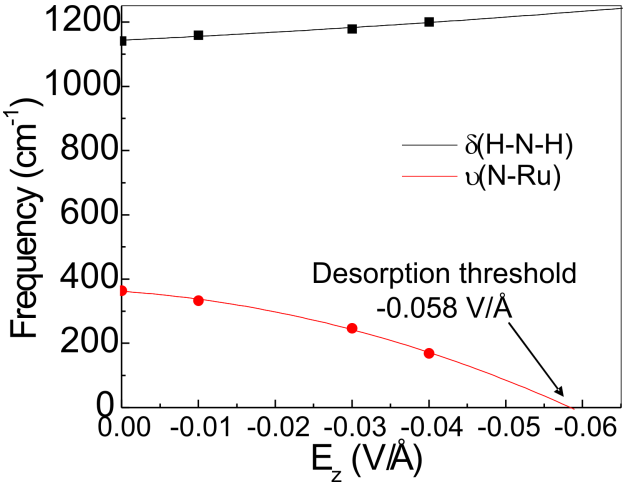

Figure 2.18: Field-dependence of N-Ru stretching and umbrella modes of ammonia with negative polarity. A softening of the N-Ru stretch mode is found, ultimately leading to desorption of the molecule at fields greater than -0.058 V/Å.

As a result desorption of the molecule occurs at fields greater than -0.058 V/Å, and the following desorption mechanism is suggested: the H atoms are initially pulled upward, while their N-H bond lengths stretch, until reaching their maximum length. Due to increasing restoring N-H forces, the N atom is forced upward, too, and the molecule eventually desorbs, see Fig. 2.19. The negative polarity thus reduces the interaction strength between surface and molecule. Experimentally, desorption was indeed observed for smaller fields. However, we did not aim at systematically conducting desorption experiments.

We tentatively suggest that dissociation becomes favorable at larger fields due to field-enhanced momentum of the H atoms relative to N, with the dissociated H atoms desorbing into vacuum, see Fig. 2.20. The process of stripping the hydrogen off the molecule is thus less assisted by the surface than the dissociation mechanism in case of the positive polarity is. Due to this reduced interaction at negative sample bias, the required field for dissociation is higher than for positive bias, in agreement with the experiment (see Fig. 2.11).

In conclusion, we measured the effect that an applied electric field within a STM junction has on the dehydrogenation of an individual ammonia molecule adsorbed on Ru(0001). We observed a linear dependence for dissociation threshold voltage versus tip-sample distance Δz, which indicates an electric field effect for large Δz. The critical fields required for dissociation were of 0.11 ± 0.01 V/Å and -0.30 ± 0.01 V/Å for a positive and a negative sample, respectively.

DFT calculations jointly with MD simulations studied the effects of an applied electric field on dissociation barriers and thresholds along different reaction pathways in order to explain the initial dissociation. These calculations distinguished between positive and negative sample bias.

For positive polarity it was found that softening of the umbrella mode due to the electrical field leads to an instability in equilibrium geometry such that the ammonia molecule is pulled towards the Ru surface and the N-H-N angle widens. The applied electric field also greatly enhances the dissociation reaction rate through a reduction

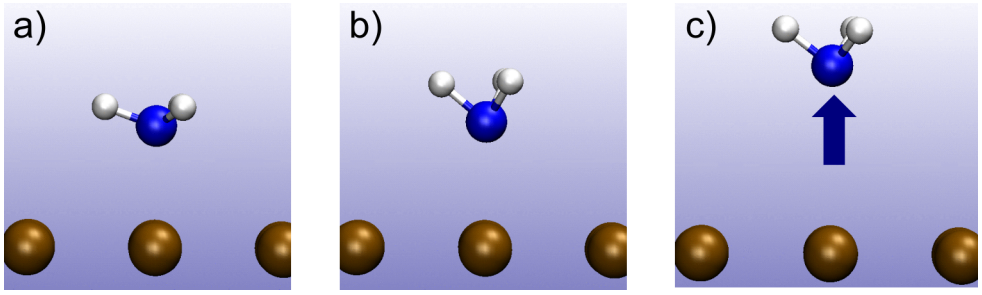

Figure 2.19: Desorption mechanism for negatively biased sample. (a) An electric field is applied, and the H atoms initially forced upward, (b) N-H bond length increases to a maximum, (c) N atom is pulled upward.

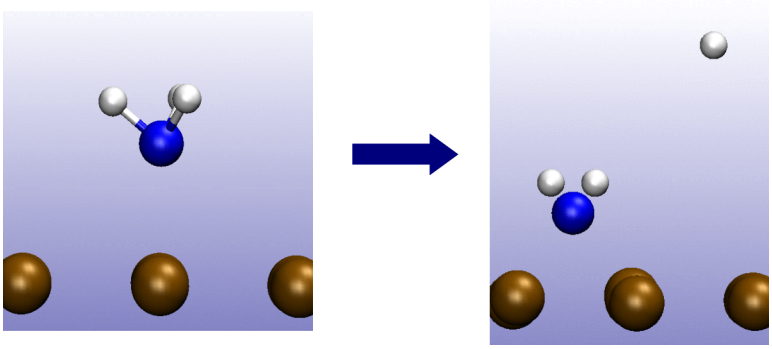

Figure 2.20: Dissociation pathway for negative polarity: the initial state of NH_3 on-top shows maximum N-H bond length (left). Final state of NH_2 at a bridge site with the dissociated H desorbing into vacuum.

of the reaction energy barrier. An extrapolated dissociation threshold of 0.2 V/Å is found, that agrees well with the experimental value.

Calculations for the negative polarity are still running. What we understood so far is that for a negative sample bias the ammonia molecule interacts less with the surface. Smaller fields cause desorption of the molecule at fields strengths greater than -0.058 V/Å, following the softening of the N-Ru stretch mode. Dissociation becomes favorable at larger fields. The mechanism of this process has yet to be resolved.

3 Water wetting and ice growth

At metallic interfaces, the nucleation of ice and in general the interactions of water with surfaces are of great scientific interest, especially regarding catalysis, electrochemistry, and corrosion. Prerequisite for extensive ice growth is surface wetting, i.e., the formation of a two-dimensional water layer due to the surface's strong affinity for water. An understanding of the arrangement of the water molecules is largely contingent on atomic-scale surface structure and composition. Among the questions that rise are the following:

Does water wet the surface completely? Does it dissociate upon adsorption? More specifically for our focus: how does ice grow on hexagonal precious metal surfaces, and does an icelike wetting layer ever exist? What happens if we do not deal with atomically clean metal surfaces, but with more stable materials that are present in ambient conditions, e.g., metals precovered with an oxygen or graphene layer – does this impact the wetting process?

In this chapter, we start with investigating the structure of the first two layers of water on hexagonal metal surfaces, as these layers provide the structural template that guides the growth of ice at the material-water interface. Ru(0001) and Pd(111) constitute model systems for water adsorption. The lattice mismatch with ice I_h amounts for just 4.2 % and 5.8 % for Ru and Pd, respectively [Fei10]. This mismatch can be compensated by straining the hydrogen bonds to fit the metal lattice constant, e.g. on Pd(111) the first layer grows according to the two dimensional ice rules [Cer04]:

1. Oxygen atoms bind to metal atoms through the O-lone pair
2. Maximization of number of H bonds: no dangling H
3. Cluster terminates when 1. and 2. cannot be fulfilled

Ideally a molecule will donate one or two H-bonds while accepting one, which corresponds to the maximum H-bonding possible in 2D. The question why cluster growth on metal surfaces is limited to small sizes at low temperature is answered by the two-dimensional ice rules. Fig. 3.1 schematically shows water clusters of side-sharing hexagons, obeying the ice rules. In contrast to 3D ice which in principle can grow indefinitely (see chapter 1.2.2), in two dimensions water growth only occurs in small clusters or narrow stripes. Beyond the hexamer, each additional hexamer must have at least one "defect" molecule of double-acceptor nature with its plane nearly vertical to the surface. The energy cost for defects is larger at internal vertices than on the cluster periphery. As is shown in Fig. 3.1 stripes wider than three hexagons or extended clusters require two or three defect molecules per hexagon. When minimizing the defect energy cost, stripe structures are formed by water on Pd(111) and Ru(0001) at low temperature [Tat09].

Now we take a more detailed look at the first wetting layer on a hexagonal crystal face, e.g., Ru(0001). The classical picture is that of an ice-like bilayer, i.e., similar

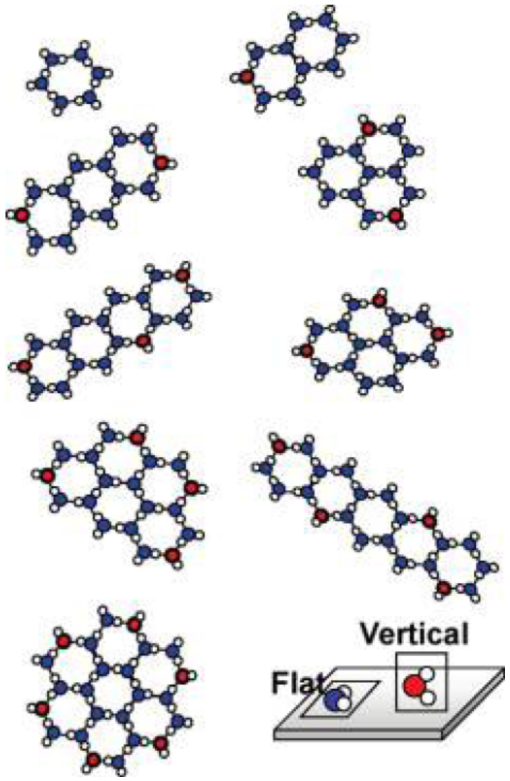

Figure 3.1: Why is cluster growth on metal surfaces like Pd(111) and Ru(0001) limited to small sizes at low temperature? The schematic drawings show water clusters of side-sharing hexagons. The clusters obey so-called "2D ice rules". These rules require maximization of O-metal bonding and H-bonding to adjacent molecules. Ideally a molecule will donate one or two H-bonds while accepting one, the maximum H-bonding possible in two dimensions (blue colored "flat" molecules parallel to the surface). Beyond the hexamer (top left), each additional hexamer must have at least one "defect" molecule of double-acceptor nature with its plane nearly vertical to the surface (red colored molecules). Each defect has an energy cost, which is higher at internal vertices than on the cluster periphery. Minimizing the defect energy cost gives rise to the observed stripe structures formed by water at low temperature [Tat09].

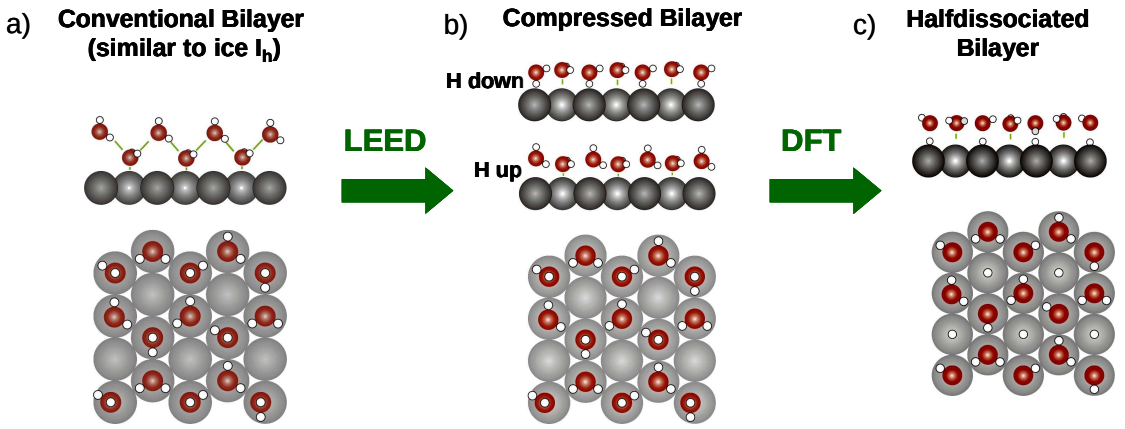

Figure 3.2: Different models for first-layer water adsorption on Ru(0001). (a) Conventional bilayer, that is similar to ice I_h, with a distance of $\sim$ 0.8 Å between the two levels of the bilayer. (b) LEED experiments found nearly co-planar oxygen (with a buckling of $\sim$ 0.1 Å) , and not a bulk-like bilayer [Hel94]. (c) DFT shows that the *complete* wetting layer on Ru(0001) has to be a half-dissociated monolayer [Fei02].

to ice I_h, see chapter 1.2.2. Three water molecules of each hexagon are adsorbed via their oxygen atoms to Ru and linked by hydrogen bonds to another three molecules in the upper half bilayer, with a distance of $\sim$ 0.8 Å between the two levels of the bilayer, see Fig. 1.13 and 3.2 (a). Though it has been a paradigm for decades, definitive evidence for the puckered bilayer remains to be uncovered [Fei10]. Experiments using LEED found nearly co-planar oxygen (with a buckling of only $\sim$ 0.1 Å), and not a bulk-like bilayer [Hel94], see Fig. 3.2 (b). This compressed bilayer manifests unsatisfied hydrogen bonds in the upper bilayer, either dangling into the vacuum or pointing down towards the Ru surface, hence the construction principle of a bilayer is still correct. Then DFT came into play, showing that a *complete* wetting layer on Ru(0001) cannot be formed of undissociated water molecules [Fei02], see Fig. 3.2 (c). Instead a half-dissociated monolayer forms, wherein water molecules and hydroxyl fragments are hydrogen-bonded in a hexagonal structure and hydrogen atoms bind directly to the metal. In Fig. 3.3 the energy diagram for H_2O bilayer adsorption and dissociation on Ru(0001), derived from DFT calculations is shown [Mic03]. In agreement with the model of the half-dissociated monolayer mentioned above, it was found that this partially dissociated OH+H_2O overlayer (Fig. 3.3 (d)) is in fact energetically favored over pure intact bilayers (Fig. 3.3 (a)), and the barrier to dissociate a H_2O incorporated in a bilayer was calculated and amounts for 0.5 eV. By removing the chemisorbed H atom and adsorbing it at a fcc site in a separate ($\sqrt{3}$x$\sqrt{3}$)R30° unit cell, a further 0.45 eV can be gained, although it remains unknown if this is possible in practice.

Knowing the structure of the first layer is just the first step in understanding the wetting behavior of a metal. As crucial as the nature of the surface-water interaction, are water-water interactions of the subsequent layers for eventually creating three-dimensional bulk ice, that is grown on a metal surface. And thus second-layer growth is the topic of the chapter following the first water layer.

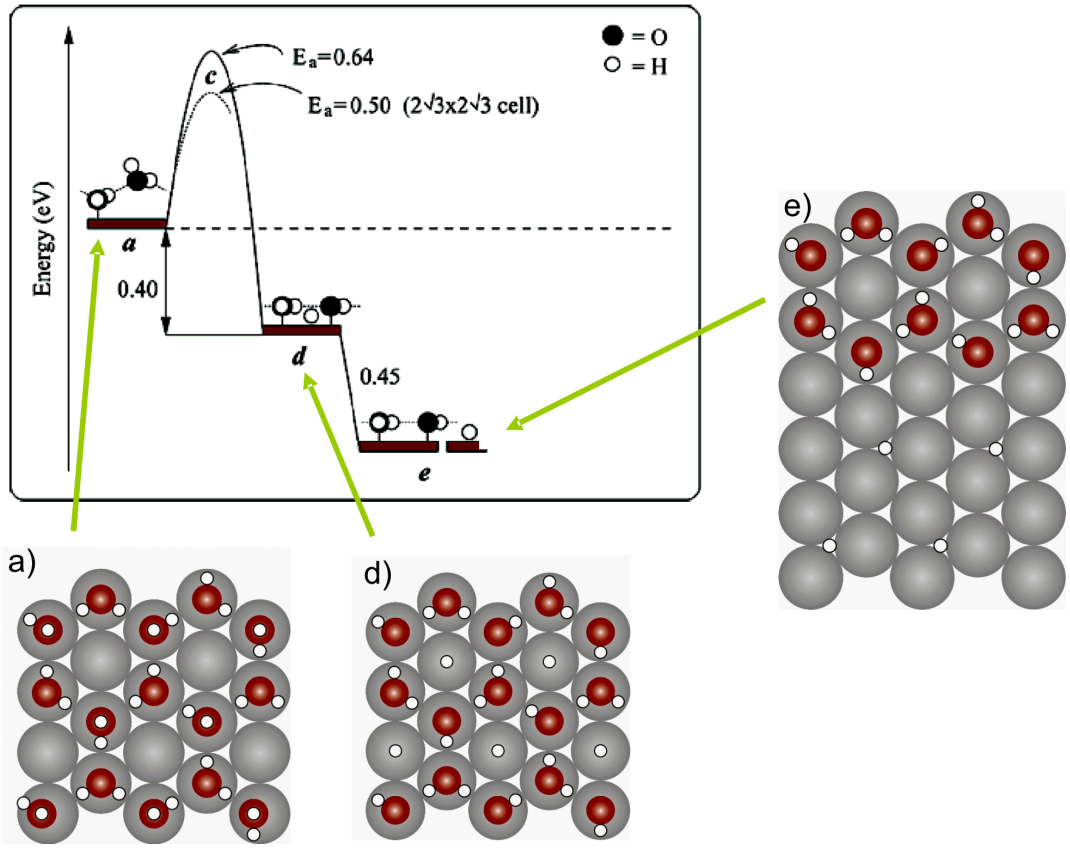

Figure 3.3: Energy diagram for H_2O bilayer adsorption and dissociation on Ru(0001) [Mic03]. a) Intact molecule adlayer, d) half-dissociated adlayer with H at atop sites, e) half-dissociated adlayer with H removed to fcc sites of a separate (√3x√3)R30° unit cell. An energy barrier of $\sim$ 0.5 eV has to be overcome to get from an intact adlayer to a half-dissociated layer.

3.1 Mixed water-hydroxyl structures

Numerous experimental and theoretical studies have been performed on the adsorption of water on hexagonal metal surfaces including ruthenium and palladium with the aim at understanding its structure and growth [Ver06, Ito08]. One goal of these studies is to determine whether water adsorbs intact or as a partially dissociated overlayer. Density functional theory calculations proposed that a partially dissociated layer, consisting of a mixture of OH, H and H_2O, is the most stable water structure on Ru(0001) [Fei02, Mic03]. Different experimental studies, including thermal desorption, vibrational spectroscopy and scanning tunneling microscopy among others, have shown that at low temperatures water adsorbs forming a metastable phase of intact molecules [Tat09, Haq06, Cla04, And04]. The transformation of this metastable phase to the stable partially dissociated phase requires overcoming an activation barrier of 0.5 eV, e.g., by thermal activation [And04, Wei04, Tat08]. Weissenrieder et al. [Wei04] showed experimental evidence for partially dissociated water on Ru(0001) by means of photoelectron spectroscopy. The temperature above which partial dissociation was observed covers a broad range between 104 K [Wei04] and 150 K [Cla04]. The complete dissociation to atomic oxygen was observed near 190 K [Wei04]. Alternatively, partial dissociation of water on ruthenium occurs upon electron and x-ray irradiation [Haq06, And04, Wei04, Tat08, Far05]. The question whether or not D_2O partially dissociates on ruthenium is still under discussion [Cla04, Far05, Gla08, Men05, Den03].

STM allows for investigating the molecular structure of water and mixed water-hydroxyl clusters with high spatial resolution while avoiding beam-induced dissociation. Yet this technique helps understanding the role of electrons during the dissociation process due to the fact that the bias voltage between tip and sample can be tuned to excite vibrational modes of the molecule under study which may lead to dissociation. It has been found that many reactions involving isolated water molecules on Ru(0001) are triggered by excitation of the O-H stretch mode ($\sim$ 450 mV) [Mug09]. Tatarkhanov et al. [Tat08] used STM and X-Ray absorption spectroscopy (XAS) combined with density functional theory calculations to describe the cluster structures after partial dissociation of water on ruthenium. They observed that the mixed water-hydroxyl structures form elongated and narrow stripes, 2.5 to 6 ruthenium lattice distances wide, showing an internal honeycomb structure. This is drastically different from the extended H-bond network models put forward previously [Mic03, Tat09, Mat05], but agrees with different models derived from low energy electron diffraction (LEED) above 150 K [Haq06, Doe82, Hel95].

Here we present a study of intact and partially dissociated water monolayers on Ru(0001). First we will discuss the structural changes of the water clusters involved in the transition of intact to partially dissociated water. Then we focus on the location and adsorption site of the hydrogen produced during partial dissociation.

3.1.1 Thermal evolution of water from intact to partially dissociated layers

Fig. 3.4 shows a series of different intact and partially dissociated first-layer water structures formed after annealing at various temperatures between 110 K and 138 K. Annealing to 110 K for 7 min produced small round-shaped islands of 2-3 nm

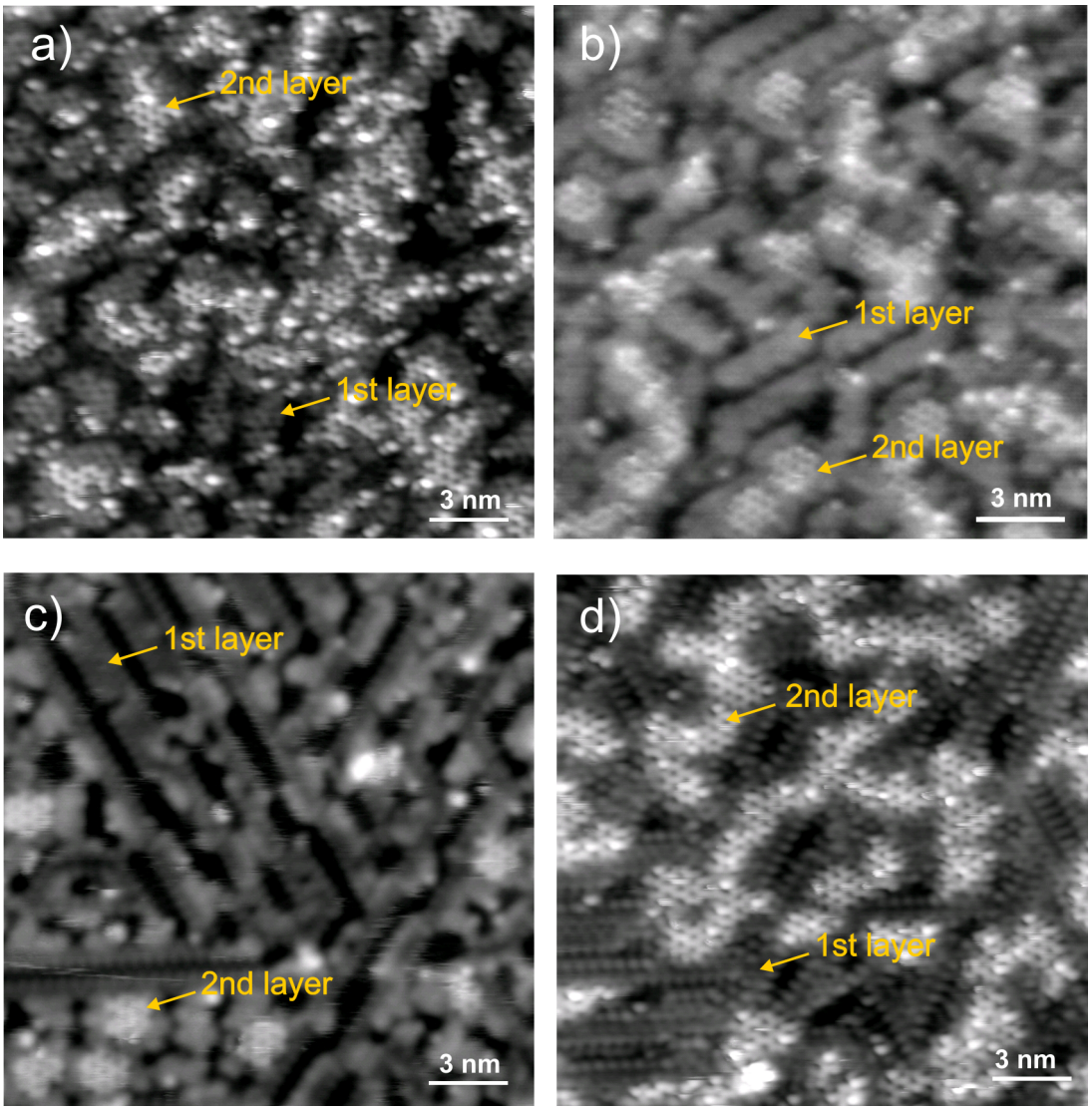

Figure 3.4: Thermal evolution of intact and partially dissociated first-layer water structures on Ru(0001). On top of the first layer (dark in imaging contrast), second-layer water hexamers (bright) are adsorbed, rotated relative to the first-layer hexagons, which will be subject of chapter 3.2. (a) Round-shaped intact first-layer water islands after 7 min of heating at 110 K, -72 mV, 11 pA, (b) stripe-like intact first-layer water clusters after 6 min at 128 K, -42 mV, 35 pA, (c) mixture of intact and partially dissociated first-layer water structures after heating at 132 K for 40 min , -89 mV, 63 pA, (d) entirely partially dissociated first-layer water after heating at 138 K for 50 min , -82 mV, 12 pA.

diameter, as shown in Fig. 3.4 (a). Annealing to 128 K leads to the formation of narrow stripes, 2-3 hexagonal units wide, see Fig. 3.4 (b). In both preparations, water does not wet the surface entirely. In addition, a few clusters of the second layer grew on top of the first layer. Water molecules of the first layer form a hexagonal network with a ($\sqrt{3}$x$\sqrt{3}$)R30° reconstruction. The structure of the second layer is also hexagonal, but surprisingly, its orientation relative to the first is rotated and will be described in chapter 3.2. Water molecules located at the edge of first-layer water clusters appear brighter. Their number is minimized after formation of narrow stripes. These edge molecules correspond to water molecules attached to hexamers that are not incorporated into the cluster [Tat09].

The preference for small clusters in form of narrow stripes, lace and rosette-like structures during water growth was described previously for Pd(111) [Tat09, Cer04]. These structures have been explained by invoking the two-dimensional ice rules for submonolayer coverage of water. According to these rules, water forms a two-dimensional hydrogen-bonded network, mostly comprised of planar hexamer rings of nearly flat-lying water molecules, where each molecule donates two hydrogen bonds and accepts one. Bonding to the metal substrate occurs through the O-lone pair. However, a defect-free extensive network consisting only of flat-lying water molecules cannot be formed unless some of the molecules change from planar to nearly vertical orientation, either with the non-H bonded hydrogen pointing up or down [Tat09]. In order to minimize the number of nearly vertical molecules, stripe-like patterns are favored. Thin stripes, one or two hexamers wide, can be formed by including one vertical molecule per hexamer. Wider islands in two dimensions require two or three additional vertical molecules per hexamer. Our experiments show that on Ru(0001) such stripe structures of intact water form after heating at about 130 K, shortly before the onset for dissociation is observed. The temperature required to form stripes on Ru(0001) is higher than on Pd, where stripes composed of flat lying molecules are already formed at 80 K and lower [Tat09].

At temperatures below 115 K we observe small two-dimensional clusters, 2-3 nm wide (Fig. 3.4 (a)). Since the dimension of these islands exceeds two to three water hexamers, water molecules with vertical planes are incorporated in the interior of the clusters by accepting two H-bonds and donating one to a neighboring molecule. The formation of an entire intact water layer with half of the molecules being flat and half vertical requires energy which can be provided by heating. Although formation of water films with coverage of two third of a monolayer were previously reported [Cla04, Doe82], our experiments indicate that in the case of ruthenium extensive heating around 130 K transforms the 2-3 nm wide structures to even narrower intact water structures in the form of stripes. These stripes act as a precursor for partial dissociation, what can be seen in the structural change of the water clusters after heating above 130 K in Fig. 3.4 (c)-(d). Our experiments agree with previous studies [Cla04, And04, Wei04, Tat08] suggesting that heating results in breaking of the OH-bond of the vertical molecules not participating in H-bonds with neighboring molecules such that a mixed H_2O-OH structure forms. Another factor which leads to small islands and hinders the formation of an entire wetting layer is the presence of preadsorbed hydrogen on the surface which is difficult to avoid even in ultra-high vacuum due to hydrogen adsorption from the background. Furthermore, it has been reported that besides the temperature the adsorption rate is also important to enable growth of well-ordered ice-layers [Gle97]. Compared to studies which observed full

wetting layers [Haq06] our adsorption rate was a factor of 2-25 faster (1-12 ML/min), which might influence the size of the water clusters on the surface.

In Figure 3.4 (c), the surface was annealed to 132 K for 40 minutes and shows some clusters in form of stripes of up to 30 nm in length, which are also observed after heating to 145 K (Fig. 3.4 (d)). These stripes have the same internal structure as the partially dissociated water stripes reported by Tatarkhanov et al. [Tat08], while the smaller structures with a slightly brighter contrast are remaining intact water clusters.

The STM image in Fig 3.5 (a), recorded after deposition of water at 145 K, shows similar intact water structures as in Fig. 3.4 (b) where the surface was heated to 127 K. After further annealing at 145 K for 30 more minutes partial dissociation was observed, Fig. 3.5 (d). These results indicate that the temperature onset for partial dissociation strongly depends on the annealing time, as is expected from a kinetically limited reaction. This explains the wide range of dissociation temperatures, from 104 K [Wei04] to 150 K [Cla04], as reported in the literature.

The molecularly resolved STM images in Fig. 3.5 (b) and (e) provide more structural information about the orientation of the linearly elongated water clusters before and after partial dissociation. The hexagonal network and the absence of atomic hydrogen around the stripes in (a) and (b) indicate that the water is intact immediately after adsorption at 145 K. The orientation of the intact stripes in (a) and (b) follows the compact atomic rows of the ruthenium lattice and the water hexamers form a (√3x√3)R30° network with armchair edges, see 3.5 (c). In contrast, the mixed water and hydroxyl stripes in (d) and (e) are oriented along the √3 directions with zigzag edges, see 3.5 (f). In all cases the orientation of the hexamers formed by intact water or by mixed H_2O/OH retains the (√3x√3)R30° orientation. The change of stripe orientation suggests that the water molecules rearrange and diffuse on the surface either before or after dissociation and that the dissociation process does not only involve bond breaking.

3.1.2 Adsorption site of hydrogen produced upon partial dissociation of H_2O

High-resolution STM images do not only allow for studying the mixed water-hydroxyl structures but also to determine their location. Fig. 3.6 shows an overview of a partially dissociated water layer consisting of mixed water-hydroxyl stripes with widths ranging from 2.5 to 4 lattice constants. Tatarkhanov et al. [Tat08] previously reported widths from 2.5 to 6 lattice constants for partially dissociated water clusters. Wider stripes have incorporated more OH per unit cell. If more hydrogen bonds have to be broken, more energy is needed to create wider partially dissociated clusters. Hence, wider structures are preferentially built at higher temperatures or longer annealing times.

The space on the surface between the mixed water-hydroxyl structures is occupied by depressions that are $\sim$ 10 pm deep and seen as dark spots on the images. This is in accordance with the experimentally observed and theoretically calculated STM topography of atomic hydrogen [Shi08]. Fig. 3.7 shows a detailed image of two water-hydroxyl stripes separated by two rows of hydrogen atoms in a (√3x√3)R30° geometry. This structure has been reported earlier for low hydrogen coverage on Ru(0001) [Tat08b, San93, Sok91], while for higher coverages (1x1) structures have

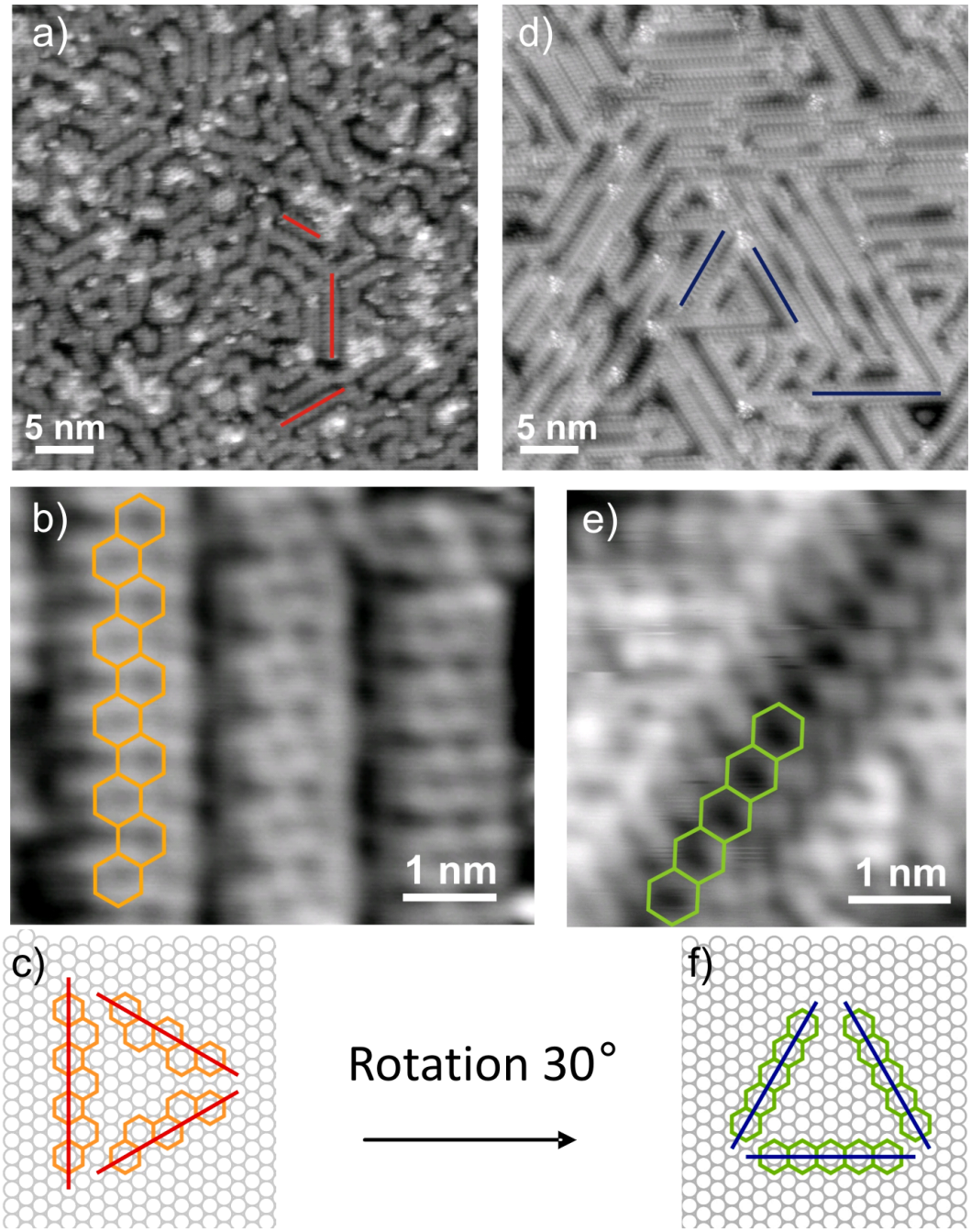

Figure 3.5: (a) Intact first-layer water stripes that align along the compact atomic rows of the Ru surface (with little amount of 2nd-layer hexamers). Image taken after adsorption at T = 145 K, -144 mV, 25 pA, (b) detail of (a) showing the hexamers that form the stripes, (c) atomic model for structures observed in (a) and (b), displaying armchair edges of a (√3x√3)R30° network. (d) Complete partial dissociation is recorded after 30 more minutes of heating at 145 K. The partially dissociated stripes are rotated by 30° relative to the compact atomic Ru rows, -51 mV, 22.2 pA. (e), (f) Zigzag edges of the (√3x√3)R30° structure are found. The Orientation of the stripes is thus a simple criterion to determine whether or not the first water layer on Ru(0001) is intact or dissociated.

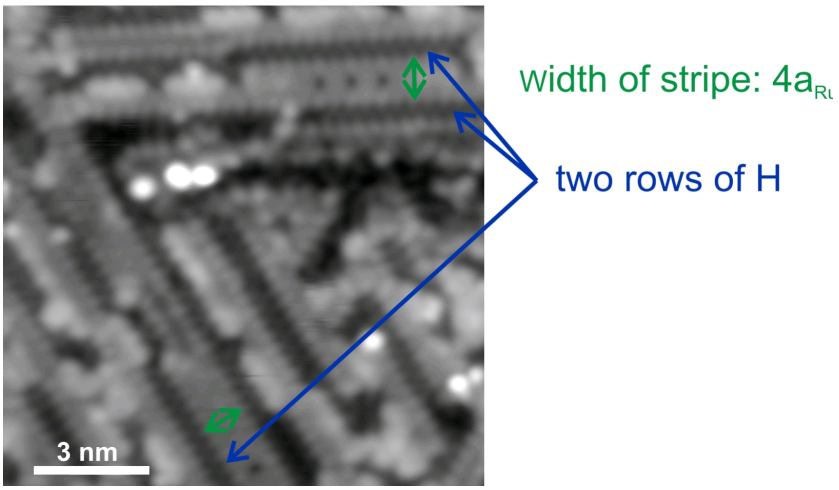

Figure 3.6: Overview of a layer of partially dissociated water. The mixed water-hydroxyl stripes have widths ranging from 2.5 to 4 ruthenium lattice spacings. Between the stripes we observe two rows of hydrogen adsorbed in a (√3x√3)R30° structure (compare Fig. 3.7 (a) for a high resolution image). Parameters: Heated to 132 K, -6 mV, 103 pA.

been observed [Tat08b, Dan78, Kos04]. The experiment indicates a three-fold hollow site for hydrogen adsorption. DFT calculations confirm the three-fold fcc site as the most stable site, in agreement with previous findings [Sok91, Kos04]. Each stripe next to the two rows of H atoms contains an OH group in each repeating unit cell. Although the OH groups can be placed in various sites of the cell satisfying 2D H-bonding and O-bonding to the substrate, DFT calculations by J. Cerdá (see chapter 2.1) suggest that the configuration in Fig. 3.7 (c), with the OH deeper inside the cluster is more stable than the one in (d) where OH is located towards the periphery of the mixed water-hydroxyl structures. From STM images however, one cannot determine the location of OH since the tunneling contrast is nearly identical to the one of the intact molecules within the cluster.

Fig. 3.7 (a) confirms the segregation of hydrogen out of the OH/H_2O lattice, which leads to the formation of domain structures. This is drastically different from the extended H-bonding networks discussed previously by theoretical models [Fei02, Mic03, Mat05], but agrees with LEED measurements [Haq06, Doe82, Hel95] and STM measurements [Tat08]. For a complete monolayer the hydrogen-bonded hexagonal network would contain the hydrogen chemisorbed on a top site in the center of each hexagon. If the hydrogen is removed from the center of the hexagonal cell and adsorbed at its preferred fcc site, an energy of 0.45 eV is gained, as shown by DFT calculations [Mic03], thus the H-centered structure is only metastable.

Fig. 3.8 shows a high-resolution image of a partially dissociated water stripe, where the centers of some hexagonal cells feature different contrasts. This indicates that these cells contain some atomic species adsorbed in the center, which can only be a hydrogen atom due to the very confined area that does not allow for adsorption of H_2O or OH. These results corroborate the partially dissociated structure proposed by Feibelman [Fei02], even if it is metastable. Hydrogen atoms located in the center of the H_2O-OH hexagons were also observed for lower coverage, prepared by dosing H_2O at 180 K, as depicted in Fig. 3.9. For this preparation the coverage of carbon

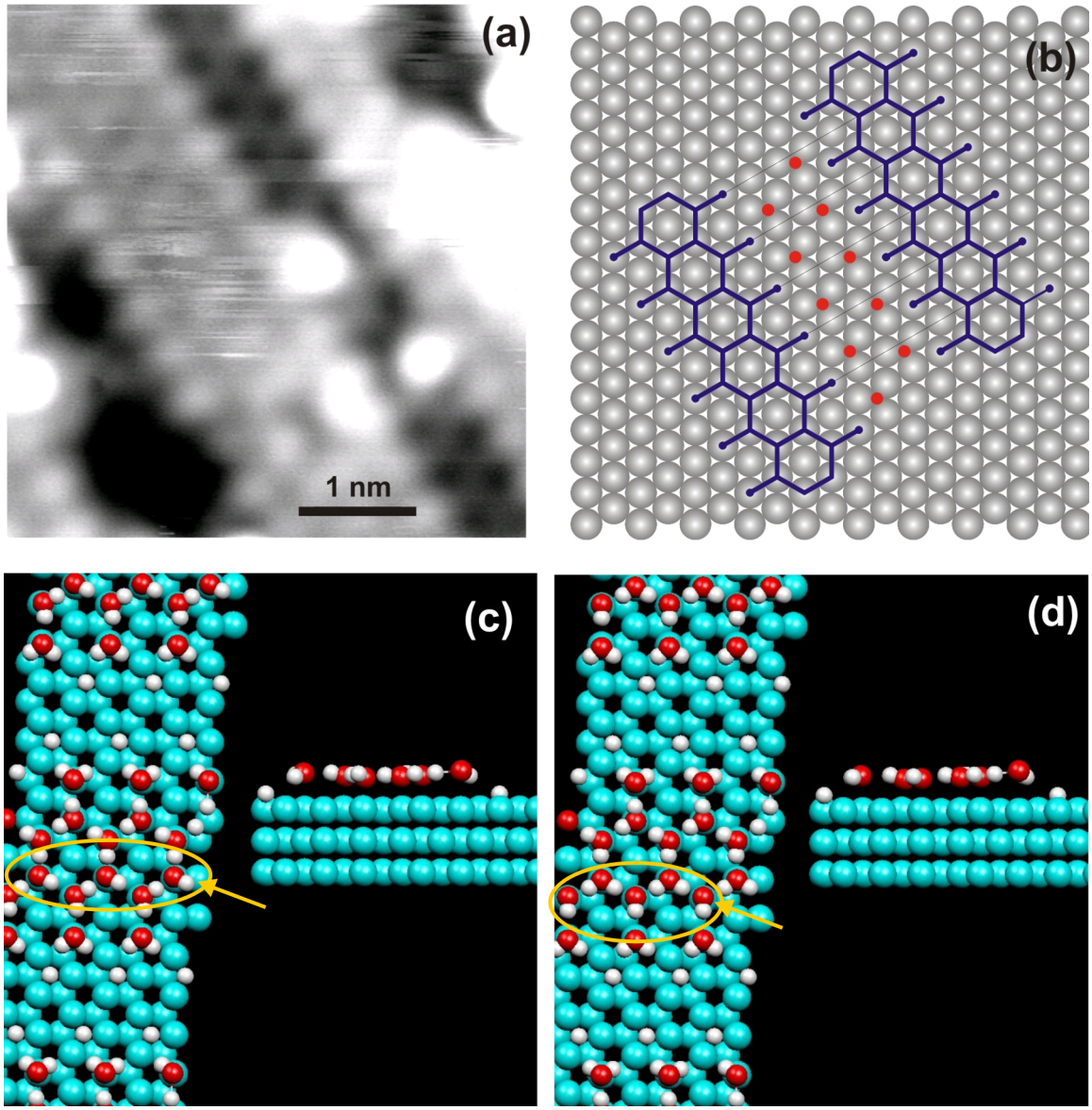

Figure 3.7: (a) High resolution STM image showing the adsorption of hydrogen in a (√3x√3)R30° structure between partially dissociated water stripes, (b) schematics of the hydrogen and H_2O/OH arrangement in (a). (c)-(d) DFT calculations of partially dissociated water clusters with hydrogen in the interspace. Parameters: heated to 132 K, -69 mV, 17 pA.

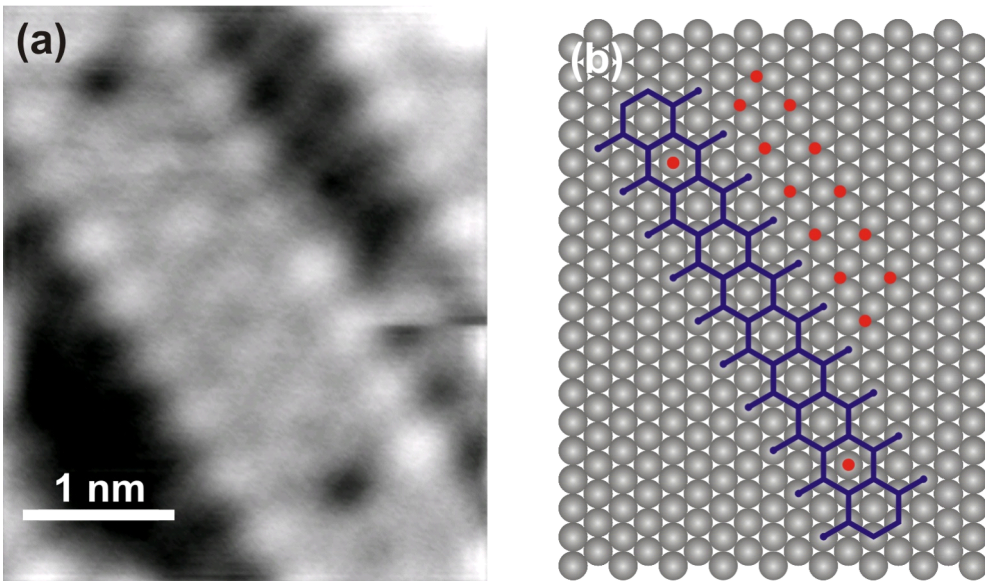

Figure 3.8: The center of the hexagonal unit cell of the partially dissociated water stripes show different contrasts. We suggest that the deep depressions correspond to a hydrogen adsorbed at an atop site in the center of the unit cell. Parameters: Heated to 132 K, -69 mV, 17 pA.

impurities was on the order of 3% of a monolayer. Hence, the hydrogen provided by the partial dissociation of water was interacting with the C to form CH. Fig. 3.9 shows a calculated STM image, similar to the geometry shown in Fig. 3.7 (c), however, this time with H in the center of every other hexagon. The experimental and the simulated image in Fig. 3.9 agree very well.

In conclusion, we have characterized the thermal evolution of water structures adsorbed on Ru(0001) in the temperature range between 110 and 145 K using low temperature scanning tunneling microscopy. The formation of mixed water-hydroxyl structures has been observed following partial dissociation above 130 K. The dissociation onset is strongly dependent on the annealing duration.

Water prefers to cluster in elongated linear structures at temperatures around 130 K to minimize the number of molecules bound with their plane nearly vertical to the surface. Both intact and partially dissociated water form linear structures that align 0° and 30° rotated relative to the Ru substrate, respectively.

We were able to resolve the liberated hydrogen following partial dissociation. Hydrogen adsorbs in the space between mixed water-hydroxyl clusters and forms a $(\sqrt{3}\mathrm{x}\sqrt{3})\mathrm{R}30°$ structure. DFT calculations in combination with STM images confirm the three-fold fcc site as the most stable adsorption site. Finally, we observed different imaging contrasts of the hexagonal centers of the elongated partially dissociated water structures, which suggests that a few centers are occupied with adsorbed hydrogen.

3.2 The second water layer

Hydrogen bonding, responsible for the unique properties and biological function of water, is not the only interaction between water molecules. Weaker electrostatic and

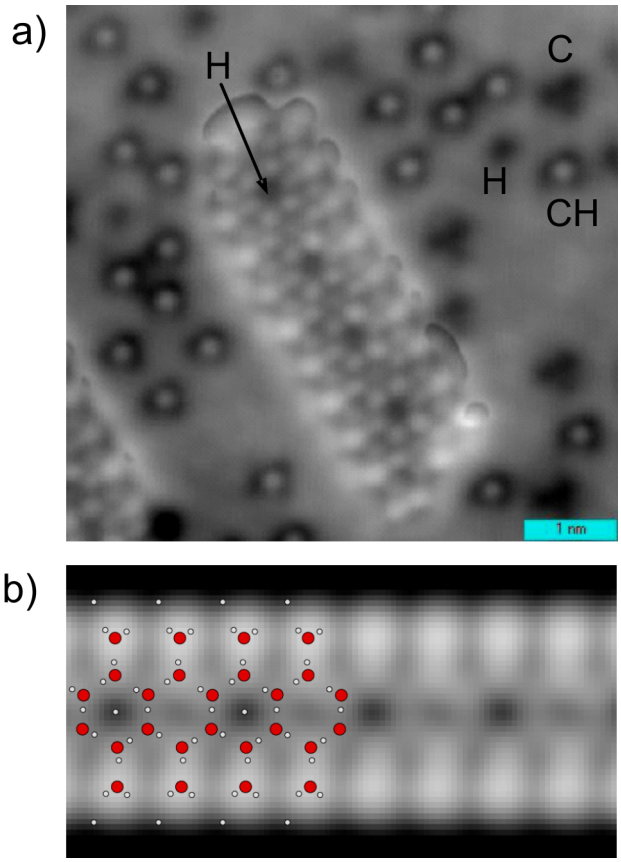

Figure 3.9: Experimental and simulated STM images of mixed H_2O-OH clusters formed by partial water dissociation. (a) The cluster reveals an internal ($\sqrt{3}$x$\sqrt{3}$)R30° structure. CH (sombrero shape) and smaller amounts of C (black triangles), as well as H (small black dots) are seen outside the cluster. At the center of the H_2O-OH hexagons, that appear darker, hydrogen is located. The surface was prepared by dosing water at 180 K, scan parameters 10 mV, 790 pA, see [Shi07]. (b) Calculated STM image with H in the center of every other hexagon.

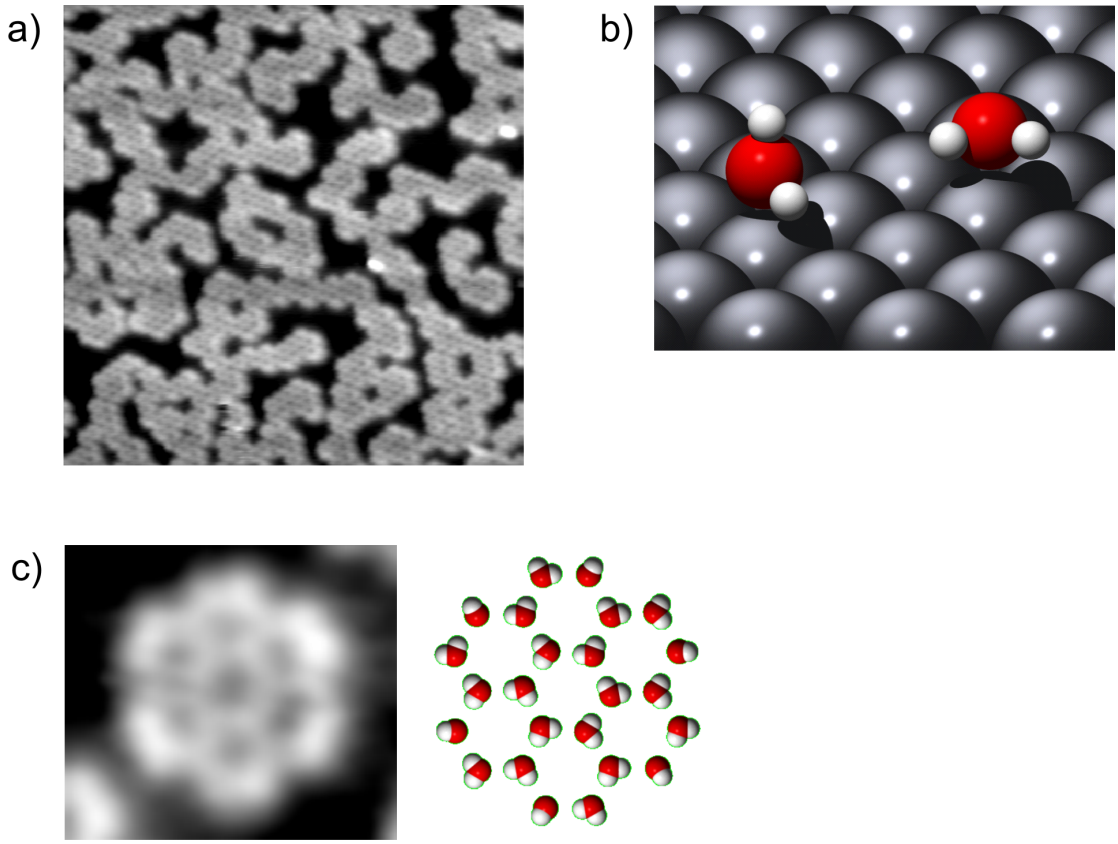

Figure 3.10: Structure of the first water layer. (a) STM image of D_2O adsorbed on Pd(111) at submonolayer coverage (20 x 20 nm^2, -115 mV, 97 pA). (b) Schematic illustration of water molecules with their plane nearly vertical to the surface, with one H pointing up into the vacuum (left) and flat-laying water with their plane nearly parallel to the surface (right). (c) The rosette structure is a building block of the extended pattern in (a). Here one of the hydrogen atoms of each water molecule on the rosette periphery lies below its oxygen atom. [Cer04].

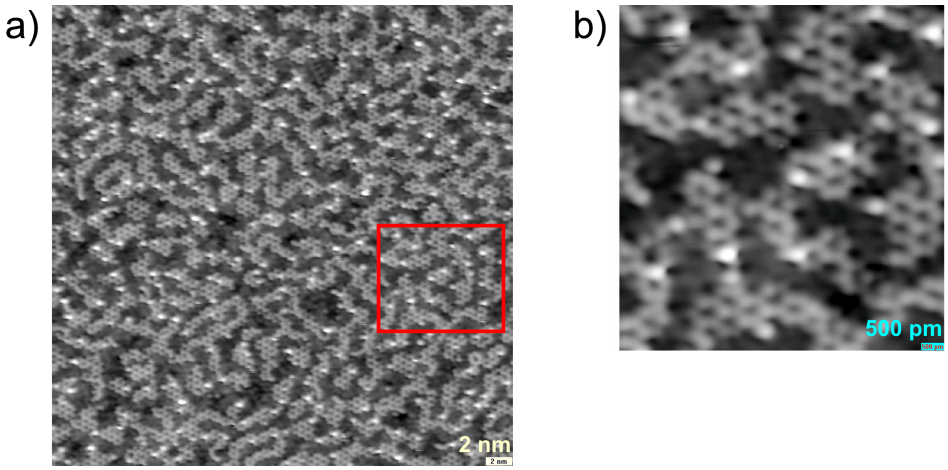

Figure 3.11: Second layer water growth on Ru(0001). (b) shows a zoom in (a), marked by the red square. The 2nd-layer hexamers are rotated 30° relative to the first layer and hence the Ru(0001) lattice. Image parameters: -38 mV, 57 pA.

van-der-Waals forces also play a role. Some of water's most important properties, like its liquid state at room temperature, owe much to a decrease in H-bonding, and to the effects of the weaker forces. The ideal laboratory for the study of non-H-bonding forces is a regime where ordered ice is not the dominant phase. Liquid water is an example; another is a water-solid interface, where H-bonding is significantly non-tetrahedral [Bal03]. Herein we show an indication for non-H bonding forces at interfaces: above a first molecular layer of water on the hexagonal surfaces of Pd and Ru, second-layer water clusters form – but not H-bonded to the layer below. The weak binding of the second-layer clusters is revealed by their quite unexpected geometries; they form hexagons rotated 30° relative to the first water layer, a local geometry not found in any low-pressure ($\lesssim$ 1 GPa) phase of ice [Pet99].

Previously, Pd(111) was imaged at 50 K in our research group using a separate instrument [Beh97]. The STM images of water layers on these surfaces show hexagonal arrangements of molecules bound to metal atoms and forming elongated honeycomb patterns, as in the example of Fig. 3.10, corresponding to Pd(111). The water molecules are nearly parallel to the surface and bind directly to metal atoms through their O atoms. They maximize H-bonding to neighboring molecules in single and double donor configurations. The geometrical constraints of H-bonding require incorporation of double acceptor molecules, which have their plane nearly vertical to the surface, with one H pointing down to the metal or up into the vacuum, see Fig. 3.16 (b). Minimizing the number of these vertical molecules, which lower the binding energy of the cluster [Cer04, Tat09] results in the peculiar, narrow stripe growth mode. Were the honeycomb structure to cover the surface completely, a saturation coverage of 2/3 monolayer would be recorded. Such a continuous layer would require 50% of the molecules to be vertical. We always observe growth of a second layer of water, before completion of the first.

Unlike Pd(111), adsorbed H_2O molecules on Ru(0001) can dissociate at temperatures somewhat below the desorption threshold, around 140 K [Sha08]. Dissociation is readily observed in STM images by the formation of "striped" islands with a characteristic contrast [Doe82, Tat08, Haq06, Hel95]. In this chapter we are concerned

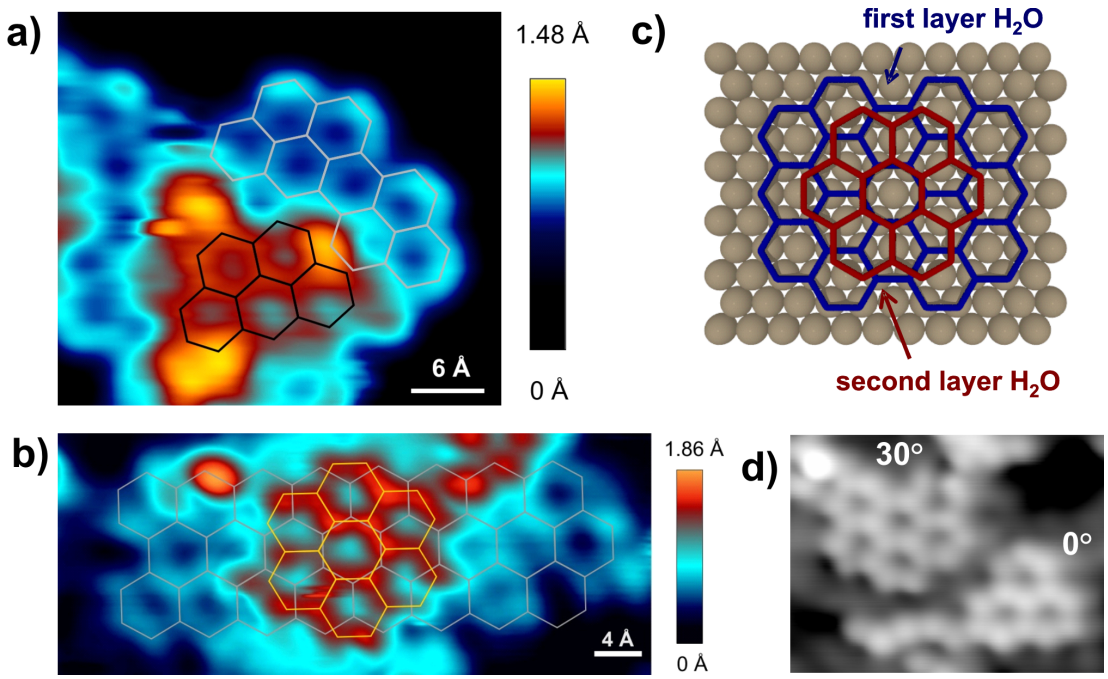

Figure 3.12: Rotation of 2nd-layer water hexamers on Ru(0001) and Pd(111). STM images of first and 30° rotated second layer water hexamers on (a) Pd(111) (156 pA, -124 mV) and (b) Ru(0001) (25 pA, -7 mV). (c) Schematic representation showing the orientation of the water hexamers in the first two adlayers. (d) One of the few exceptions on Ru(0001), where both orientations of second layer water hexamers were observed.

only with the growth and structure of water films below 130 K. Dissociation does not occur at any appreciable rate in this regime.

Images of the second layer formed by additional water show that, like the first, it forms hexagonal clusters, see Fig. 3.11 and 3.12. Surprisingly the hexagons in the second layer are rotated 30° with respect to those in the first. High-resolution images make clear that the honeycomb network of the first layer is contiguous and commensurate between the regions extending out from under the 2nd layer clusters, see Fig. 3.12 (b). The 30° rotation has been observed on both Ru, see Fig. 3.12(b), and on Pd, see Fig. 3.12(a), in 99.9% of all second layer hexagons. A few exceptions are observed occasionally, see Fig. 3.12(d).

The observation that the second water layer is rotated 30° relative to the first is unexpected because hydrogen bonding requires the 2nd layer hexagons to be in a 0° orientation relative to the first, see 3.13 (a). From an H-bonding point of view, a rotated 2nd layer leads either to an incommensurate structure (Fig. 3.13 (b) top) or – when assuming a contraction by 10 % – a commensurate structure (Fig. 3.13 (b) bottom). However, a contraction of 10 % is quite large and thus not very likely. There are two better ways to explain the observation of a 2nd layer rotated by 30°. One is that the molecules beneath the second layer restructure into a similar orientation, not visible in the images, see Fig. 3.13 (c). This, however, requires the rotated patch to connect to the surrounding molecules in the 1st layer by formation of 5- and 7-membered water rings, which was occasionally observed for the second

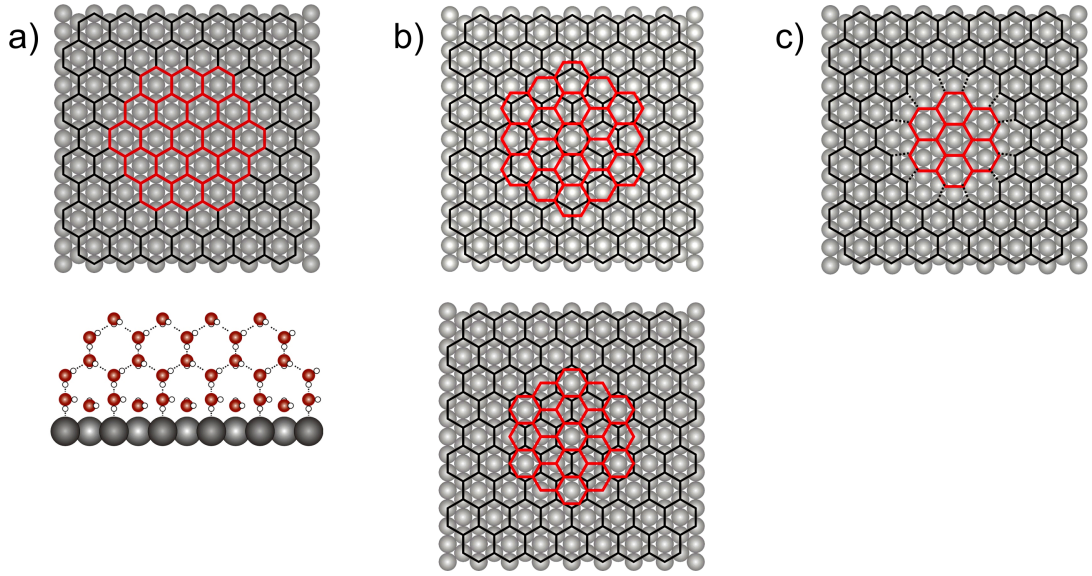

Figure 3.13: Different models for 2nd layer water growth. (a) Ice-like growth is not consistent with experiment. (b) From an H-bonding point of view, a rotated 2nd layer leads either to an incommensurate structure (top) or a commensurate, but not realistic structure, when assumimg a contraction by 10 % (bottom). (c) A rotation of both, first *and* second layer can be accomodated by defects in the form of pentagonal and heptagonal rings to reconnect with the surrounding first layer.

layer, see Fig. 3.14. Alternatively, one may postulate that the first layer has a hydrophobic character [Kim05], i.e., it forms no H-bonds to the second. The 2nd layer orientation should then be determined by the corrugation of the residual, and weak, interaction forces.

Interestingly, not even gain of thermal energy – that leads to partial dissociation of the underlying first water layer – is sufficient to rotate the second layer into registry with the first, see Fig. 3.4.

Quantitatively accurate calculation of such forces is beyond the capability of today's approximate versions of density functional theory (DFT) [San08, Hoh65]. Still, for a qualitative sense of whether weak forces dominate the binding of the second layer to the first, we are currently running DFT optimizations of hypothetical water adlayer structures.

In conclusion, our experiments suggest that water might form structures where clusters are bound together by non-H-bonding interactions. This occurs because the first water layer forms clusters bound to the metal by strong covalent bonds through the O atoms. The flat geometry of the molecules and their H-bonding with each other does not provide dangling H-bonds that would facilitate growth of a second layer following an ice-like structure. Therefore the second layer water molecules form hexagonal clusters with very weak bonding to the first layer, notably with a surprising 30° rotation relative to the first layer underneath not found in any phase of ice. Similar weak bonding configurations are likely in bulk water, where thermal agitation disrupts the tetrahedral structure. That is at the heart of room-temperature fluidity and, likely, many of the other unusual properties of water.

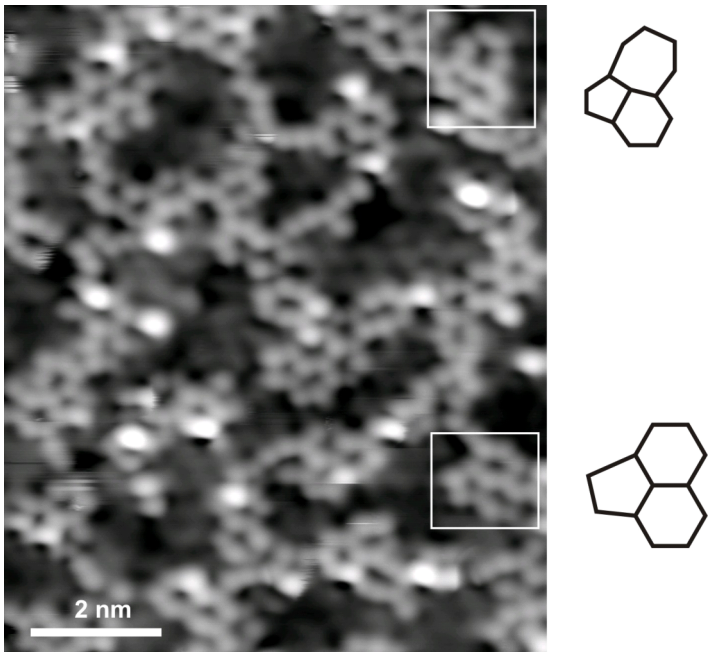

Figure 3.14: Defects in form of pentamers and heptamers as proposed in Fig. 3.13 (c). Dosed at 50 K and heated at 110 K, -11 mV, 86 pA.

3.2.1 Outlook: Beyond the second layer

Here we are going to report briefly on the water structure beyond the second layer which shows the transition from wetting layers to growth of compact ice clusters.

The structure of the water layers beyond the second layer that were adsorbed at 127 K, is reflected in Fig. 3.15. The dark background corresponds to the first layer of water and small patches of the ruthenium surface that are not covered by water. Apparently, even at this high coverage, the second layer is not complete; instead it consists of thin stripe-like clusters which seem connected to each other. On top of the second layer we observe several larger ice clusters, which are more compact compared to the first two wetting layers. The histogram in Fig. 3.15 (c) suggests that the height of these clusters is larger than just one additional layer. Remarkably, these clusters could be imaged in a stable manner by using small tunneling currents below 3 pA. Although the internal structure could not be resolved in detail, it seems that some ordering does exist, however, the exact structure remains unknown. Similar structures beyond the second layer were observed in a wide temperature range from 110-145 K.

The images in Fig. 3.15 show a clear transition in water growth beyond the second layer. The structure changes beyond two wetting layers to compact water clusters, several monolayers in height. This is in accordance to previous studies of D_2O multilayers on hexagonal metals where it was reported for temperatures above 120 K that the first monolayer of D_2O is hydrophobic and gives rise to nonwetting growth for subsequent 3D mounds [Kim05, Zim06, Meh07, Thü08, Thü08b]. A similar transition from amorphous layer-by-layer growth for D_2O adsorption at low temperature to crystalline growth at around 140 K was also found on Ru(0001) [Haq07, Kon06, Bov05]. So far, in the literature there has been reported *one*-monolayer thick wetting for heterogeneous growth of ice clusters. In contrast, we

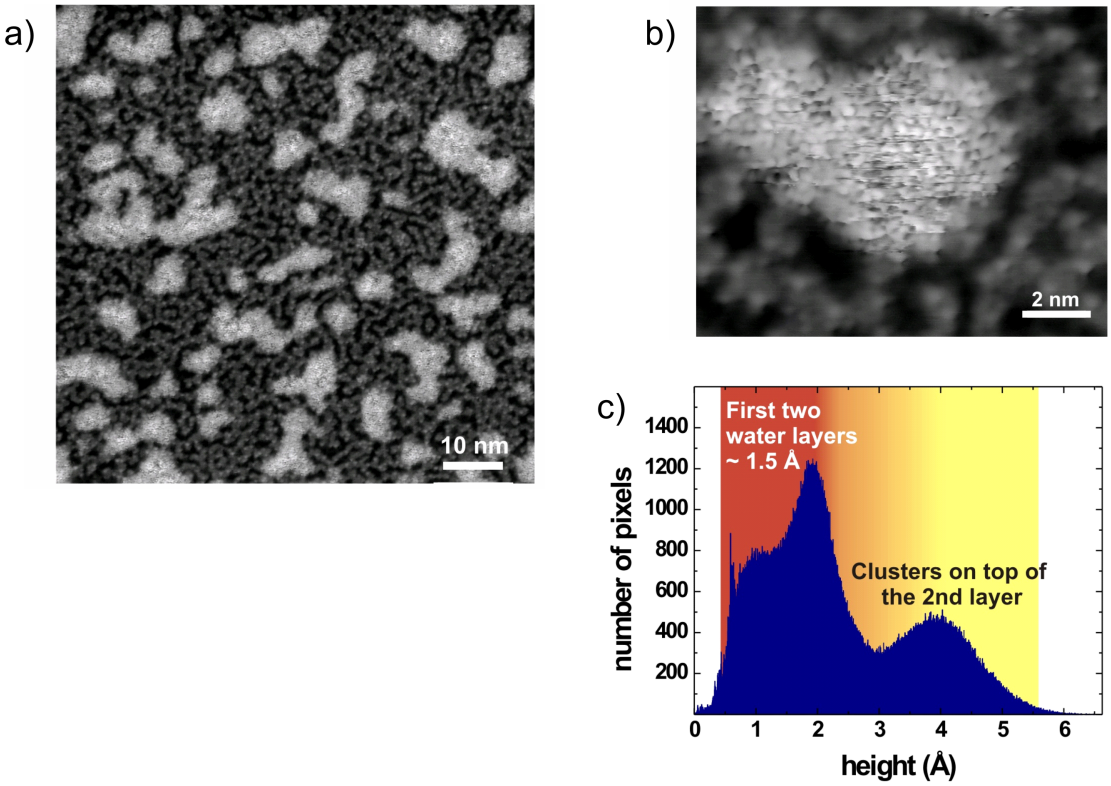

Figure 3.15: Water growth beyond the second layer on Ru(0001), adsorbed at 127 K. (a) Image showing two wetting layers with more compact clusters of several layers height on top, -123 mV, 2 pA, (b) cluster in more detail, -54 mV, 2 pA, (c) histogram of film thickness revealing that the clusters are several molecular layers high.

observe in our H_2O study a *two*-monolayer thick wetting layer.

3.3 Water induced surface reconstruction of the oxygen (2x1) covered Ru(0001)

Understanding water-solid interfaces is important in a variety of phenomena including catalysis, electrochemistry, and corrosion. It has also major applications in hydrogen production and fuel cells. Water adsorption on clean single crystalline metal surfaces was intensively investigated by various experimental techniques as a model system for understanding water-solid interfaces. In ambient conditions, metal surfaces interact with a vast number of molecules, amongst others oxygen and water. Thus most metal surfaces are covered by an oxide film and a water layer whose thickness depends on the relative humidity. Chemisorbed oxygen on metal surfaces forms well-ordered and atomically flat overlayers and are therefore ideal surfaces to study the initial interaction of water molecules with surface oxygen.

Co-adsorbed oxygen is known to change the dissociation behavior of water on Pt-group metal surfaces significantly. On Ru(0001) [Gla08, Gla05, Cab08, Mug08] and other Pt-group metals [Sha08] it was shown that the adsorption of water changes as a function of oxygen coverage. Dissociation is observed at low oxygen coverage

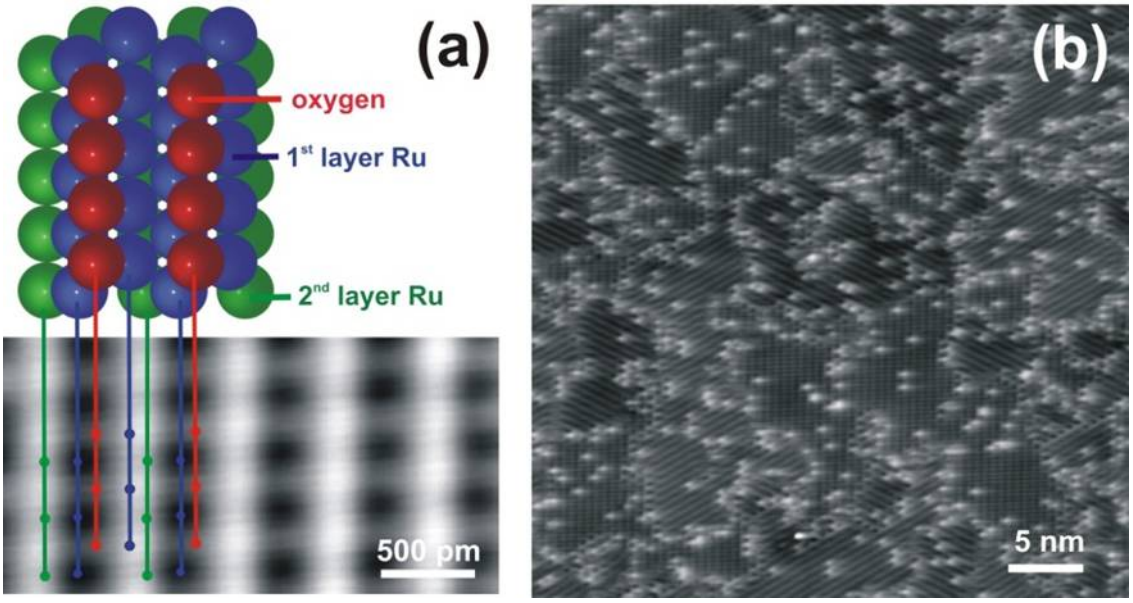

Figure 3.16: (a) Atomically resolved STM image (bottom) and schematic representation (top) of the O(2x1)/Ru(0001) surface. Red circles represent the oxygen atoms, blue and green represent first and second layer Ru atoms. (b) Large scan area image of the O(2x1)/Ru(0001) surface, showing different domains rotated 120° with respect to each other. White spots correspond to O vacancies. Imaging parameters: (a)-(b) 22 mV, 90 pA.

($\Theta < 0.2$ ML) while it is inhibited at larger O coverage ($\Theta = 0.25$-0.5 ML) contrary to studies that assume that water remains intact when interacting with oxygen [Doe82, Kre82, Thi87, Thi82]. Pre-adsorbed oxygen on the ruthenium surface does not only influence the dissociation characteristics of water but also its structure. On the p(2x2) oxygen terminated surface, water adsorbs in a p(2x2) symmetry [Mug08, Cab07], compared to a hexagonal arrangement ($\sqrt{3}$x$\sqrt{3}$)R30° observed on clean hexagonal closed-packed metal surfaces [Fei02, Cer04].

Unlike the open p(2x2)-O surface, the denser p(2x1)-O surface leaves much less room for the water to adsorb because all the preferred adsorption sites, i.e. atop sites, are blocked. Older results suggested that the high oxygen coverage on Ru(0001) [Doe82] as well as on Ni(111) [Mad82] and Rh(111) [Gib00] prevents any long-range ordering in the water overlayer. Recently, Gladys et al. performed an x-ray photoelectron spectroscopy (XPS) and near-edge x-ray absorption spectroscopy (NEXAFS) study of water adsorption on the O(2x1)/Ru(0001) surface [Gla08]. They reported that water adsorbs intact at 140 K and no indication of dissociation was observed at higher temperatures near the point of desorption. Although these measurements did not provide the local geometry of water on the p(2x1)-O surface, based on steric and symmetry arguments the authors proposed that water orders in a honeycomb structure, (2x2)-(2O-H2O), where half of the oxygen atoms from the O(2x1) overlayer shift from hcp sites to fcc sites, see Fig. 3.17 (b). Such a structure enables water to adsorb on the preferred metal top sites. The formation of a honeycomb O-structure has previously been observed in adsorption experiments of CO [Nar94, Kos92, Hof91] and NO [Sti99, Sti00, Jak97] on the p(2x1) oxygen

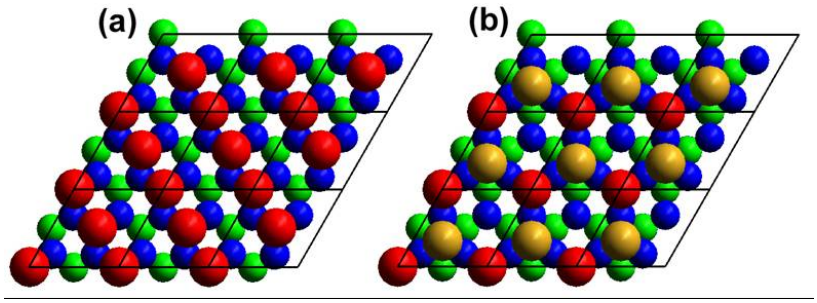

Figure 3.17: Structures formed by oxygen on Ru(0001) at half monolayer coverage. Two possible surface geometries are shown, along with the 2x2-cell (dark lines) used in the DFT calculations. Blue and green circles correspond to top and hcp Ru sites, respectively. Red circles correspond to oxygen adsorbed on hcp Ru sites and yellow circles to oxygen on fcc sites. (a) O(2x1) layer with all O atoms occupying hcp positions, and (b) O(2x2) honeycomb structure with half of the O atoms in hcp and half in fcc sites. Both systems were calculated and the O(2x1) structure found to be more stable by 231 meV per (2x2) cell.

covered ruthenium surface. The XPS experiments of Gladys et al. [Gla08] showed that between 170 K and 180 K most of the water desorbs intact from the surface and that the binding energy of the O 1s peak of the remaining water changed by 0.6 eV, indicating the formation of a second water species $H_2O(2)$. Recently, Shavorskiy et al. [Sha09] reported that the intact water species adsorbed on the O(2x1)/Rh(111) surface between 160 and 190 K have the same spectroscopic signature in XPS as the one observed for higher oxygen coverage on Ru(0001). Therefore, they assume that these adsorption states are in similar geometries on both surfaces. This indicates that the oxygen honeycomb structure, which has top sites available for the water molecules to adsorb, might not only form on oxygen precovered ruthenium but also on other metal surfaces as well as upon water adsorption.

So far, model calculations and direct experimental evidence for the formation of the oxygen honeycomb structure upon adsorption of water on the O(2x1)/Ru(0001) surface are missing. Here, we present a study of the adsorption of water on Ru(0001) precovered with 0.5 ML of oxygen, based on low temperature STM and DFT calculations by P. Cabrera-Sanfelix, D. Sánchez-Portal and Andrés Arnau at Donostia International Physics Center, San Sebastian (Spain). Our experiments and calculations confirm the formation of the honeycomb structure driven by the adsorption of water. We discuss the local geometry of water and oxygen in detail. In particular we found that the water molecules form a superstructure with (4x2) periodicity due to the alternation of two preferred molecular orientations.

3.3.1 The (2x1)O-Ru(0001) surface

Prior to water adsorption we identified the different high symmetry sites on the O-precovered surface that were later used to determine the water adsorption site. This is usually not trivial, since the imaging contrast of the oxygen precovered surface is strongly voltage dependent [Cab07, Cal04]. We found that our STM images compare well with previously published STM image calculations of the O(2x1)/Ru(0001)

surface [Cor05]. In Fig. 3.16 (a) the individual oxygen atoms of the (2x1) rows are resolved. The corresponding surface geometry is schematically represented in the same figure for comparison. The oxygen atoms appear as dark depressions relative to the ruthenium surface [Shi08]. A large scan image of the surface, Fig. 3.16 (b), shows that the surface consists of different domains rotated by 120° with respect to each other. Our surface preparation leads to an averaged domain size of approximately 50 nm^2 and a concentration of O defects less than 20%. The surface imaged in Fig. 3.16 (b) was slightly underdosed and the bright spots represent exposed Ru regions.

Figure 3.17 shows two possible high symmetry structures of the 0.5 ML oxygen precovered Ru(0001) surface. In Fig. 3.17 (a) the oxygen atoms sit on hcp sites arranged in a O(2x1) structure and in (b) the oxygen atoms form a (2x2) honeycomb structure occupying both hcp and fcc sites. Our calculations show that the O(hcp) pattern (Fig. 3.17 (a)) is the preferred configuration by ~231 meV per (2x2) cell, or per displaced O atom, compared to the honeycomb structure in Fig. 3.17 (b). This energy difference indicates the preference of O atoms to adsorb on hcp sites. This is consistent with our STM observations that always showed the well-ordered O(hcp) structure after the preparation procedure outlined below in the absence of water.

The calculations indicate also that in the O(2x1) overlayer (Fig. 3.17 (a)) the oxygen atoms adsorb 1.24 Å above the Ru topmost layer. There are four Ru top sites per unit cell (blue circles): two of them are bound to two O(hcp) atoms, the other two are bound to only one oxygen atom. The Ru atoms adjoining two O(hcp) are pulled 0.08 Å vertically towards the bound O atoms. This buckling of the first ruthenium layer, caused by the chemisorbed oxygen, as well as the oxygen-Ru distances are consistent with previous low energy electron diffraction (LEED) [Pfn89] and medium energy ion scattering (MEIS) experiments [Qui01] as well as DFT calculations [Cor05, Sta96]. In the O(2x2) honeycomb structure (Fig. 3.17 (b)) the O(hcp) atoms adsorb 1.22 Å over the Ru topmost layer, whereas this height increases to 1.46 Å for the O(fcc) atoms, i.e., 0.24 Å higher. In this honeycomb structure, three of the four Ru top atoms in the unit cell are bound to two oxygen atoms and so slightly pulled from the surface. The fourth Ru atom is not bound to any oxygen, leading to a small buckling of the surface of about 0.11 Å. As we will see below, this exposed top Ru atom creates the stable site for water adsorption.

Further calculations in a larger cell have been performed in order to determine the energy cost of the reconstruction as a function of the percentage of oxygen atoms displaced from hcp to fcc sites. Using a (4x4) unit cell, we found that the energy cost (ΔE) to move one (12.5 % of the oxygen atoms in the surface moved, ΔE = 185 meV per oxygen atom), two (25 %, ΔE = 191 meV/O), three (37.5 %, ΔE = 212 meV/O), and four (50 %; ΔE = 231 meV/O) oxygen atoms is roughly additive. Forming the honeycomb structure, i.e., displacing half of the oxygen atoms, costs $\sim$ 231 meV/oxygen. This value progressively decreases, up to a $\sim$ 20 %, as the percentage of displaced oxygen atoms is reduced.

3.3.2 Water monomers and small clusters

Figure 3.18 (a) shows a STM image of the O(2x1)/Ru(0001) surface with a few water molecules adsorbed at 140 K. The molecules appear as $\sim$ 160 pm protrusions above the 10-20 pm corrugation of the oxygen overlayer. The edges of isolated molecules are fuzzy in the images for bias voltages between 150 mV to 380 mV, for

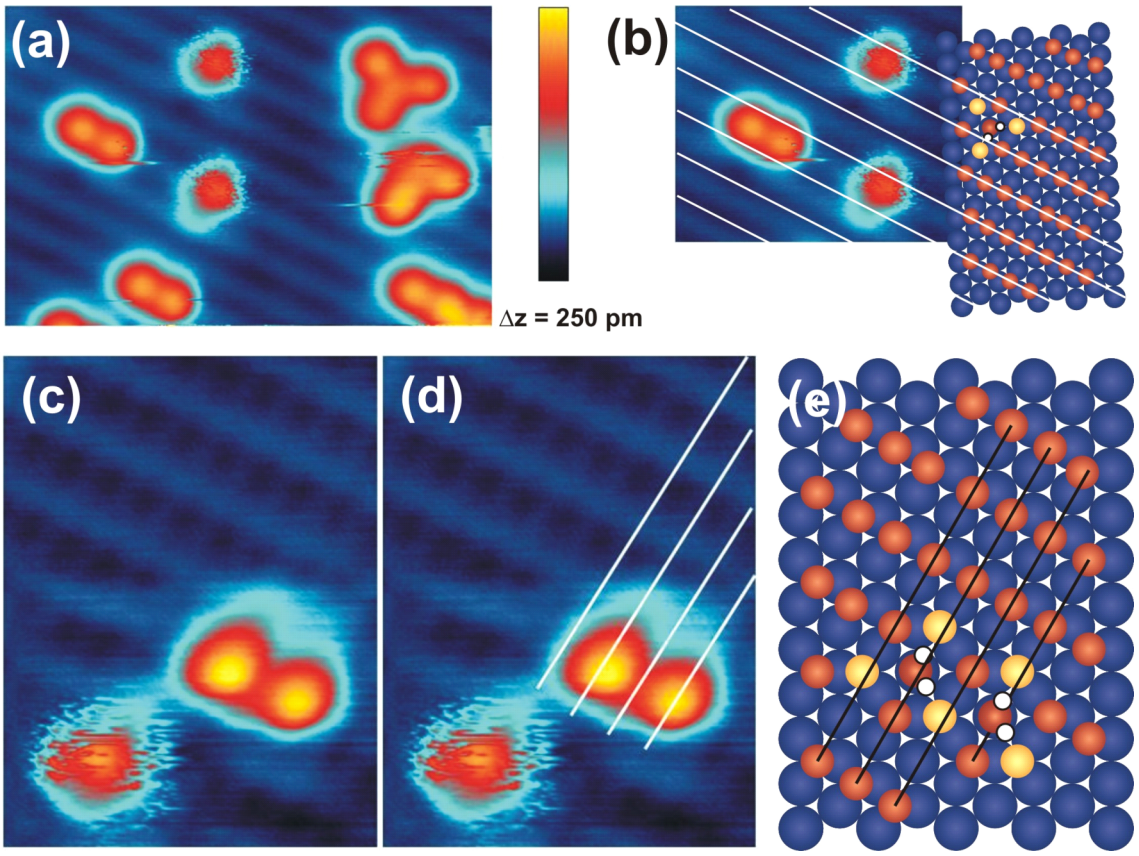

Figure 3.18: (a) STM image showing individual water molecules, and groups of two and three molecules in adjacent sites on a O(2x1)/Ru(0001) adsorbed at 140 K. During imaging at 7 K, clusters of neighboring molecules are stable, while isolated molecules are vibrating. (5.8 nm x 3.8 nm, -380 mV and 5 pA). The schematic in (b) shows that water molecules adsorb between the oxygen rows. The Ru atoms are represented in blue, oxygen on hcp sites in red and on fcc sites in yellow. (c)-(d) Images showing isolated water molecules and pairs of molecules on a well resolved image of the O(2x1)/Ru(0001) surface (2.9 nm x 4.7 nm, -245 mV, and 10 pA). The schematic drawing in (e) shows the location of the water molecules relative to the 2x1 oxygen lattice.

both positive and negative voltages. Such fuzziness is not observed in molecules occupying contiguous sites. Since at temperatures below 40 K there is insufficient thermal energy for the water to diffuse freely on the surface, we surmise that the monomer is vibrationally excited by tunneling electrons. Below 150 mV the libration modes (85 meV-115 meV), the frustrated rotation or the Ru-OH_2 stretch mode ($\sim$ 48 meV) can be excited by the tunneling electrons [Hen02]. In the case of molecules in neighboring sites these vibrations are inhibited due to the water-water interaction which stabilizes the relative orientation of the molecules. We will come back to this point of the preferred relative molecular orientations when considering the case of higher water coverage.

The image in Fig. 3.18 (b) reveals that water molecules adsorb between the oxygen rows (dark lines). Fig. 3.18 (c)-(d) provide additional information, since the (2x1) overlayer in the background is well resolved. These images show that the water

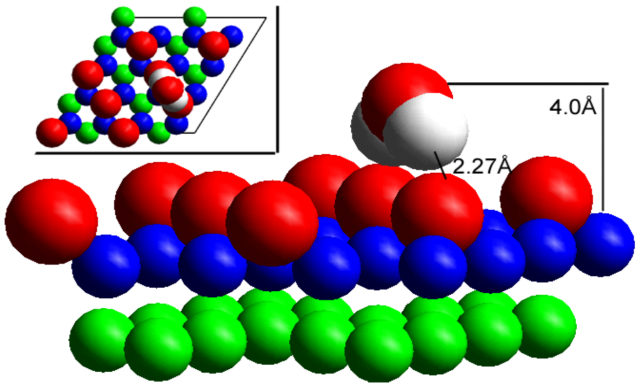

Figure 3.19: Optimized model of a hypothetical water molecule adsorbed on an unmodified O(2x1)/Ru(0001). Two quite long and weak hydrogen bonds are formed with the oxygen atoms in the surface. The calculated binding energy of 86 meV is insufficient to ensure wetting.

molecules adsorb on top sites and that neighboring molecules are separated by two lattice spaces (measured distance: 533 pm ± 10pm). Because the molecules adsorb on Ru top sites we conclude that the adsorption of one water molecule provides enough energy to reconstruct the underlying oxygen overlayer to create a free Ru top site.

These results are in contrast with another plausible adsorption configuration for water on O(2x1)/Ru(0001) that was proposed in Ref. [Thi05]. In this configuration, see Figure 3.19, the molecular plane is vertical and two hydrogen bonds (H-bonds) are established with two O atoms in the O(2x1) overlayer. Our calculations show that this configuration is weakly bound, with an adsorption energy of 89 meV per molecule. Water prefers to adsorb on Ru top sites if they are available and, as we will see in the following, in the case of the O(2x1)/Ru(0001) surface the water molecules are able to create such exposed top sites by displacing O atoms from their most stable adsorption site.

In order to explore different possibilities for the adsorption of water on the oxygen honeycomb reconstructed surface, we used several geometries where one, two, three, and four oxygen atoms were moved from hcp to fcc sites in a 4x4 unit cell. The water molecule adsorbs always on exposed Ru top sites, with its oxygen located 2.23 Å above the Ru atom and slightly displaced (~ 0.2 Å) in the xy-plane relative to the Ru top position in order to facilitate the formation of H-bonds with neighboring O atoms in the substrate. The molecule has two different orientations depending on whether the OH bonds point towards O(hcp) or O(fcc) sites. For the fully reconstructed oxygen-honeycomb structure the two possible orientations are shown in Fig. 3.20. In the configuration shown in Fig. 3.20 (a) two H-bonds are formed with neighboring O(hcp) atoms, whereas in the other orientation (b) the molecule is bound to the closest O(fcc) atoms. The H-bonds with O(fcc) atoms are ~ 30 meV stronger than those formed with O(hcp) atoms. They are also shorter, 2.30 Å compared to 2.46 Å. Therefore, configurations in which the hydrogen atoms of the molecule point towards O(fcc) atoms are ~ 60 meV more stable than those with an O(hcp) orientation. The adsorption energies for all the studied configurations are shown in Fig. 3.21. Notice that in all cases the adsorption energy on the reconstructed surface (in the range of 0.8-1 eV) is around ten times larger than on the original O(2x1)/Ru(0001)

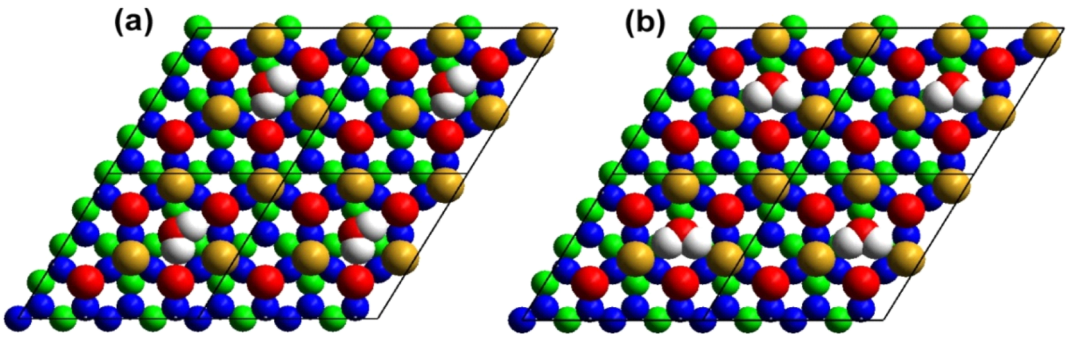

Figure 3.20: Models of water adsorption structures on the O(2x2)/Ru(0001) honeycomb surface. A 4x4 cell (marked by the lines) was used for the calculations. The coverage of water is 0.25 ML. Blue and green circles correspond to top and hcp Ru sites, respectively; red and yellow circles correspond to oxygen atoms at hcp and fcc sites. The difference between the two structures is the orientation of the water molecule: (a) H atoms point towards the O(hcp) atoms; (b) H atoms point towards the O(fcc) atoms. Adsorption energies are given in the last row of the table in Fig. 3.21. The O(fcc)-oriented molecules are $\sim$ 60 meV more stable.

surface (configuration shown in Fig. 3.19). Furthermore, the adsorption energy increases significantly (by more than 200 meV) as more oxygen atoms shift to fcc sites. Therefore, the energy released by the adsorption of a single water molecule compensates the energy cost to displace up to four oxygen atoms from hcp to fcc sites ($\sim$ 231 meV per oxygen atom). This clearly justifies the viability of the formation of the oxygen honeycomb structure after adsorption of water.

3.3.3 Water cluster formation

Water structures after annealing at 140K

Figure 3.22 shows STM images of the O-covered Ru(0001) surface after adsorption of different amounts of water, starting from around 10 % up to about 85 % coverage. The molecules form ordered domains on top of the O-covered substrate. These domains have higher contrast in STM images (bright in the figures) than the uncovered oxygen (2x1) areas. The formation of domains indicates that water-water interactions play a decisive role in the arrangement of the molecules. As the water coverage grows the water domains expand to cover most of the surface, shown in Fig. 3.22 (c), indicating that the first water layer wets the surface.

Figure 3.23 (a) shows an expanded view of an area inside an ordered water domain, with individual water molecules (brightest spots) resolved. The molecules form an hexagonal structure, in agreement with the model proposed by Gladys et al. [Gla08]. The image shows the different contrast of hcp and fcc oxygen atoms, the former appearing lower (darker) than the fcc ones. The same imaging contrast of fcc and hcp oxygen was observed in STM image simulations, see Fig. 3.26.

	E_{ads} (meV) [relative to the reconstructed O/Ru(0001)]	E'_{ads} (meV) [relative to the unreconstructed O_{hcp}(2x1)/Ru(0001)]
12.5% O shifted to fcc	788 (hcp)* **821 (fcc)***	603 (hcp)* 636 (fcc)*
25.0% O shifted to fcc	885 (hcp) **937 (fcc)**	503 (hcp) 555 (fcc)
37.5% O shifted to fcc	966 (hcp) **1023 (fcc)**	330 (hcp) 387 (fcc)
50.0% O shifted to fcc	977 (hcp) **1034 (fcc)**	53 (hcp) 110 (fcc)

* For the 12.5% configurations the hydrogen bonds are always formed with O(hcp) atoms. Here, fcc and hcp labels refer to the orientation of the plane bisecting the molecule. This plane passes through the closest O(fcc) atom for the so-called fcc configuration.

Figure 3.21: Adsorption energy (E_{ads}) of one water molecule on a partially reconstructed (4x4) supercell of the O(2x1)/Ru(0001) surface. As indicated in the first column, E_{ads} is given for different fractions of oxygen atoms displaced to fcc sites. The (hcp) and (fcc) labels correspond to different orientations of the water molecule with the hydrogen atoms oriented towards O_{hcp} or O_{fcc} atoms, respectively. E'_{ads} is the adsorption energy relative to the clean unreconstructed O_{hcp}(2x1)/Ru(0001).

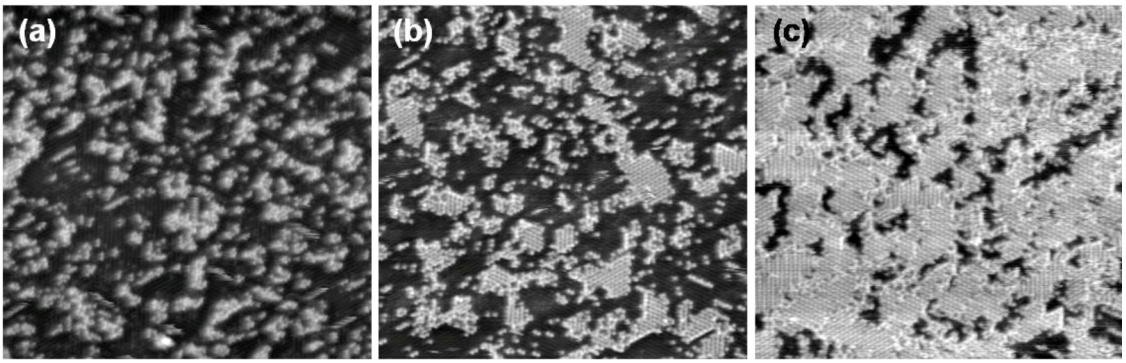

Figure 3.22: STM images of the O(2x1)/Ru(0001) surface with different amounts of water adsorbed at 140 K: (a) 10-20 % (b) 20-30 % and (c) 75-85 % water coverage. All images are 40 nm x 40 nm in size. STM image parameters: (a) -155 mV, 37 pA, (b) 221 mV, 8 pA, and (c) -385 mV, 4 pA.

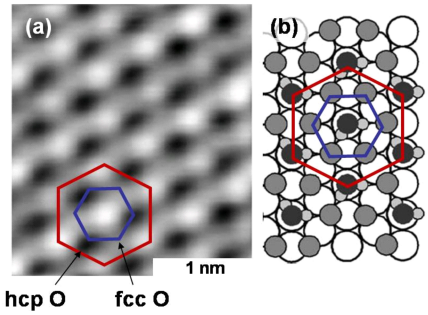

Figure 3.23: (a) High resolution STM image from a water domain revealing the hexagonal structure of the adsorbed water. (b) Model structure showing water adsorbed on the honeycomb (2x2)O/Ru(0001). STM image parameters: (a) 221 mV, 8 pA, (b) 221 mV, 7 pA.

Orientation of the water molecules within a cluster

In the following, we discuss the influence of the water-water interactions on the preferred orientation of the water molecules. For this study we performed calculations using supercells with sizes from 2x2 to 2x12 in units of the Ru(0001) unit cell. There are up to six possible orientations of a single water molecule in the oxygen honeycomb structure. Three of these orientations correspond to configurations in which the molecule is H-bonded to O(fcc) atoms, while the other three orientations have the water molecule bound to O(hcp) atoms.

We first consider a configuration (Fig. 3.24 (a)) where all water molecules have the same orientation. The binding energy of this structure is 62 meV/H_2O higher if the molecules are H-bonded to O(fcc) atoms than when they bond to O(hcp) atoms. This is agreement with the data in Fig. 3.21 (notice, however, that the data correspond to lower water coverage) and confirms the $\sim$ 30 meV additional stabilization for each O(fcc)-oriented H-bond respect to the O(hcp) ones. In the case of two different alternating orientations of the molecules, we have considered two configurations (Fig. 3.24 (b) and (c)) formed by O(fcc)-oriented molecules. The configuration in Fig. (b) is energetically degenerate with that in panel (a). However, the structure in (c), where the water dipoles make angles of 60° and face each other in pairs of rows, is $\sim$ 21 meV/H_2O less stable than the optimum dipole-parallel water rows in (a). The energy ordering of these structures can be fully understood from the interaction between the dipoles of the adsorbed molecules. Taking into account only the dipole-dipole interaction the structure in panel (a) is the most stable followed closely by (b). Structure (c) is higher in energy. More specifically, the difference between the dipole-dipole interaction energy of structures (a) and (c) is more than 6 times higher than the corresponding difference for configurations (a) and (b). Interestingly, a starting geometry similar to that in Fig. (b) but formed by O(hcp)-oriented molecules was not stable during optimization and spontaneously evolved to the configuration shown in (a). This confirms the strong preference of the water molecules in this substrate for the H-bonding to O(fcc) atoms.

We have also considered a configuration (Fig. 3.24 (d)) of O(fcc)-oriented molecules with three different relative orientations of water in successive rows. This structure is less stable (by $\sim$ 17meV/H_2O) than the optimal configurations in (a) and (b). Again, this is consistent with the energetics derived from dipole-dipole interactions.

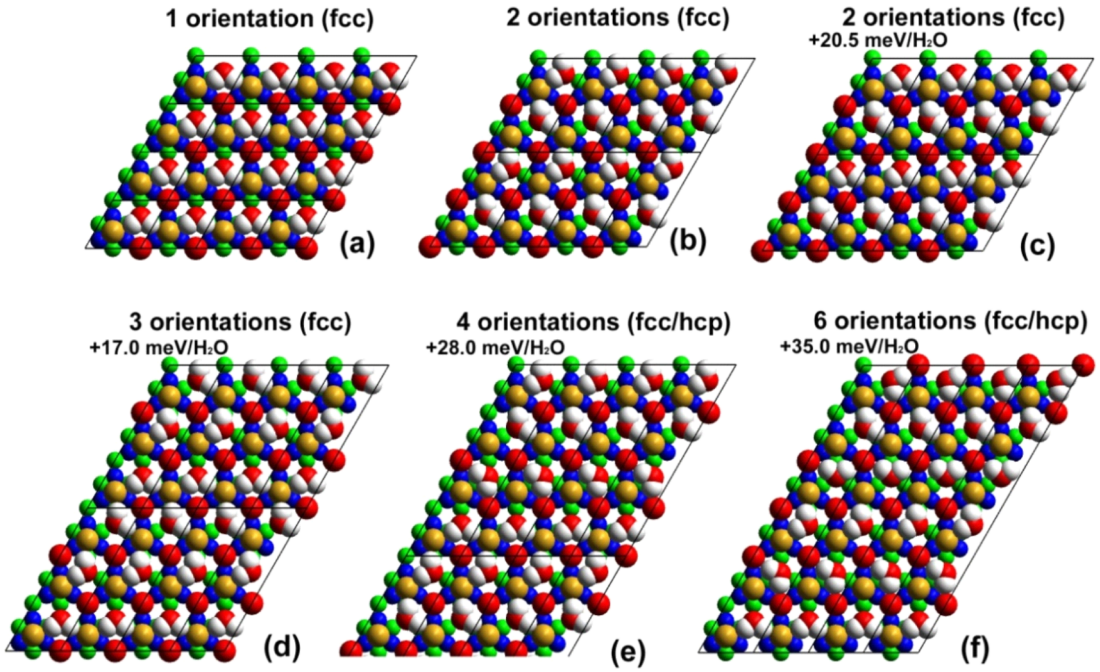

Figure 3.24: Overview of relaxed geometries from the DFT calculations for different relative orientations of the water molecules within the layer. Figures (a)-(d) correspond to different configurations in which all the molecules are H-bonded to O(fcc) atoms. In panel (e) one molecule out of four is H-bonded to two O(hcp) atoms, and in panel (f) 50% of the molecules are H-bonded to O(hcp) atoms. In (a) all water dipoles are aligned, while in (b) their directions alternate. These two configurations are the most stable and are energetically degenerated, with an adsorption energy E_{ads} = 896 meV/H_2O. The other configurations are slightly less stable with adsorption energies lower by 21 meV/H_2O for (c), 17 meV/H_2O for (d), 28 meV/H_2O for (e), and 35 meV/H_2O for (f).

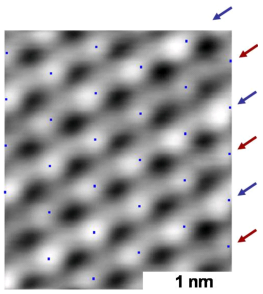

Figure 3.25: Experimental STM image showing the presence of slight deviations from the perfect 2x2 alignment in the position of the maxima corresponding to water molecules, represented by the blue lattice. Every second row is slightly displaced.

We can also consider more than three relative orientations among the water molecules, but then at least one molecule per cell has to be H-bonded to O(hcp) atoms. This will reduce the stability of these structures by $\sim$ 60meV per molecule. Hence, it should be energetically unfavorable to have more than three orientations within a cluster. This is confirmed by our calculations. As expected, the configuration with four different water orientations, with one imposed O(hcp)-oriented molecule out of four (see Fig. 3.24 (e)), is less stable by 28 meV/H_2O compared to the optimal configurations in (a) and (b). An alternative configuration with four different water orientations: 50 % O(hcp)/50 % O(fcc)-oriented molecules, is also less stable than the optimum ones by $\sim$ 30 meV/H_2O. Fig. 3.24 (f) shows a configuration with six relative water orientations, in which half of the molecules are O(hcp)-oriented. This configuration is 35 meV/H_2O higher in energy than the most stable ones.

In summary, the energy ordering of all the calculated structures can be explained as the result of dipolar intermolecular interaction with an energy penalty of 60 meV per O(hcp)-oriented molecule. Our calculations clearly show that the energy difference between O(fcc)-oriented and O(hcp)-oriented adsorption configurations of water in this substrate is larger than the energy differences associated with different relative orientations of the molecular dipoles. Therefore, at low temperatures we should only expect to find O(fcc)-oriented molecules in the oxygen honeycomb reconstructed surface.

Experimentally we find that in some domains the water molecules do not show the same contrast and that their position deviates slightly from the perfect 2x2 alignment, as shown by the lattice of blue points in Fig. 3.25. In the molecular rows marked by red arrows the dots are centered over the water molecules while in the rows marked with blue arrows they are slightly off-centered. This asymmetry is not present in the oxygen honeycomb structure obtained after desorbing the water above 185 K, which will be discussed later (Fig. 3.28). This observation suggests that the deviations from the perfect 2x2 structure are correlated with the orientation of the molecules. Simulated STM images corresponding to the three more stable configurations in Fig. 3.24 are presented in Fig. 3.26 (d)-(f). In the case of two and three relative water orientations, the STM simulations show that the center of the molecules is slightly displaced, similar to the shift observed in the experimental images. From this comparison we can conclude that two relative orientations of

water molecules are indeed present in the experimentally observed configuration which, therefore, form a (4x2) periodicity. This is supported by the fact that such molecular arrangement is calculated to be the most stable one, together with that in Fig. 3.24 (a). Curiously, the energetically equivalent structure, where all molecules are oriented in the same direction, has not been observed in the STM experiments. This indicates that, in reality, the structure with two alternating orientations and (4x2) periodicity is more stable than that with all molecules aligned. However, the reason behind this larger stability is still unclear.

3.3.4 Water structures formed after annealing above 180 K

Annealing a nearly fully water covered surface (as the one in Fig. 3.22 (c)) to 180 K caused most of the water to desorb. A small residue of molecules was left on the surface forming one-molecule wide lines, several nanometers long, as shown in Fig. 3.27. These water lines were homogenously distributed over the surface and have an apparent height of 55-65 pm over the oxygen covered ruthenium surface. The lines often start or end at an edge of underlying oxygen domains. The molecule at the junction of individual lines showed higher contrast than the rest of the water molecules, as shown in Fig. 3.27 (c). The lines did not decorate the steps nor grew over monatomic steps. Interestingly, the oxygen overlayer around the lines retained the honeycomb structure and did not change to the original O(2x1) structure. We will describe the characteristics of this honeycomb structure in further detail in the next section. In order to grow more of these water lines we dosed water while keeping the surface at 180 K. However, the coverage did not increase significantly. Annealing the sample to 185 K, even in the presence of background water, resulted in the complete desorption of the water layer and only the oxygen overlayer remained on the ruthenium surface, as shown Fig. 3.28 (a).

The water lines could well correspond to the $H_2O(2)$ species identified by Gladys et al. [Gla05] by XPS. The authors showed that most of the water desorbed from the surface between 170 K and 180 K, and the binding energy of O 1s peak of the remaining water changed by 0.6 eV, forming a second water species $H_2O(2)$, with a saturation coverage of 0.23 ML. We observed a slightly smaller coverage, which might be due to the difficulty of growing extended layers at these temperatures. They also concluded, using NEXAFS, that these water molecules are tilted with respect to the surface plane. At present, neither our STM experiments nor our simulations point in this direction. For water adsorbed on the O(2x2)/Ru(0001) surface, previous STM experiments in our group showed a tendency for the molecules to form short linear row structures at intermediate coverage, rather than denser two-dimensional patches [Cab07].

Manipulation experiments on individual water molecules using voltage pulses suggest that the molecules are not adsorbed at the domain boundaries between oxygen honeycomb domains, as shown in Fig. 3.29 (b). A possible explanation for the formation of water lines is that at 180 K the diffusion of water molecules competes with desorption allowing the water to arrange in thermodynamically favored structures. Thus, dipole-dipole interaction between the water molecules might cause the formation of linear water stripes.

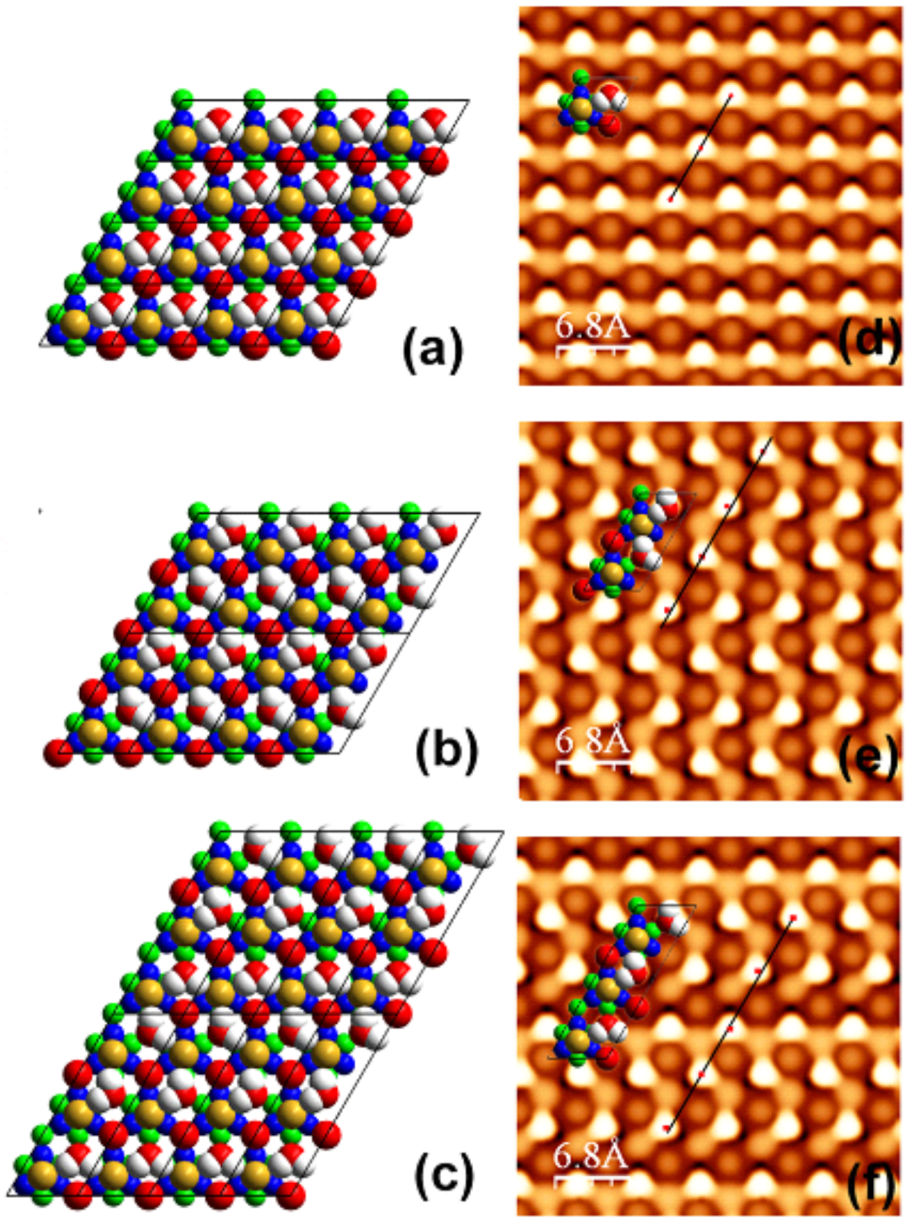

Figure 3.26: (a)-(c) Optimal configurations for the adsorption of water molecules on the oxygen-honeycomb reconstruction showing (a) one, (b) two, and (c) three different molecular orientations. Structures (a) and (b) are energetically degenerate, while (c) is slightly less optimal by ~ 17 meV/H_2O. In all configurations, the water molecules are slightly displaced (~ 0.2 Å) along the xy-plane, with respect to the Ru top sites, in order to form hydrogen bonds with the O(fcc) atoms (bond length 2.25 Å). (d)-(f) Corresponding simulated constant current images at +400 meV bias. In panels (e) and (f) the slightly displaced centers of the molecular protrusion are marked in red.

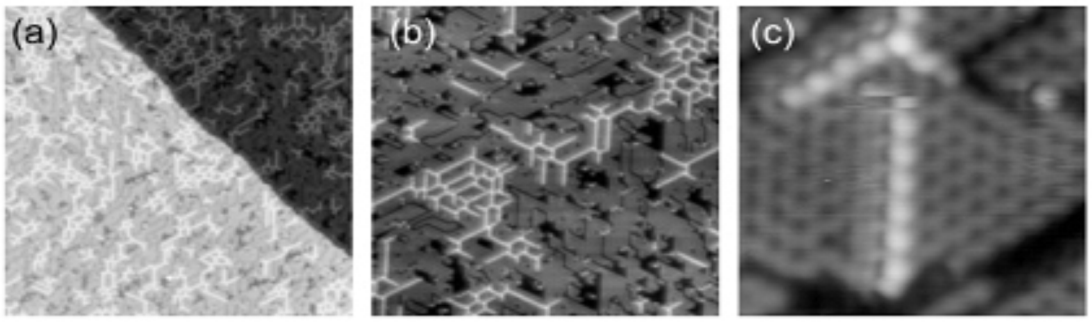

Figure 3.27: Water adsorbed at 140 K on the O/Ru(0001) surface followed by annealing to 180 K. The residual water molecules form lines several nanometers long. The lines do not grow over monatomic steps nor decorate them as seen in (a). Image parameters: (a) 80 nm^2, -340 mV, 9 pA, (b) 40 nm^2, -310 mV, 6 pA, and (c) 6.6 nm^2, -309 mV, 5 pA.

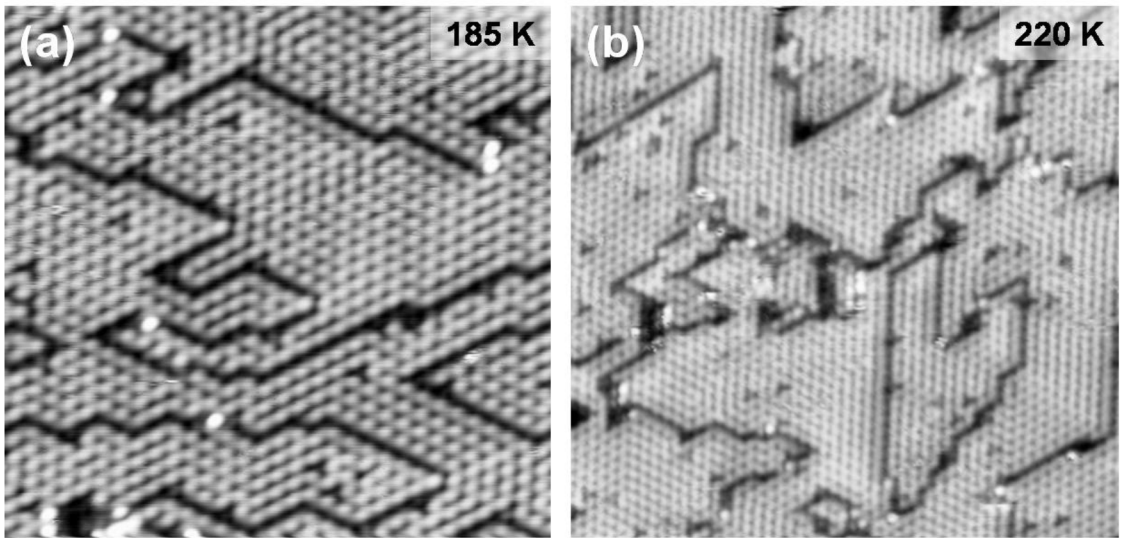

Figure 3.28: STM images of the oxygen honeycomb structure after desorbing the water by annealing to (a) 185 K (15 nm x 15 nm) and (b) to 220 K (25 nm x 25 nm). Image parameters: (a) -148 mV, 11 pA and (b) -312 mV, 26 pA.

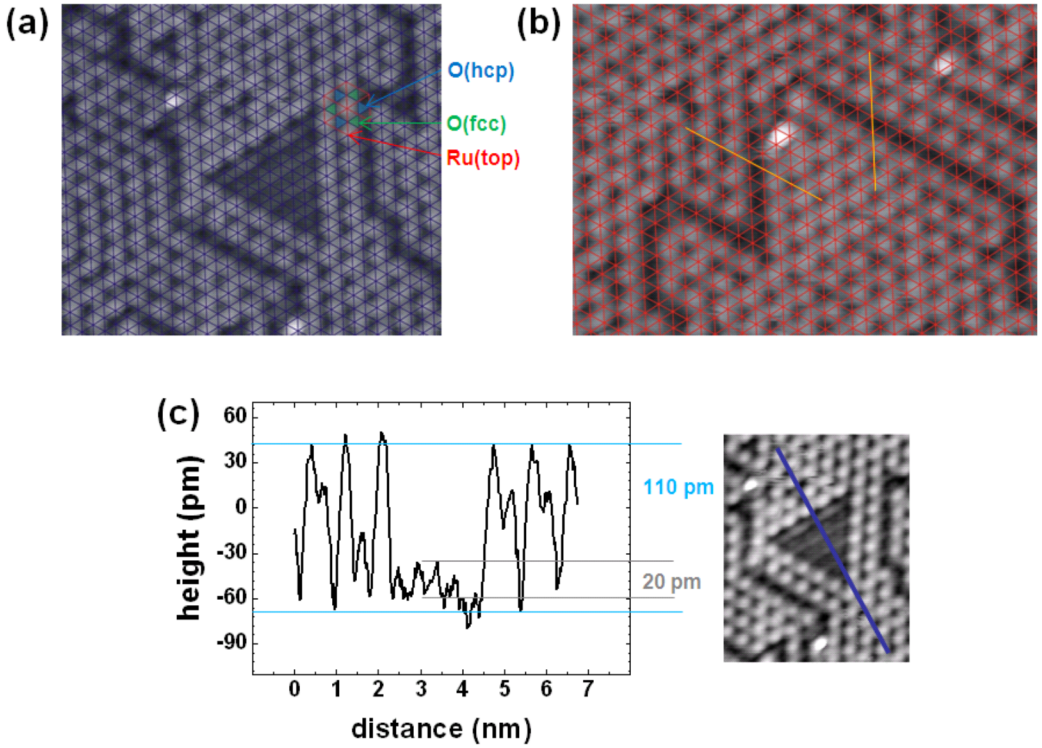

Figure 3.29: (a) High resolution image (9.2 nm x 6.8 nm) of the O honeycomb structure with a small patch of the original O(2x1) structure. The resolution of the images in the O(2x1) patch is sufficient for identification of the adsorption sites in the surrounding honeycomb structure. The nodes of the superimposed lattice located over the white protrusions in the honeycomb structure represent Ru(0001) top sites. (b) The dark stripes are domain boundaries between different honeycomb patches as can be seen more clearly with the help of the yellow lines. The nodes of the lattice in (b) represent Ru(0001) fcc sites. (9 nm x 5.2 nm) (c) Section through the O(2x1) patch and honeycomb structure in the right image, showing that the corrugation in the honeycomb structure is about five times higher than in the O(2x1) structure. According to the simulated STM images, the double peak structure might be attributed to the O(fcc) and Ru top atoms. STM parameters: -21 mV and 11 pA.

3.3.5 Honeycomb oxygen structure

The honeycomb oxygen structure created by water adsorption remained unchanged after heating to 220 K (Fig. 3.28 (b)). The original O(2x1) surface, consisting of three different domains rotated by 120° with respect to each other, could still be observed by STM after heating the surface to 260 K. Finally the oxygen switches back from the fcc sites to the hcp sites to restore the original O(2x1) at around 260 K. The formation of oxygen honeycomb structures starting from a p(2x1) oxygen covered ruthenium surface has also been observed with CO [Nar94, Kos92, Hof91] and NO [Sti99, Sti00, Jak97]. Regeneration of the O(2x1) structure by switching oxygen back from fcc sites to hcp sites was observed in conjunction with the desorption of CO and NO at 360 K for CO [Nar94, Kos92, Hof91] and 470 K for NO[Jak97]. Since desorption of these molecules occurs at a higher temperature than for water, it is not possible to prepare a pure oxygen honeycomb structure without them. In contrast, the oxygen honeycomb structure remains on the surface after the water desorption.

The interesting metastable oxygen honeycomb structure might be used as a template for the adsorption of other small molecules providing the unique feature of two kinds of oxygen species (fcc and hcp bound) compared to the other known oxygen reconstruction. Because the fcc oxygen is more weakly bound to the surface, it is also likely to be more reactive towards other coadsorbed molecules adsorbed at hcp sites.

The high resolution image in Fig. 3.29 (a) reveals dark patches between the honeycomb structures with the original O(2x1) structure. They correspond to residual areas not covered with water as in Fig. 3.22 (c). We used these O(2x1) patches as a reference to identify the adsorption sites in the honeycomb structure. The white protrusions correspond to Ru top sites, the core of the honeycomb structure. The narrow dark stripes between honeycomb structures show also a (2x1) structure, qualitatively with the same contrast as the (2x1) patches. These stripes are domain boundaries between different honeycomb patches as can be seen in Fig. 3.29 (b). The high resolution images of the oxygen honeycomb structure in Fig. 3.28 and Fig. 3.29 show no evidence for water dissociation, only a few defects/adsorbates are observed after water desorption. This is in agreement with Gladys et al. [Gla08, Gla05] who reported water dissociation is suppressed on the O(2x1)/Ru(0001) surface as indicated by the absence of a OH peak in XPS.

We observed a significant larger corrugation, by about a factor of five, in the images of the honeycomb structure compared to that in the O(2x1). The corrugation of the O(2x1) is between 10-20 pm while the corrugation of the honeycomb structure can be up to around 100 pm, see Fig. 3.29 (c). Large corrugations reflect a larger difference in the local density of states between O sites and Ru sites in the honeycomb structure. The corrugation of the O(2x1) structure is in agreement with previous experiments and calculations [Cor05], which described that the (2x1) structure has about a factor three weaker corrugation in STM images than the (2x2). Our simulation of an STM image of the oxygen honeycomb reconstruction is shown in Fig. 3.30. The simulated image reveals a corrugation of about 75 pm, confirming that the corrugation is large compared to that of the O(2x1) and O(2x2) structure.

In conclusion, STM experiments have shown that water adsorbs on the O(2x1)/Ru(0001) surface forming a well-ordered (4x2) superstructure at temperatures of 140 K. This requires displacement of half of the surface oxygen from a hcp to an fcc

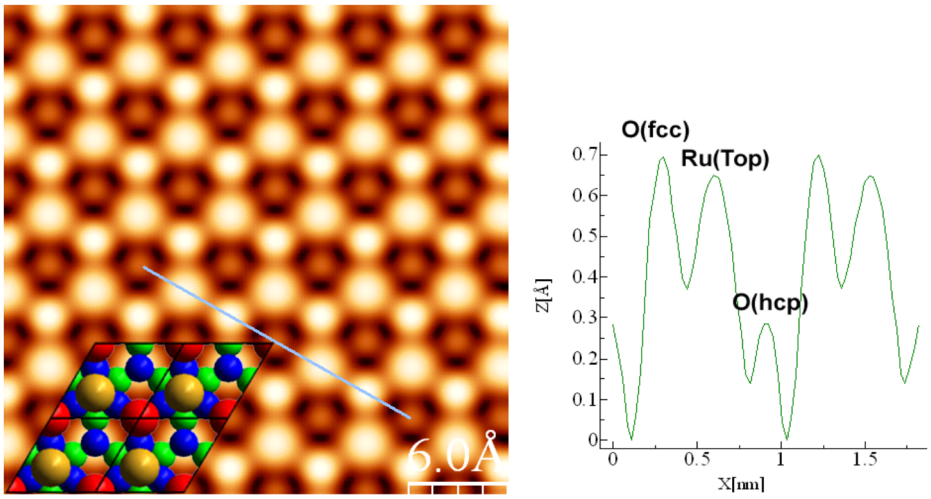

Figure 3.30: Calculated constant current STM image at +400 meV bias, and topographic profile for the oxygen honeycomb reconstruction. Inset: red circles correspond to O(hcp) atoms, while yellow circles correspond to O(fcc) atoms. Blue and green circles correspond to top and hcp Ru sites, respectively.

site to form a honeycomb structure that provides Ru top sites for the adsorption of water. DFT calculations have determined that binding of the water molecules to the unmodified O(2x1)/Ru(0001) structure is too weak to lead to wetting. Instead a reconstruction of the O(2x1) into a honeycomb O(2x2) structure takes place that is driven by water adsorption. The energy cost of $\sim$ 231 meV/oxygen atom for this reconstruction is well compensated by the adsorption of water on the exposed Ru atoms. At low coverage, water adsorbs strongly on top of the Ru atoms with its plane nearly parallel to the surface and with the hydrogen atoms oriented towards the oxygen atoms at the fcc-hollow sites. At low water coverage (0.625 ML) the adsorption energy can be as high as $E_{ads} \sim 1.03$ eV/H_2O, high enough to overcome the energy cost of moving four oxygen atoms from hcp to fcc sites in a 4x4 unit cell. At the saturation water coverage of 0.25 ML, we found two energetically degenerate configurations with $E_{ads} = 896$ meV/H_2O. These structures differ in the relative orientation of the water molecules: in one configuration all molecules are aligned, while in the other the molecules alternate their orientations forming a (4x2) periodicity. Simulated STM images of these configurations show that the water molecules are slightly displaced ($\sim$ 0.2Å) with respect to their Ru adsorption sites, towards the O(fcc) atoms with which they form H-bonds. The STM images showed slight deviations in the position of the water molecules from a perfect 2x2 alignment, distorting it into a (4x2) periodicity, with two orientations of water molecules.

At 180 K, most of the water desorbed from the surface and the remaining water arranged in linear structures. Water was completely desorbed above 185 K, leaving behind a metastable oxygen honeycomb structure. The stable (2x1) structure is not recovered until after heating to temperatures close to 260 K.

Theoretical method

DFT calculations were performed in order to determine the preferred configuration of the adsorbed water layer and on the related oxygen honeycomb reconstruction. We have also investigated the energetics of the reconstruction process with and without water. The calculations were done using the Vienna package (VASP) [Kre93, Kre94, Kre96b], within the Perdew-Wang 1991 (PW91) version of the general gradient approximation (GGA) [Per92]. The projector augmented wave (PAW) [Blö94, Kre99] method was used to describe the interaction of valence electrons with the Ru, O and H cores. A symmetric slab of seven Ru layers and the same amount of vacuum was used to represent the Ru(0001) surface. The oxygen and water adsorbates are placed on the top and bottom surfaces of the symmetric slab. A plane-wave cutoff of 400 eV and a 6x6x1 k-point sampling was used for the smallest cell, corresponding to a 2x2 unit cell of the clean Ru(0001) surface. For supercells of different sizes we used a similar k-sampling density. All geometries were optimized by allowing relaxation of all degrees of freedom of the two outermost Ru layers and the O and H atoms until residual forces were smaller than 0.03 eV/Å. STM simulations based on the structures obtained by DFT were performed using the Tersoff-Hamann [Ter83, Ter85] approximation, assuming constant current and a bias voltage of +400.0 meV.

3.4 Graphene on ruthenium

Since its successful fabrication by cleavage in 2004 [Nov04], graphene has attracted great interest because of its novel properties and potential applications. As the epitaxial growth of graphene on a metallic substrate is a promising way to produce large-scale graphene layers with high quality [Pan08], the structure and growth of graphene on ruthenium has recently been studied in detail.

In the following chapter, we report a novel growth mode for graphene, observed on a Ru(0001) surface. This growth originates from Ru metal etching, leading to a peculiar reconstructed Ru surface of a comparably huge unit cell. Afterwards, we show how water interacts with this graphene covered ruthenium surface.

3.4.1 Graphene growth by metal etching

The study of graphene on metal surfaces has a long history, culminating in widespread recent activity [Win09]. Here we focus on the interaction of graphene with atomic steps and terraces on a precious metal surface. How graphene grows depends on the nature of this interaction. For example, on Ir(111) [N'Di08, Cor09, Log09, Log09b] and Ru(0001) [Log09b, Mar07, Log08, McC09, Sut08], it mainly grows over atomic substrate steps forming a continuous carpet. On Ru(0001) this growth mode [Log08, Sut08] occurs by adding carbon to the free edge of the graphene sheet, e.g., point A in Fig. 3.31(b). (On Ir(111) the graphene also grows slowly up the staircase of substrate steps [Cor09, Log09b].) Carbon from a sea of carbon monomers (adatoms) attaches to this free edge. Previous work suggests that the attachment occurs by an intermediate state involving several C atoms [Log09b, Log08]. Because of the high energy cost of forming these C clusters, carpet growth occurs only at high C supersaturation.

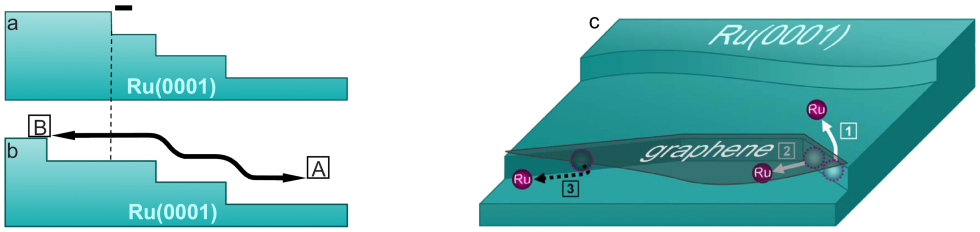

Figure 3.31: Schematic illustration of graphene growth on a precious-metal surface. (a) A graphene sheet (black) nucleated at a monatomic substrate step, on the lower terrace. In the carpet growth mode, the graphene sheet advances over descending substrate steps by adding carbon to the sheet's free edge, labeled A. (b) In the etching growth mode, the sheet grows in the opposite direction by etching substrate atoms, causing the substrate step that abuts the graphene sheet (point B) to retract. (c) Representation of possible paths for etched Ru atoms during "uphill" growth of graphene on Ru(0001): (1) to the upper terrace, (2) under graphene sheet, and (3) on the same terrace away from graphene.

The difficulty of attaching individual carbon adatoms to the free graphene edge has another consequence – growth can occur by an additional complex mechanism, as illustrated in Fig. 3.31(b). Here the graphene sheet edge that abuts the substrate step edge (point B in Fig. 3.31(b)) advances by displacing atoms from the monatomic step of the substrate. The graphene sheet thus "eats into" the adjoining terrace.

Evidence for graphene sheets embedded in terraces has been reported for graphene growth on Pt(111) [Nak02, Fuj05, Lan92], Pd(111) [Kwo09], and Ir(111) [Cor09], but the mechanism by which the embedding occurs has not been determined. In contrast to previous work, the results presented here show that carpet growth and etching processes occur on Ru(0001). Our focus is on the latter process.

We applied Low-energy electron microscopy (LEEM), density functional calculations and scanning tunneling microscopy to study a new mode of graphene growth on Ru(0001) in which Ru atoms are etched from a step edge and injected or *intercalated* under a growing graphene sheet. The intercalation alters the structure at the metal substrate/graphene interface and may change the properties of the film, e.g., its chemical reactivity.

LEEM experiments were conducted by E. Loginova and K. F. McCarty at Sandia National Laboratories (Livermore, CA). Since there is not enough room in this thesis to present these findings in detail, I refer to our publication for further reading [Log09c], and summarize the results in a nutshell: Graphene sheets that grow into Ru steps displace Ru atoms. The displaced Ru atoms can be captured by adjacent bare Ru steps, after diffusing over the upper Ru terrace (pathway 1 in Fig. 3.31 (c)), or they can be injected under the growing graphene (pathway 2 in Fig. 3.31 (c)). Our results suggest that the extent of injection can be as large as 10 to 20 % of a monolayer. The observation that pits several microns across expand during etching growth and shrink with graphene removal suggests that the injected Ru atoms can diffuse far from their source/sink, the Ru step edge.

A plausible way to account for the observed etching, according to DFT (performed

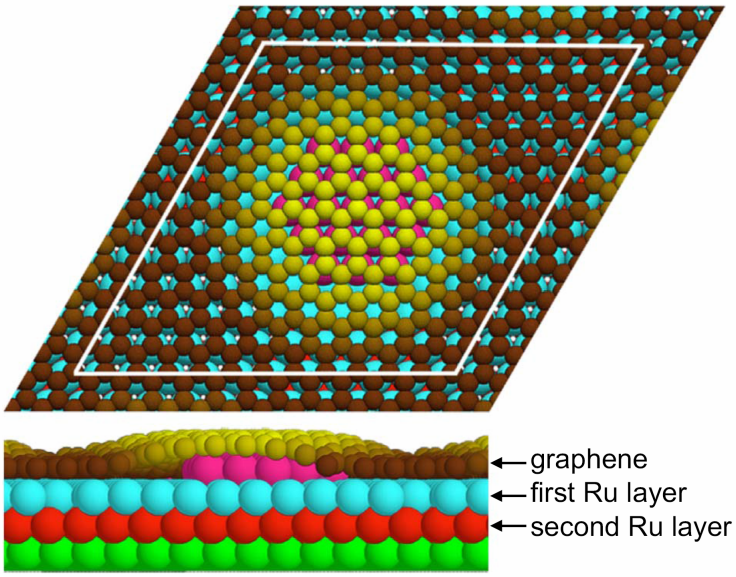

Figure 3.32: Schematic (top and side view) of a 19 Ru island under the "atop" region" of a graphene moiré on Ru(0001). White lines delimit the moiré supercell. Island Ru adatoms are colored magenta. First- and second-layer Ru atoms are colored cyan and red, respectively, enabling one to see that the hcp region of the moiré is to the right of the island, and the fcc region is to the left. C atoms are colored yellow to brown according to their computed heights above the Ru surface layer.

by P. J. Feibelman at Sandia National Laboratories (Albuquerque, NM)), is formation of small Ru islands. On Ru(0001), graphene makes a moiré with the substrate and is periodically buckled [Mar07]. As we describe next, Ru islands form with low energy under the moiré regions where the separation between the graphene sheet and the substrate is the largest. There are two reasons that support this scenario. One is that with a 2.14 Å natural spacing of Ru(0001) layers, and the sum of the Ru metallic radius and the C covalent radius equal to 2.10 Å, buckling of the graphene layer to a calculated interlayer separation of 3.79 Å comes close to providing sufficient room for intercalated Ru atoms with no strain. The other reason is that the high point of the moiré occurs in its "atop region," where C atoms reside, approximately, above 3-fold hollows of the underlying Ru surface (and, surround atop sites – whence the nomenclature). This means that an under-graphene Ru atom in an hcp hollow will lie directly under a C-atom. Thus, these Ru atoms are well-positioned to interact with the C 2pz orbital, just as the surface layer Ru atoms do with the C atoms directly above them in the low-lying regions of the moiré.

To test this idea we optimized islands of several sizes, producing a set of formation energies and chemical potentials. In each case, the atoms forming the Ru island were placed in hcp hollow sites, and the island, as a whole, was centered in the moiré atop region. An illustration of a moiré supercell containing a 19 Ru-adatom underlayer island is shown in Fig. 3.32, see [Log09c] for details .

Why have intercalated islands not been detected so far with STM or X-Ray diffraction [Mar08, Win09]? We discuss two relevant issues, first, how prevalent intercalated Ru islands would be on a typical Ru surface, and second, how inter-

calated islands might affect STM images, particularly the corrugation in apparent height. We begin by noting that DFT predicts that the under-graphene islands are metastable compared to Ru attached to steps. Ultimately they will decay and their Ru content will end up at non-abutted step edges. Thus, this decay must be kinetically hindered to detect the under-graphene islands. We have not been successful in finding such sites in our STM studies, a reflection of the technique's difficulty in imaging large areas. Overall, under-graphene islands would only be expected at the rare locations where a graphene sheet abuts a Ru step separating relatively wide terraces. However, the current lack of direct observation of the under-graphene islands does not rule out their potential to serve as a low-energy intermediate state that allows graphene to etch Ru.

So, how should the under-graphene islands affect STM? In principle, atomically resolved STM could see the effect of the under-graphene islands – the islands convert atop sites of the non-intercalated moiré to hcp-like sites. Since resolving these subtle differences in STM is likely challenging, we next discuss the effect of the intercalated islands on STM height corrugation. Testing the hypothesis of intercalated Ru islands by examining the height corrugation of graphene in STM is difficult: DFT shows that the height difference between highest and lowest C atoms without intercalated Ru islands is 1.55 Å. With a 19-Ru island, the height difference is 2.18 Å. With a 37-Ru island, the corrugation is not very different, 2.22 Å. With a 7-Ru island, it is 2.07 Å. The lack of striking differences in corrugations between all these predicted moirés and the observed experimental moiré (with about 1 Å corrugation [Win09]) does not allow a definitive determination of the existence of underlayer islands, given the uncertainty of the relative importance of electronic and topology effects in determining the STM corrugation.

Thus, DFT calculations suggest that under-graphene islands are a low-energy state that can accommodate large amounts of intercalated Ru. While the islands ultimately are metastable, they are an intermediate state that enables graphene to etch Ru steps by injecting Ru under graphene. Our LEEM observations of Ru etching and release are consistent with the proposal, but experimental confirmation awaits.

The STM observations in Fig. 3.33 suggest another state of the intercalated Ru besides formation of islands. The graphene structures shown in the images are rotated with respect to the Ru substrate and the moiré periodicity is 1.4 ± 0.2 nm, smaller than the ∼ 3 nm periodicity previously reported for the (12x12)C/(11x11)Ru [Mar07, Log08, Dai97, Wan08, Wu94, Zha09] and the (25x25) [Mar08] moiré superstructures. Distances in the STM images have been calibrated using the lattice spacing of bulk graphene (2.46 Å) as a reference. The angle between the moiré periodicity and the carbon lattice is 9 ± 2° in Fig. 3.33 (a, c, d). Small rotations of the graphene lattice relative to the substrate lattice can cause large changes in the moiré periodicity [Cor08]. Based on the moiré equations derived by Nishijima et al. [Nis64] we determined a rotation of the graphene relative to the ruthenium lattice of about 6° using a Ru-Ru distance of 2.71 Å.

Strikingly, we also observe a long-range triangular network with unusually large unit cells (side lengths 8.7 nm (Fig. 3.33 (c)), 10.2 nm (Fig. 3.33 (d)) and up to 12.8 nm in Fig. 3.33 (b)). It is difficult to understand how this triangular network can result from placing graphene on a bulk-terminated Ru(0001) substrate. Instead, as we argue below, these triangles are consistent with a network of misfit dislocations

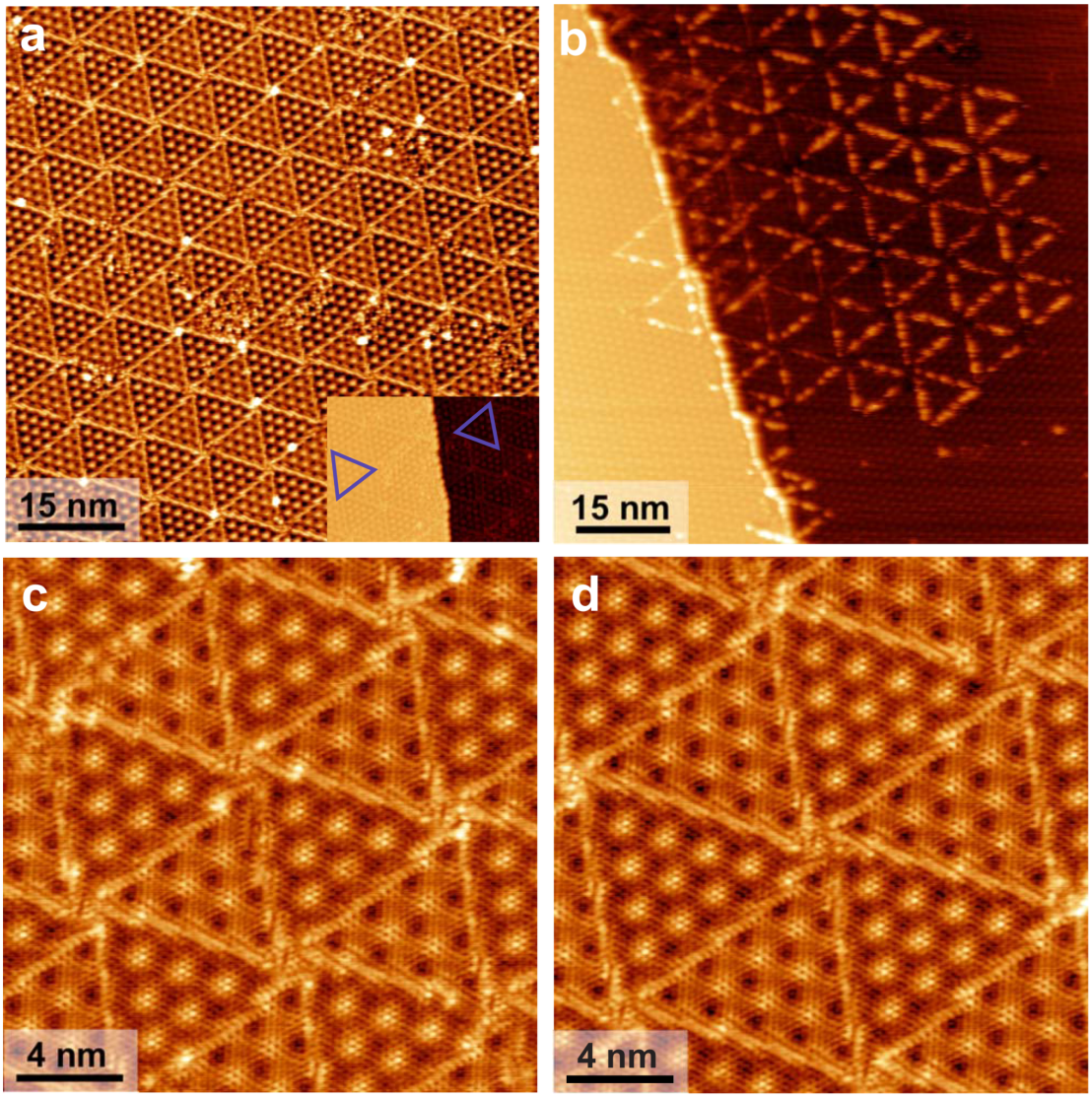

Figure 3.33: STM images of graphene grown by segregation on Ru(0001) annealed to 1670 K. (a) Terrace completely covered with the triangular reconstruction. Inset demonstrates 180° rotation of the same type of triangular moiré cell on crossing a monatomic Ru step. (b) Triangular reconstruction around a Ru monatomic step, showing more reconstruction on the lower terrace. High-resolution images of the reconstruction with different triangular side lengths 8.7 nm (c) and 10.2 nm (d). Scan parameters are: (a) -150 mV and 11 pA; (b) -103 mV and 13 pA; (c) -151 mV and 17 pA; (d) -150 mV and 11 pA.

that reconstructs the topmost Ru layer. The triangular networks were found only in graphene-covered regions of the substrate and in two separate growth (segregation) preparations. These triangular networks were only observed near Ru steps, and can be larger than 700 nm in extent in some areas or just local around a monatomic step (the dislocation network in Fig. 3.33 (b) is decorated by water adsorbed at 130 K to enhance the contrast). In this image, the terrace below the step has more triangles than the upper terrace. In addition, the Ru step is faceted along the close-packed $<11\bar{2}0>$ Ru directions. The configuration around the Ru step could have resulted from a graphene sheet growing into the lower terrace followed by the growth of a separate sheet moving "downhill" on the upper Ru terrace.

The etched Ru atoms (pathway 2 in Fig. 3.31 (c)) can form the observed triangular networks by inserting themselves into the topmost Ru layer, so that the first Ru layer has a slightly higher atomic density. The high-resolution STM images 3.33 (c-d) reveal two types of triangular unit cells whose moiré patterns have different contrasts. We note that the imaging contrast of these structures was strongly voltage dependent. Adjacent cells are rotated by 180°. These observations suggest that one triangular cell type has the hcp stacking of the Ru while the other type has fcc stacking. Supporting this conclusion, the triangle orientation rotates 180° across a monatomic Ru step, as marked in the inset of Fig. 3.33 (a). The lines in Fig. 3.33 are thus Shockley partial dislocations that separate areas where the topmost atomic layer has unfaulted hcp stacking from areas of faulted fcc stacking, similar to reconstructions reported on Pt(111) [Bot93, Hoh95, Pus03] during Pt homoepitaxy. The size of the triangles is then determined by how much Ru is taken up by the first Ru layer and the corresponding contraction of the lattice.

To explain the structure of the dislocations and to estimate how many Ru atoms are involved, N. C. Bartelt (Sandia National Laboratories (Livermore, CA)) reproduced the triangle network with an atomic, two-dimensional Frenkel-Kontorova model of the topmost Ru layer [Log09]. We start with a moiré structure in which 41 Ru atoms are uniformly compressed to lie over 40 substrate atoms, yielding a unit cell size of 10.8 nm. Elastic relaxation in the top layer will concentrate the compression in regions away from the stable three-fold hollow sites of the substrate. To mimic this effect, we assume that nearest-neighbor Ru overlayer atoms interact through harmonic pairwise forces, while the substrate interaction is represented as a rigid sinusoidal two-dimensional potential. Figure 3.34 shows a model configuration that schematically reproduces the structure measured with STM in Fig. 3.33. In particular, after relaxation, the simulation accurately reproduces the triangular-shaped dislocations in the white-shaded regions in Fig. 3.34, as long as the energy difference between hcp and fcc regions is small enough that the areas of the two regions are similar. The dislocations in the Frenkel-Kontorova model lie along close-packed Ru directions, as also found in the STM images of Fig. 3.33. (Atomically resolved images of the clean Ru substrate were used to determine in-plane directions.) While not included in the Frenkel-Kontorova model of Fig. 3.34, the graphene lattice on top of the dislocated Ru layer contributes the periodic corrugation observed in the STM images of Fig. 3.33. While not completely proved, our model of the dislocation network in the topmost Ru layer well-describes the observed STM images. Since the model has extra Ru atoms in the topmost Ru layer, it provides evidence for the injection of Ru atoms underneath graphene. The validity of the model could be further evaluated using in-situ STM measurements. For example, whether the triangular

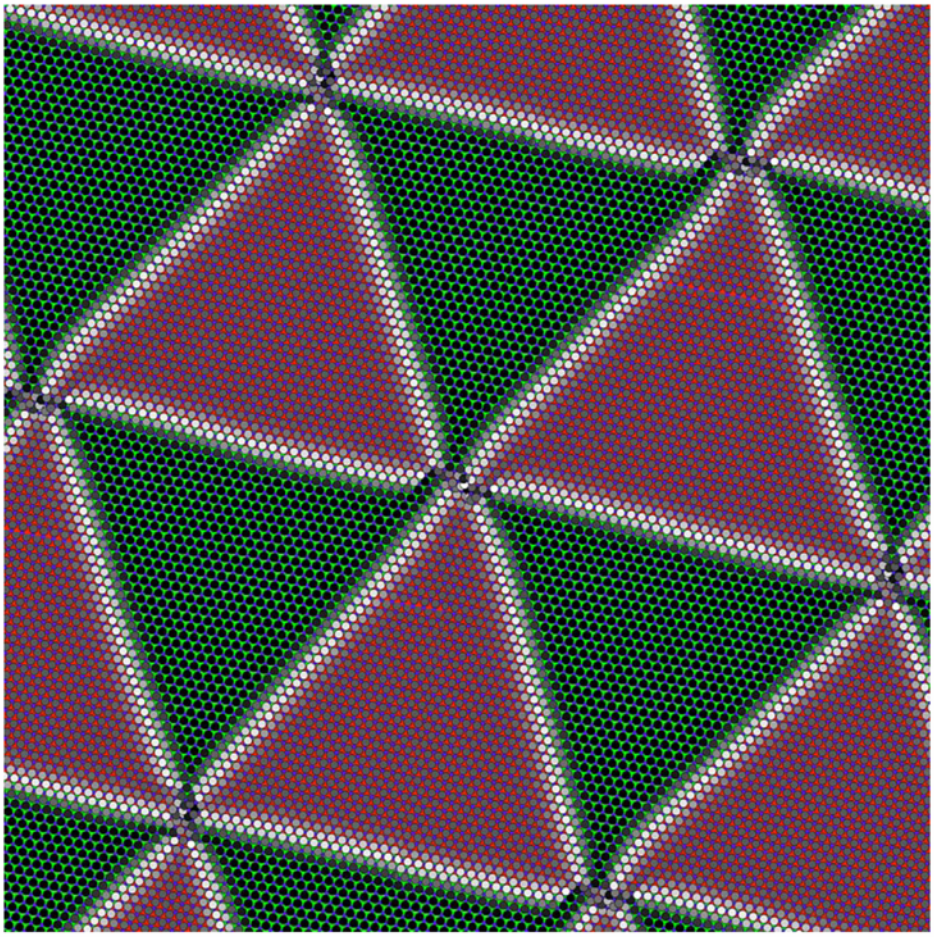

Figure 3.34: Frenkel-Kontorova model of dislocations in the topmost layer of Ru(0001). Green- and red-shaded regions represent the surface Ru atoms in hcp and fcc binding sites, respectively, separated by Shockley partial dislocations.

networks formed as Ru steps were etched by graphene growth could be evaluated, as could their fate after graphene removal by oxygen exposure or dissolution into the bulk. In addition, the amount of Ru needed to create the proposed dislocation network is quite small – on the order of 0.1% of a ML. Our LEEM observations suggest that much larger amounts of Ru can be injected under the graphene where growth by the etching mode dominates over the carpet mode. Thus, the nature of the injected Ru atoms varies with their concentration. At low concentration, the injected Ru atoms may form dislocation networks in the topmost Ru layer. At high concentration, DFT calculations suggest that under-graphene Ru islands occur.

In conclusion, our results show that graphene can grow on Ru(0001) by etching Ru steps. This growth mode is slower than graphene overgrowing descending Ru steps. On other substrates, the energetic barrier to attaching C atoms to a free graphene step edge may be even larger than for growth on Ru(0001) [Log08]. Thus, etching could dominate growth on these substrates. Indeed, the etching mode also occurs during growth on Pt(111) [Fuj05, Lan92] and Pd(111) [Kwo09]. Whether substrate atoms are also injected under graphene in these systems should be examined. The etching growth facets the Ru steps; therefore, graphene prefers particular bonding configurations at Ru steps. Step-etching also suggests that C bonds strongly to the Ru steps. Such tight bonding likely explains why graphene sheets do not grow up over the top of Ru steps, but etch the Ru step. The etching growth mode has important consequences for the properties of the graphene film. The Ru atoms injected under the graphene sheet result in a more complex geometry than a flat, bulk-terminated substrate overlain by a buckled graphene sheet. When the concentration of injected Ru atoms is low, dislocation networks in the Ru layer under the graphene can occur, as seen by STM. At the higher concentration of injected Ru atoms observed by LEEM, islands of Ru atoms may exist under the graphene, as suggested by DFT calculations. Characterizing these structural changes is important for understanding the physical properties of graphene sheets. For example, the chemical reactivity of the graphene sheet could well be modified by intercalated islands. In fact, we suggest that titrating the graphene film with metal adatoms can distinguish local regions with and without intercalated Ru islands. Lastly we remark on how unusual the etching mode is compared to typical film growth. Films commonly grow by atoms (molecules) attaching to the open site (a kink or a step) at the free edge of the film, because there the attachment barrier is zero or small [Bur51]. The ability of graphene to grow by displacing atoms on metal surfaces is another consequence of the exceptionally large barrier for direct adatom attachment [Log08].

3.4.2 Outlook: Water adsorption on graphene on Ru

Water interacts with interfaces all the range between strongly hydrophobic to strongly hydrophilic. In the above chapter, we investigated the wetting behavior of water on metallic surfaces, i.e., we focused on hydrophilic phenomena, where strong bonding of the first water layer to the substrate is given. For hydrophobic surfaces however, there is no such strong bonding, a fact that can lead to significant distortions away from the tetrahedral ice structure [Kim09]. Molecular dynamics predicted quasi-two-dimensional crystalline and amorphous ice between planar hydrophobic walls involving nontetrahedral bonding geometries, novel phase transi-

tions and anomalous self-diffusion [Zan04, Gio09, Cic08, Kog00, Kog97]. Yet, this has not been confirmed by experiments, until recently, when wetting of two-layer ice on hydrophobic graphene, grown on Pt(111), was observed – at a single hydrophobic interface and in absence of further confinement [Kim09]. Kimmel et al. applied LEED, reflection-absorption infrared spectroscopy (RAIRS), rare-gas adsorption/desorption and molecular dynamics to find that the new (metastable) crystalline ice polymorph consists of two *flat* hexagonal sheets of water molecules in which the hexagons in each sheet are stacked directly on top of each other, previously predicted for water confined between hydrophobic walls. Due to its particular structure – each molecule forms three hydrogen bonds with its neighbors within the layer, and a fourth hydrogen bond with a molecule in the other sheet, such that no dangling hydrogens appear on either surface of the ice film, i.e., these ice surfaces are expected to be hydrophobic. This two-layer ice was grown at temperatures of 100 - 135 K. Adsorption, desorption and growth of thin water films – wetting ice films as well as three-dimensional structures – on hydrophobic surfaces such as graphite have also been reported [Cha95, And07, San07, Yan09].

While ruthenium is a hydrophilic metallic surface, graphite is thus an example of a hydrophobic surface. By studying water adsorption on single graphite sheets, i.e., on *graphene* supported by Ru, as presented above (see Fig. 3.33), we intended to investigate the hydrophobic/hydrophilic character of this particularly reconstructed surface. We found that water, adsorbed at 130 K, initially adsorbs at the boundaries of the triangular superstructure (Shockley partial dislocations), see Fig. 3.35 (a), (b). Note that in each triangle, the graphene Moiré pattern is still visible. In Fig. 3.35 (c) and (d) we see enhanced water growth along the boundaries and growing towards the center of each triangle. The edge of the water stripe is not straight, it rather follows the moiré structure. These H_2O stripes are $\sim$ 3 nm wide and have an apparent height of $\sim$ 200 pm. Larger flat patches at their crossings seem to be built of ordered water structures, see Fig. 3.37. However, we cannot determine the structure due to limited resolution. A large-scale image for this water coverage can be seen in Fig. 3.36, which shows the fascinating surface reconstruction over 700 nm x 700 nm, the area corresponing to our maximum scan range. Larger water coverages are imaged in Fig. 3.35 (e) and (f). While in (e) some triangles are covered by water, in (f) the trend towards surface wetting is enhanced, indicating that complete wetting on graphene-precovered ruthenium might occur.

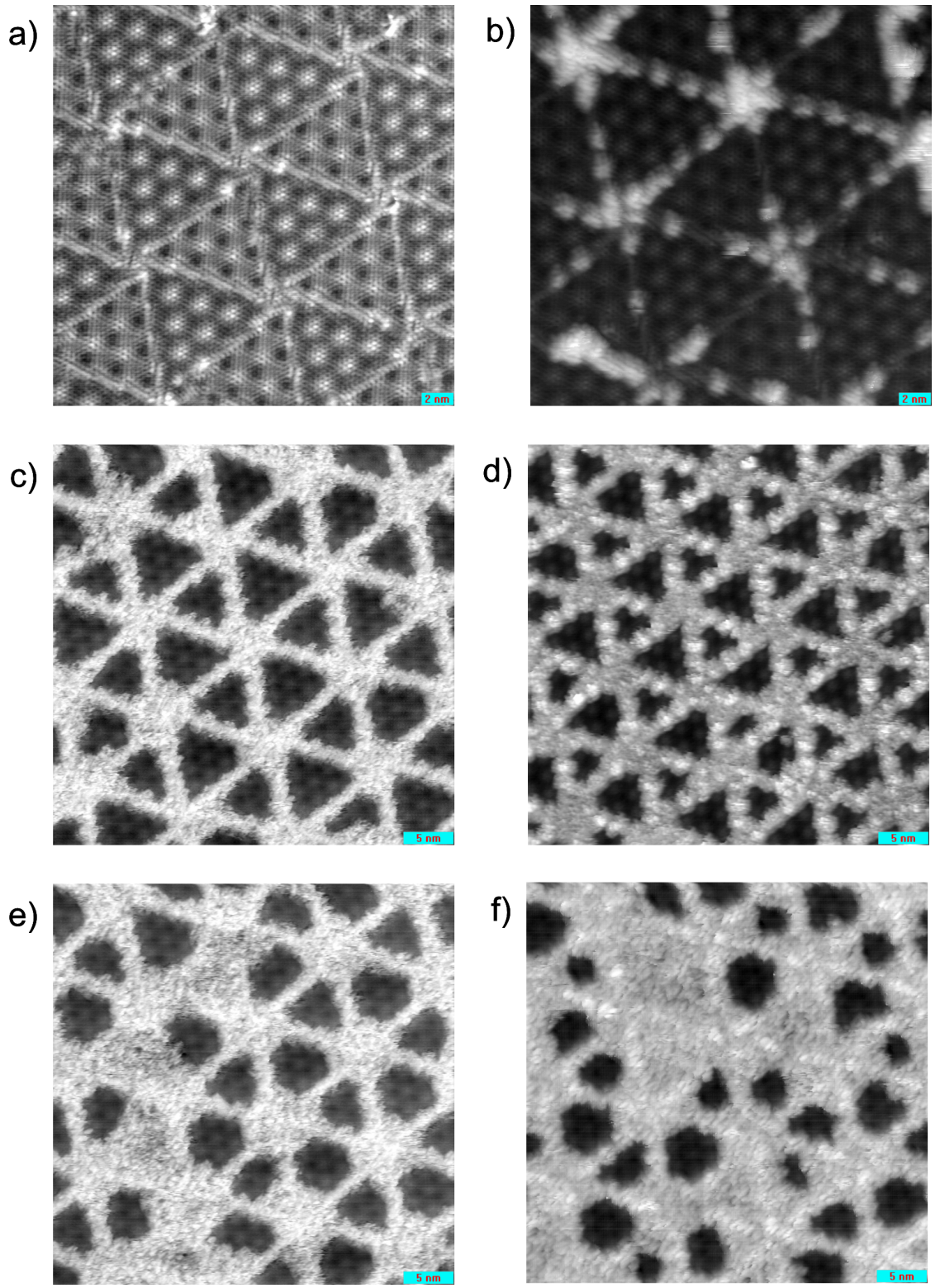

Figure 3.35: Different water coverages on Ru-supported graphene, adsorbed at 130 K. Scan parameters in (a) -151 mV, 17 pA, (b) -188 mV, 8 pA, (c) -141 mV, 9 pA, (d) -216 mV, 8 pA, (e) -150 mV, 11 pA, (f) -139 mV, 9 pA

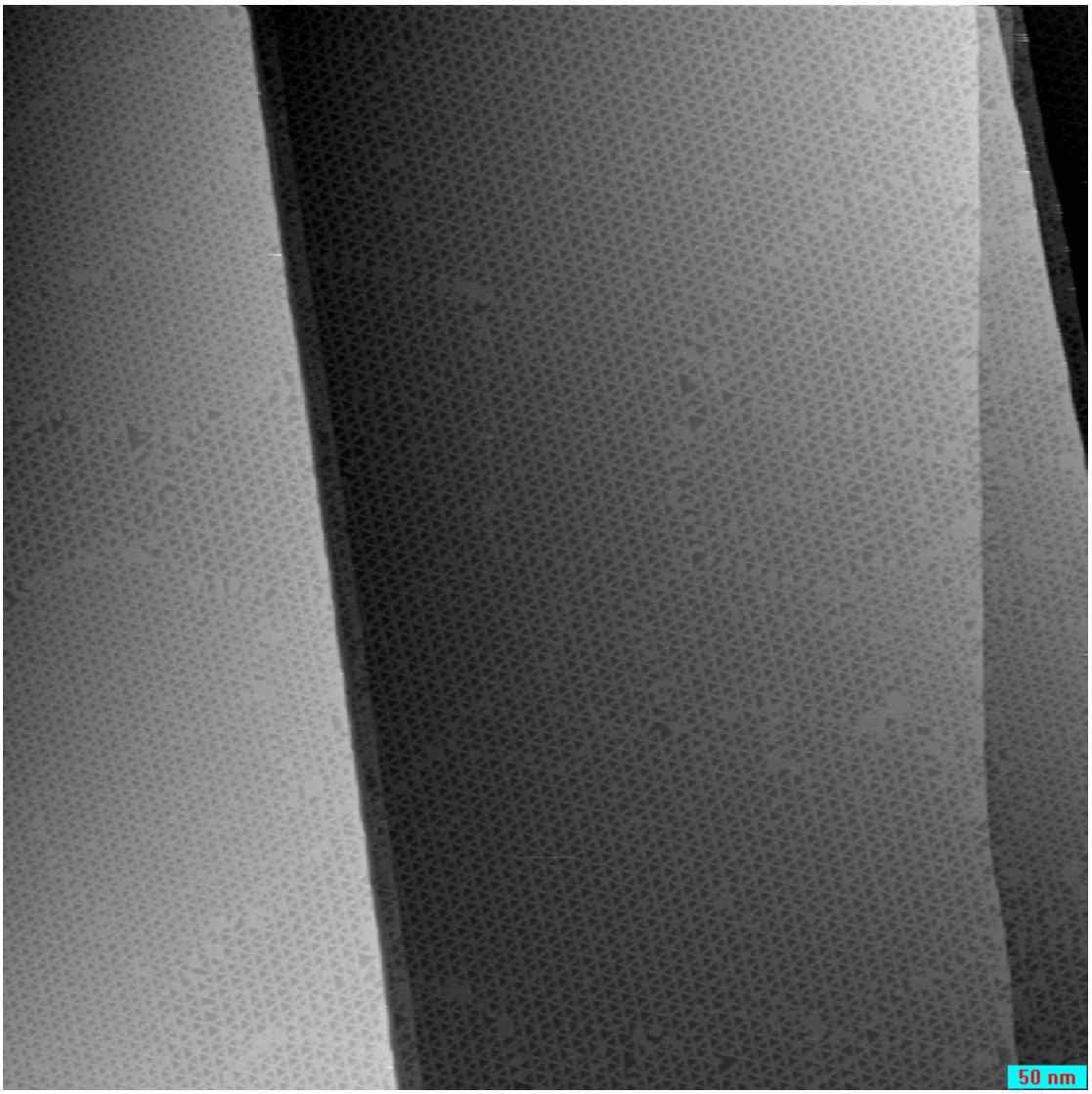

Figure 3.36: Large-scale image of water-covered graphene on Ru(0001). The coverage corresponds to the one shown in Fig. 3.35 (c). The image dimensions are 700 nm x 700 nm, and scan parameters of -270 mV, 13 pA were used.

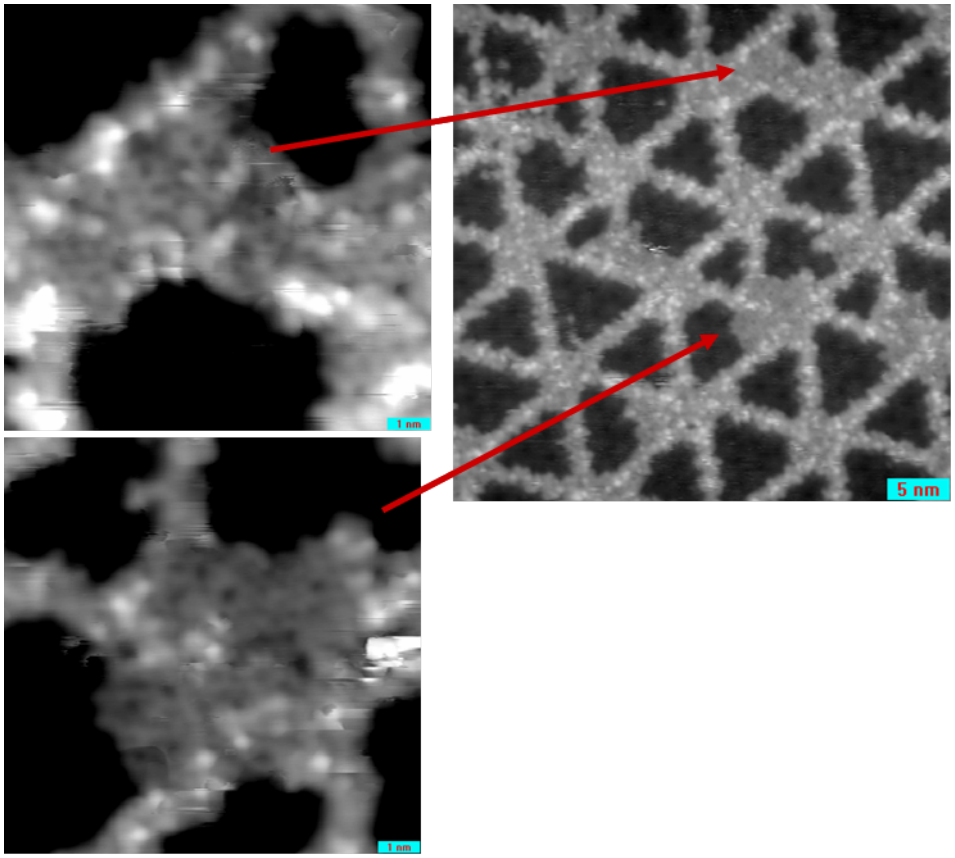

Figure 3.37: Larger flat water patches at the crossings of the water stripes seem to be ordered. Scan parameters were -155 mV, 11 pA, and -127 mV, 14 pA for the zoomed images.

Summary

In this thesis, we investigated growth and surface reactions of water and ammonia on Ru(0001) at the atomic scale. The main tool for our studies was a scanning tunneling microscope operated at low temperature.

The first part deals with single-molecule ammonia chemistry on ruthenium. Starting with adsorption and imaging of intact ammonia molecules, the succesive dehydrogenation reaction of ammonia was achieved by using the biased STM tip as a local probe to produce NH_2, NH and N on ruthenium. Experimental images of the different NH_x species (x = 0, 1, 2, 3) were taken and are nicely matched by STM simulations. Besides, initial and final state of the dehydrogenation reaction were experimentally confirmed to be the on-top site for NH_3 and the hcp hollow site for N, in agreement with density functional theory (DFT) calculations. In addition, complexes of NH_3 surrounded by up to three hydrogen atoms were found to be adsorbed with the surrounding hydrogen atoms at fcc sites and two Ru lattice spacings apart from each other. Indication for ammonia dimer formation and splitting was obtained, as well as an agreement of experimental and simulated STM images of the ammonia dimer.

After succeeding in the stepwise ammonia dehydrogenation, we aimed at gaining an understanding of the underlying dissociation processes. For that, we studied the effect of an applied electric field within the STM junction on the dehydrogenation of ammonia molecules. Experimentally, a linear dependence for the dissociation threshold voltage versus tip-sample distance Δz was measured for large Δz, which suggests an electric-field effect with critical fields of 0.11 ± 0.01 V/Å and -0.30 ± 0.01 V/Å for a positively and a negatively biased sample, respectively.

The effects of an applied electric field on dissociation barriers and thresholds along different reaction pathways were studied by DFT calculations and molecular dynamics (MD) simulations for the initial dissociation. Distinct reaction mechanisms were considered for the different bias polarities. For a positively biased sample, an increasing electrical field induces softening of the ammonia's umbrella mode resulting in the molecule being pulled towards the Ru surface and a widening of the H-N-H angles. The reaction energy barrier is also reduced by the applied field. By extrapolation a dissociation threshold of 0.2 V/Å is found, in quite good agreement with the experimental value. For a negative polarity, the calculations are work in progress. However, we know that a negative sample bias leads to a decrease in molecule-surface interaction. Smaller fields induce softening of the N-Ru stretch mode and cause desorption of the molecule at fields strengths greater than -0.058 V/Å. Dissociation becomes favorable at larger fields, although the exact mechanism that the dissociation is based on has not been understood yet.

The second part of this thesis covers the topics of water wetting and ice growth, first on pristine Ru(0001) and then on Ru precovered by oxygen as well as graphene.

In terms of the clean surface we characterized the first, second and multilayer growth between 110 and 145 K. The first layer consists of mixed water-hydroxyl structures that follow partial dissociation above 130 K, where the onset temperature for dissociation is strongly correlated with annealing duration. At about 130 K, elongated structures form instead of surface wetting in order to minimize the number of molecules bound with their plane nearly vertical to the surface. It was found that the elongated intact-water structures align with the compact atomic rows of the substrate, whereas the partially dissociated stripes are rotated by 30° relative to the intact stripes.

Partial dissociation goes along with liberated hydrogen atoms that form a ($\sqrt{3}$x$\sqrt{3}$) R30° structure between the mixed water-hydroxyl clusters. The three-fold fcc hollow site was confirmed by DFT calculations to be the hydrogen's most stable adsorption site. Partially dissociated water clusters that exhibit a darker contrast in the hexagonal centers of the clusters contain a hydrogen atom, as was found by comparison with STM image simulations.

Second-layer water molecules form clustered hexamers with an unexpected 30° rotation relative to the first layer, not observed in any phase of ice. Due to the flat geometry of the intact first-layer molecules, dangling H-bonds are inhibited, and growth of a second layer following an ice-like structure is not facilitated. Our experiments thus suggest that second-layer water might bind to the underlying intact water clusters by non-H-bonding interactions. Beyond the second water layer, growth of compact ice clusters was observed, although neither the first nor the second water layer were complete.

Water adsorption on Ru(0001) precovered by O(2x1) induces a well-ordered (4x2) superstructure at temperatures of 140 K. According to DFT, the unmodified O-(2x1) periodic surface should be hydrophobic. Interestingly however, water induces strong modifications to the structure of the O adlayer, which results in a wetting layer. Our study helps to understand the complex phenomena of wetting and reactivity at the most fundamental level. STM experiments and DFT calculations reveal that the adsorption of water causes the shift of up to half of the chemisorbed oxygen atoms from their preferred hcp sites to fcc sites, creating a (2x2) honeycomb structure where each water molecule is surrounded by six oxygen atoms. This oxygen honeycomb structure induced by the adsorption of water remains metastable after water desorption and does not revert to the stable linear 2x1 structure until temperatures close to 260 K, providing a template surface for the adsorption of small molecules, as it features two kinds of oxygen species.

Finally, graphene growth on ruthenium and the surface's wetting behavior were investigated. An unusual graphene growth mode by etching of Ru steps was observed, faceting the Ru step and injecting Ru atoms under the graphene sheet. If the concentration of injected Ru atoms is low, dislocation networks in the Ru layer under the graphene can occur. At higher concentration, islands of Ru atoms may exist under the graphene, as suggested by DFT calculations. A characterization of the structural changes is important for an understanding of the physical properties and the chemical reactivity of graphene sheets.

By adsorbing water on ruthenium-supported graphene at 130 K, we studied the hydrophobicity/hydrophilicity of this particularly reconstructed surface. We found that water initially adsorbs at the boundaries of the triangular superstructure, while the Moiré pattern can still be seen inside the triangles. Larger coverages lead to en-

hanced water growth along the boundaries and towards the centers of the triangles. The trend towards surface wetting indicates that complete wetting on graphene-precovered ruthenium might be possible.

Both of the two molecules that were investigated throughout this thesis – water and ammonia – contain hydrogen atoms and commonly form structures via hydrogen bonding. Future experiments might be conducted in order to explore their interactions when co-adsorbing them on a surface.

Acknowledgements

This thesis would not have been possible without many people's help. I would like to express my gratitude to all of them for their support and assistance.

I owe my deepest gratitude to my advisors Nacho Pascual (Berlin) and Miquel Salmeron (Berkeley) for their collaboration to accomplish this dissertation. I appreciate their guidance and engagement throughout my PhD, and the great freedom to pursue independent work.

For offering to co-referee this thesis, I would like to thank Wolfgang Kuch.

I am grateful to Sabine Maier for investing her time and energy in the lab as well as for many discussions, and for improving the quality of this dissertation.

During the first stage of my PhD I had the pleasure to learn technical skills and gain insight into the group's ongoing research thanks to Tomoko Shimizu and Aitor Mugarza.

I owe special debts to our collaboration partners:

- Aaron Sisto, Alexey Zayak and Jeff Neaton at Lawrence Berkeley Lab for DFT calculations and MD simulations within the ammonia project.
- Jorge Cerdá at Instituto de Ciencia de Materiales de Madrid (Spain) for DFT calculations and STM image simulations of ammonia and water-hydroxyl species.
- Pepa Cabrera-Sanfelix, Daniel Sánchez-Portal and Andrés Arnau at Donostia International Physics Center, San Sebastian (Spain) for DFT calculations and STM image simulations within the scope of water adsorption on oxygen-covered ruthenium.
- Elena Starodub and Kevin McCarty at Sandia National Laboratories (Livermore, CA) for LEEM experiments, and Norman Bartelt (Sandia National Laboratories (Livermore, CA)) and Peter Feibelman at Sandia National Laboratories (Albuquerque, NM) for theoretical support in the context of graphene growth on ruthenium.

Lastly, I would like to thank everybody I have been working with in Berkeley and Berlin. Warmest thanks go to all of those who supported me in any respect during the completion of this project.

Curriculum Vitae

For reasons of privacy there is no CV available online.

Publications

- L. Grill, I. Stass, K.-H. Rieder, F. Moresco, Preparation of self-ordered molecular layers by pulse injection, Surf. Sci. Lett. **600**, L143 (2006).
- E. Starodub, S. Maier, I. Stass, N. C. Bartelt, P. J. Feibelman, M. Salmeron, and K. F. McCarty, *Graphene Growth by Metal Etching on Ru(0001)*, Phys. Rev. B **80**, 235422 (2009).
- S. Maier, P. Cabrera-Sanfelix, I. Stass, D. Sánchez-Portal, A. Arnau, M. Salmeron, *Water Induced Surface Reconstruction of the Oxygen (2x1) covered Ru(0001)*, submitted.
- *Adsorption and identification of NH_x species on Ru(0001)*, in preparation.
- *Successive dehydrogenation of single ammonia molecules on ruthenium*, in preparation.
- *Structure and formation of mixed water-hydroxyl structures following partial dissociation of water on Ru(0001)*, in preparation.
- *Growth of intact water on ruthenium*, in preparation.

Bibliography

[And04] K. Andersson, A. Nikitin, L. G. M. Pettersson, A. Nilsson, H. Ogasawara, *Water Dissociation on Ru(001): An Activated Process*, Phys. Rev. Lett. **93**, 196101 (2004).

[And07] P. U. Andersson, M. T. Suter, N. Markovic, J. B. C. Petterson, *Water Condensation on Graphite Studied by Elastic Helium Scattering and Molecular Dynamics Simulations*, J. Phys. Chem. C **111**, 15258 (2007).

[Ash76] N.W. Ashcroft, N.D. Mermin, *Solid State Physics*, Saunders College Publishing International Edition (1976).

[Bal03] P. Ball, *How to keep dry in water*, Nature **423**, 25 (2003).

[Bal08] P. Ball, *Water-an enduring mystery*, Nature **452**, 291 (2008).

[Bar61] J. Bardeen, *Tunnelling from a Many-Particle Point of View*, Phys. Rev. Lett. **6**, 57 (1961).

[Bar99] L. Bartels, M. Wolf, T. Klamroth, P. Saalfrank, A. Kühnle, G. Meyer, K.-H. Rieder, *Atomic-scale chemistry: Desorption of ammonia from Cu(111) induced by tunneling electrons*, Chem. Phys. Lett. **313**, 544 (1999).

[Beh97] S. Behler, M. K. Rose, J. C. Dunphy, D. F. Ogletree, M. Salmeron, C. Chapelier, *Scanning tunneling microscope with continuous flow cryostat sample cooling*, Rev. Sci. Instrum. **68**, 2479-2485 (1997).

[Bin82] G. Binnig, H. Rohrer, C. Gerber, E. Weibel, *Tunneling through a controllable vacuum gap*, Appl. Phys. Lett. **40**, 178 (1982).

[Bin82b] G. Binnig, H. Rohrer, C. Gerber, E. Weibel, *Surface Studies by Scanning Tunneling Microscopy*, Phys. Rev. Lett. **49**, 57 (1982).

[Bin83] G. Binnig, H. Rohrer, C. Gerber, E. Weibel, *7 x 7 Reconstruction on Si(111) Resolved in Real Space*, Phys. Rev. Lett. **50**, 120 (1983).

[Blö94] P. E. Blöchl, *Projector augmented-wave method*, Phys. Rev. B **50**, 17953 (1994).

[Boc00] J. O'M Bockris, A. K. N. Reddy, M. Gamboa-Aldeco, *Modern electrochemistry*, Vol. 2, Kluwer Academic/Plenum Publishers (2000).

[Bot93] M. Bott, M. Hohage, T. Michely, and G. Comsa, *Pt(111) reconstruction induced by enhanced Pt gas-phase chemical potential*, Phys. Rev. Lett. **70**, 1489 (1993).

[Bov05] U. Bovensiepen, C. Gahl, J. Stähler, M. Wolf, *Ultrafast electron dynamics in amorphous and crystalline D_2O layers on Ru(001)*, Surf. Sci. **584**, 90 (2005).

[Bur51] W. K. Burton, N. Cabrera, and F. C. Frank, *The growth of crystals and the equilibrium structure of their surfaces*, Philos. Trans. R. Soc. London Ser. A **243**, 299 (1951).

[Cab07] P. Cabrera-Sanfelix, D. Sanchez-Portal, A. Mugarza, T. K. Shimizu, M. Salmeron, A. Arnau, *Water adsorption on O(2x2)/Ru(0001): STM experiments and first-principles calculations*, Phys. Rev. B **76**, 205438 (2007).

[Cab08] P. Cabrera-Sanfelix, A. Arnau, A. Mugarza, T. K. Shimizu, M. Salmeron, D. Sanchez-Portal, *Decisive role of the energetics of dissociation products in the adsorption of water on O/Ru(0001)*, Phys. Rev. B **78**, 155438 (2008).

[Cal04] F. Calleja, A. Arnau, J. J. Hinarejos, A. L. V. de Parga, W. A. Hofer, P. M. Echenique, R. Miranda, *Contrast Reversal and Shape Changes of Atomic Adsorbates Measured with Scanning Tunneling Microscopy*, Phys. Rev. Lett. **92**, 206101 (2004).

[Cer97] J. Cerdá, M. A. Van Hove, P. Sautet and M. Salmeron, *Efficient method for the simulation of STM images. I. Generalized Green-function formalism*, Phys. Rev. B **56,** 15885 (1997).

[Cer04] J. Cerdá, A. Michaelides, M.-L. Bocquet, P. J. Feibelman, T. Mitsui, M. Rose, E. Fomin, M. Salmeron, *Novel water overlayer growth on Pd(111) characterized with scanning tunneling microscopy and density functional theory*, Phys. Rev. Lett. **93**, 116101 (2004).

[Cha95] D. V. Chakarov, L. Osterlund, B. Kasemo, *Water adsorption on graphite (0001)*, Vacuum **46**, 1109 (1995).

[Cho01] T.V. Choudhary, C. Sivadinarayana, D.W. Goodman, *Catalytic ammonia decomosition: CO_x-free hydrogen production for fuel cell applications*, Catal. Lett. **72**, 197 (2001).

[Cic08] G. Cicero, J. C. Grossman, E. Schwegler, F. Gygi, G. Galli, *Water confined in nanotubes and between graphene sheets: a frist principles study*, J. Am. Chem. Soc. **130**, 1871 (2008).

[Cla04] C. Clay, S. Haq, A. Hodgson, *Intact and dissociative adsorption of water on Ru(0001)*, Chem. Phys. Lett. **388**, 89 (2004).

[Cor05] C. Corriol, F. Calleja, A. Arnau, J. J. Hinarejos, A. L. V. de Parga, W. A. Hofer, R. Miranda, *Role of surface geometry and electronic structure in STM images of O/Ru(0 0 0 1)*, Chem. Phys. Lett. **405**, 131 (2005).

[Cor08] J. Coraux, A. T. N'Diaye, C. Busse, and T. Michely, *Structural coherency of graphene on Ir(111)*, Nano Lett. **8**, 565 (2008).

[Cor09] J. Coraux, A. T. N'Diaye, M. Engler, C. Busse, D. Wall, N. Buckanie, F. J. M. Z. Heringdorf, R. van Gastei, B. Poelsema, and T. Michely, *Growth of graphene on Ir(111)*, New J. Phys. **11**, 023006 (2009).

[Cro93] M. F. Crommie, C. P. Lutz, D. M. Eigler, *Confinement of Electrons to Quantum Corrals on a Metal Surface*, Science **262**, 218 (1993).

[Dai97] Q. Dai, J. Hu, and M. Salmeron, *Adsorption of water on NaCl (100) surfaces: Role of atomic steps*, J. Phys. Chem. B **101**, 1994 (1997).

[Dan78] L. R. Danielson, M. J. Dresser, E. E. Donaldson, J. T. Dickinson, *Adsorption and desorption of ammonia, hydrogen and nitrogen on ruthenium (0001)*, Surf. Sci. **71**, 599 (1978).

[Den03] D. N. Denzler, S. Wagner, M. Wolf, G. Ertl, *Isotope effects in the thermal desorption of water from Ru(001)*, Surf. Sci. **532**, 113 (2003).

[Dia09] B. Diawara, L. Joubert, D. Costa, P. Marcus, C. Adamo, *Ammonia on Ni(111) surface studied by first principles, Bonding, multilayers structure and comparison with experimental IR and XPS data*, Surf. Sci. 603, 3025 (2009).

[Die96] H. Dietrich, K. Jacobi, G. Ertl, *Coverage, lateral order, and vibrations of atomic nitrogen on Ru(0001)*, J. Chem. Phys. **105**, 8944 (1996).

[Doe82] D. L. Doering, T. E. Madey, *The Adsorption of Water on Clean and Oxygen-Dosed Ru(001)*, Surf. Sci. **123**, 305 (1982).

[Eig90] D. M. Eigler, E. K. Schweizer, *Positioning single atoms with a scanning tunnelling microscope*, Nature **344**, 524 (1990).

[Far05] N. S. Faradzhev, K. L. Kostov, P. Feulner, T. E. Madey, D. Menzel, *Stability of water monolayers on Ru(0001): Thermal and electronically induced dissociation*, Chem. Phys. Lett. **415**, 165(2005).

[Fei02] P. J. Feibelman, *Partial Dissociation of Water on Ru(0001)*, Science **295**, 99 (2002).

[Fei10] P. J. Feibelman, *The first wetting layer on a solid*, Physics Today **63**, 34 (2010).

[Fow28] R. H. Fowler, L. Nordheim, *Electron Emission in Intense Electric Fields*, Proc. Roy. Soc. London **A119**, 173 (1928).

[Fuj05] T. Fujita, W. Kobayashi, and C. Oshima, *Novel structures of carbon layers on a Pt(111) surface*, Surf. Interface Anal. **37**, 120 (2005).

[Gei07] A. K. Geim, K. S. Novoselov, *The rise of graphene*, Nat. Mat. **6**, 183 (2007).

[Gia60] I. Giaever, *Energy Gap in Superconductors Measured by Electron Tunneling*, Phys. Rev. Lett. **5**, 147 (1960).

[Gia60b] I. Giaever, *Electron Tunneling between two Superconductors*, Phys. Rev. Lett. **5**, 464 (1960).

[Gib00] K. D. Gibson, M.Viste, S. J. Sibener, *The adsorption of water on clean and oxygen pre-dosed Rh(111): Surface templating via (1x1)-O/Rh(111) induces formation of a novel high-density ice structure*, Chem. Phys. **112**, 9582 (2000).

[Gio09] N. Giovambattista, P. J. Rossky, P. G. Debenedetti, *Phase Transitions Induced by Nanoconfinement in Liquid Water*, Phys. Rev. Lett. **102**, 050603 (2009).

[Gla05] M. J. Gladys, A. Mikkelsen, J. N. Andersen, G. Held, *Water adsorption on O-covered Ru{0001}: Coverage-dependent change from dissociation to molecular adsorption*, Chem. Phys. Lett. **414**, 311 (2005).

[Gla08] M. J. Gladys, A. A. El-Zein, A. Mikkelsen, J. N. Anderson, G. Held, *Modifying the adsorption characteristics of water on Ru{0001} with preadsorbed oxygen*, Phys. Rev. B **78**, 035409 (2008).

[Gle97] A. L. Glebov, A. P. Graham, A. Menzel, J. P. Toennies, *Orientational ordering of two-simensional ice on Pt(111)*, J. of Chem. Phys. **106**, 9382 (1997).

[Gro39] W. R. Grove, *On voltaic series and the combination of gases by platinum*, Philos. Mag. Series 3, 127 (1839).

[Hak94] H. Haken und H. C. Wolf, *Molekülphysik und Quantenchemie*, 2. Auflage, Springer, Berlin (1994).

[Han87] P. K. Hansma, J. Tersoff, *Scanning tunneling microscopy*, J. Appl. Phys. **61**, R1 (1987).

[Haq06] S. Haq, C. Clay, G. R. Darling, G. Zimbitas, A. Hodgson, *Growth of intact water ice on Ru(0001) between 140 and 160 K: Experiment and density-functional theory calculations*, Phys. Rev. B **73**, 115414 (2006).

[Haq07] S. Haq, and A. Hodgson, *Multilayer Growth and Wetting of Ru(0001)*, J. Phys. Chem. C **111**, 5946 (2007).

[Hel94] G. Held, D. Menzel, *The structure of the p($\sqrt{3}$ x $\sqrt{3}$)R30° bilayer of D_2O on Ru(001)*, Surf. Sci. **316,** 92 (1994).

[Hel95] G. Held, D. Menzel, *Isotope Effects in Structure and Kinetics of Water Adsorbates on Ru(001)*, Surf. Sci. **327**, 301(1995).

[Hel09] A. Hellman, K. Honkala, I. N. Remediakis, A. Logadottir, A. Carlsson, S. Dahl, C. H. Christensen, J. K. Nørskov, *Ammonia synthesis and decomposition on a Ru-based catalyst modeled by first-principles*, Surf. Sci. **603**, 1731 (2009).

[Hen02] M. A. Henderson, *The interaction of water with solid surfaces: fundamental aspects revisited*, Surf. Sci. Rep. **46**, 5 (2002).

[Hla00] S.-W. Hla, L. Bartels, G. Meyer, K.-H. Rieder, *Inducing All Steps of a Chemical Reaction with the Scanning Tunneling Microscope Tip: Towards Single Molecule Engineering*, Phys. Rev. Lett. **85**, 2777 (2000).

[Hof91] F. M. Hoffmannn, M. D.Weisel, C. H. F. Peden, *In-situ FT-IRAS study of the CO oxidation reaction over Ru(001): II. Coadsorption of carbon monoxide and oxygen*, Surf. Sci. **253**, 59 (1991).

[Hoh64] P. Hohenberg, W. Kohn, *Inhomogeneous Electron Gas*, Phys. Rev. **136**, B864 (1964).

[Hoh65] P. Hohenberg, W. Kohn, *Inhomogenous Electron Gases*, Phys. Rev. B **136**, B864 (1965).

[Hoh95] M. Hohage, T. Michely, and G. Comsa, *Pt(111) network reconstruction – structure, growth and decay*, Surf. Sci. **337**, 249 (1995).

[Hon05] K. Honkala, A. Hellman, I. N. Remediakis, A. Logadottir, A. Carlsson, S. Dahl, C. H. Christensen, J. K. Nørskov, *Ammonia Synthesis from First-Priciples Calculations*, Science **307**, 555 (2005).

[Ito08] M. Ito, *Structures of water at electrified interfaces: Microscopic understanding of electrode potential in electric double layers on electrode surfaces*, Surf. Sci. Rep. **63**, 329 (2008).

[Jac00] K. Jacobi, *Nitrogen on Ruthenium Single-Crystal Surfaces*, Phys. Status Solidi A, **177**, 37 (2000).

[Jak97] P. Jakob, M. Stichler, D. Menzel, *The adsorption of NO on Ru(001) and on O(2 × 1)/Ru(001) revisited*, Surf. Sci. **370**, L185 (1997).

[Jan08] B. Janta-Polczynski, J. I. Cerdá, G. Ethier-Majcher, K. Piyakis, A. Rochefort, *Parallel Scanning Tunneling Microscopy Imaging of Low Dimensional Nanostructures*, J. Appl. Phys. **104,** 23702 (2008).

[Kat07] S. Katano, Y. Kim, M. Hori, M. Trenary, M. Kawai, *Reversible Control of Hydrogenation of a Single Molecule*, Science **316**, 1883 (2007).

[Kim02] Y. Kim, T. Komeda, M. Kawai, *Single-Molecule Reaction and Characterization by Vibrational Excitation*, Phys. Rev. Lett. **89**, 126104 (2002).

[Kim05] G. A. Kimmel, N. G. Petrik, Z. Dohnálek, B. D. Kay, *Crystalline Ice Growth on Pt(111): Observation of a Hydrophobic Water Monolayer*, Phys. Rev. Lett. **95**, 166102 (2005).

[Kim09] G. A. Kimmel, J. Matthiesen, M. Baer, C. J. Mundy, N. G. Petrik, R. S. Smith, Z. Dohnálek, B. D. Kay, *No Confinement Needed: Observation of a Metastable Hydrophobic Wetting Two-Layer Ice on Graphene*, J. Am. Chem. Soc. **131**, 12838 (2009).

[Kle08] A. Klerke, C. H. Christensen, J. K. Nørskov, T. Vegge, *Ammonia for hydrogen storage: challenges and opportunities*, J. Mater. Chem. **18**, 2304 (2008).

[Kog97] K. Koga, X. C. Zeng, H. Tanaka, *Freezing of confined water: A bilayer ice phase in hydrophobic nanopores*, Phys. Rev. Lett. **79**, 5262 (1997).

[Kog00] K. Koga, H. Tanaka, X.C. Zeng, *First-order transition in confined water between high-density liquid and low-density amorphous phases*, Nature **408**, 564 (2000).

[Koh65] W. Kohn, L. J. Sham, *Self-Conistent Equations Including Exchange and Correlation Effects*, Phys. Rev. **140**, A1133 (1965).

[Koh99] W. Kohn, *Nobel Lecture: Electronic structure of matter - wave functions and density functionals*, Rev. Mod. Phys. **71**, 1253 (1999).

[Kon06] T. Kondo, S. Mae, H. S. Kato, M. Kawai, *Morphological change of D_2O layers on Ru(0001) probed with He atom scattering*, Surf. Sci. **600**, 3570 (2006).

[Kos92] K. L. Kostov, H. Rauscher, D. Menzel, *Adsorption of CO on oxygen-covered Ru(001)*, Surf. Sci. **278**, 62 (1992).

[Kos04] K. L. Kostov, W. Widdra, D. Menzel, *Hydrogen on Ru(001) revisited, vibrational structure, adsorption states, and lateral coupling*, Surf. Sci. **560**, 130 (2004).

[Kre82] K. Kretzschmar, J. K. Sass, A. M. Bradshaw, S. Holloway, S. Surf. Sci. **115**, 183 (1982).

[Kre93] G. Kresse, J. Hafner, *Ab initio molecular dynamics for liquid metals*, Phys. Rev. B **47**, 558 (1993).

[Kre93b] G. Kresse, J. Hafner, *Ab initio molecular dynamics for open-shell transition metals*, Phys. Rev. B **48** 13115 (1993).

[Kre94] G. Kresse, J. Hafner, *Ab initio molecular-dynamics simulation of the liquid-metal–amorphous-semiconductor transition in germanium*, Phys. Rev. B **49** 14251 (1994).

[Kre96] G. Kresse and J. Furthmüller, *Efficiency of ab-initio total energy calculations for metals and semiconductors using a plane-wave basis set*, Comp. Mat. Sci. **6**, 15 (1996).

[Kre96b] G. Kresse, J. Furthmüller, *Efficient iterative schemes for ab initio total-energy calculations using plane-wave basis set*, Phys. Rev. B **54**, 11169 (1996).

[Kre99] G. Kresse, D. Joubert, *From ultrasoft pseudopotentials to the projector augmented-wave method*, Phys. Rev. B **59**, 1758 (1999).

[Kun83] K. Kunc and R. Resta, *External Fields in the Self-Consistent Theory of Electronic States: A New Method for Direct Evaluation of Macroscopic and Microscopic Dielectric Response*, Phys. Rev. Lett. **51**, 686 (1983).

[Kwo09] S.-Y. Kwon, C. V. Ciobanu, V. Petrova, V. B. Shenoy, J. Bareo, V. Gambin, I. Petrov, and S. Kodambaka, *Growth of Semiconducting Graphene on Palladium*, Nano Lett. **9**, 3985 (2009).

[Lan86] N. D. Lang, *Theory of Single-Atom Imaging in the Scanning Tunneling Microscope*, Phys. Rev. Lett. **56**, 1164 (1986).

[Lan86b] N. D. Lang, *Spectroscopy of single atoms in the scanning tunneling microscope*, Phys. Rev. B, **34**, 5947 (1986).

[Lan92] T. A. Land, T. Michely, R. J. Behm, J. C. Hemminger, and G. Comsa, *STM investigation of single layer graphite structures produced on Pt(111) by hydrocarbon decomposition*, Surf. Sci. **264**, 261 (1992).

[Lip89] P. H. Lippel, R. J. Wilson, M. D. Miller, C. Wöll, S. Chiang, *High-Resolution Imaging of Copper-Phthalocyanine by Scanning-Tunneling Microscopy*, Phys. Rev. Lett. **62**, 171 (1989).

[Log03] Á. Logadóttir, J. K. Nørskov, *Ammonia synthesis over a Ru(0001) surface studied by density functional calculations*, J. Catal. **220**, 273 (2003).

[Log08] E. Loginova, N. C. Bartelt, P. J. Feibelman, K. F. McCarty, *Evidence for graphene growth by C cluster attachment*, New J. Phys. **10**, 093026 (2008).

[Log09] E. Loginova, S. Nie, N. C. Bartelt, K. Thürmer, and K. F. McCarty, *Defects of graphene on Ir(111): Rotational domains and ridges*, Phys. Rev. B **80**, 085430 (2009).

[Log09b] E. Loginova, N. C. Bartelt, P. J. Feibelman, and K. F. McCarty, *Factors influencing graphene growth on metal surfaces*, New J. Phys. **11**, 063046 (2009).

[Log09c] E. Starodub, S. Maier, I. Stass, N. C. Bartelt, P. J. Feibelman, M. Salmeron, K. F. McCarty, *Graphene Growth by Metal Etching on Ru(0001)*, Phys. Rev. B **80**, 235422 (2009).

[Lor00] N. Lorente, M. Persson, *Theory of Single Molecule Vibrational Spectroscopy and Microscopy*, Phys. Rev. Lett. **85,** 2997 (2000).

[Lor00b] N. Lorente, M. Persson, *Theoretical aspects of tunneling-current-induced bond excitation and breaking at surfaces*, Faraday Discuss. **117**, 277 (2000).

[Mad82] T. E. Madey, F. P. Netzer, *The adsorption of H2O on Ni (111): influence of preadsorbed oxygen on azimuthal ordering*, Surf. Sci. **117**, 549 (1982).

[Mar02] P. Maragakisa, S. A. Andreev, Y. Brumer, D. R. Reichman, E. Kaxiras, *Adaptive nudged elastic band approach for transition state calculation*, J. Chem. Phys. **117**, 4651 (2002).

[Mar04] R. M. Martin, *Electronic structure: Basic theory and practical methods*, Cambridge University Press (2004).

[Mar07] S. Marchini, S. Günther, J. Wintterlin, *Scanning tunneling microscopy of graphene on Ru(0001),* Phys. Rev. B **76,** 075429 (2007).

[Mar08] D. Martoccia, P. R. Willmott, T. Brugger, M. Bjorck, S. Gunther, C. M. Schleputz, A. Cervellino, S. A. Pauli, B. D. Patterson, S. Marchini, J. Wintterlin, W. Moritz, and T. Greber, *Graphene on Ru(0001): A 25×25 supercell*, Phys. Rev. Lett. **101**, 126102 (2008).

[Mat05] G. Materzanini, G. F. Tantardini, P. J. D. Lindan, P. Saalfrank, *Water adsorption at metal surfaces: A first-principles study of the p($\sqrt{3}x\sqrt{3}$)R30° H_2O bilayer on Ru(0001)*, Phys. Rev. B **71**, 155414 (2005).

[May06] A. J. Mayne, G. Dujardin, G. Comtet, D. Riedel, *Electronic Control of Single-Molecule Dynamics*, Chem. Rev. **106**, 4355 (2006).

[McC09] K. F. McCarty, P. J. Feibelman, E. Loginova, and N. C. Bartelt, *Kinetics and thermodynamics of carbon segregation and graphene growth on Ru(0001)*, Carbon **47**, 1806 (2009).

[Meh07] M. Mehlhorn, K. Morgenstern, *Faceting during the Transformation of Amorphous to Crystalline Ice*, Phys. Rev. Lett. **99**, 246101 (2007).

[Mei97] K. Meinel, H. Wolter, Ch. Ammer, A. Beckmann, H. Neddermeyer, *Adsorption stages of O on Ru(0001) studied by means of scanning tunnelling microscopy*, J. Phys.: Condens Matter **9**, 4611 (1997).

[Men05] S. Meng, Wang, E. G. Frischkorn, M. Wolf, S. W. Gao, *Consistent picture for the wetting structure of water/Ru(0001)*, Chem.Phys. Lett. **402**, 384 (2005).

[Mic03] A. Michaelides, A. Alavi, D. A. King, *Different surface chemistries of water on Ru{0001}: From monomer adsorption to partially dissociated bilayers*, J. Am. Chem. Soc. **125**, 2746 (2003).

[Mug08] A. Mugarza, T. K. Shimizu, P. Cabrera-Sanfelix, D. Sanchez-Portal, A. Arnau, M. Salmeron, *Adsorption of Water on O(2x2)/Ru(0001): Thermal Stability and Inhibition of Dissociation*, J. Phys. Chem. C **112**, 14052 (2008).

[Mug09] A. Mugarza, T. K. Shimizu, D. F. Ogletree, M. Salmeron, *Chemical reactions of water molecules on Ru(0001) induced by selective excitation of vibrational modes*, Surf. Sci. **603**, 2030 (2009).

[Nak02] O. Nakagoe, N. Takagi, and Y. Matsumoto, *Thermal decomposition of acetylene on Pt(111) studied by scanning tunneling microscopy*, Surf. Sci. **514**, 414 (2002).

[Nar94] B. Narloch, G. Held, D. Menzel, *Structural rearrangement by coadsorption: a LEED IV determination of the Ru(001)-p(2 × 2)(2O + CO) structure*, Surf. Sci. **317**, 131 (1994).

[N'Di08] T. N'Diaye, S. Bleikamp, P. J. Feibelman, and T. Michely, *Two-Dimensional Ir Cluster Lattice on a Graphene Moire on Ir(111)*, Phys. Rev. Lett. **101**, 219904 (2008).

[Nis64] Y. Nishijima, and G. Oster, *Moiré Patterns: Their Application to Refractive Index and Refractive Index Gradient Measurements*, J. Opt. Soc. Am. **54**, 1 (1964).

[Nov04] K. S. Novoselov, A. K. Geim, S. V. Morozov, D. Jiang, Y. Zhang, S. V. Dubonos, I. V. Grigorieva, A. A. Firsov, *Electric Field Effect in Atomically Thin Carbon Films*, Science **306**, 666 (2004).

[Off06] W. K. Offermanns, A. P. J. Jansen, R. A. van Santen, *Ammonia activation on platinum{111}: A density functional theory study*, Surf. Sci. **600**, 1714 (2006).

[Pan99] S. H. Pan, E. W. Hudson, J. C. Davis, *^{3}He refrigerator based very low temperature scanning tuenneling microscope*, Rev. Sci. Instrum. **70**, 1459 (1999).

[Pan08] Y. Pan, H. Zhang, D. Shi, J. Sun, S. Du, F. Liu, H.-J. Gao, *Highly Ordered, Millimeter-Scale, Continuous, Single-Crystalline Graphene Monolayer Formed on Ru(0001)*, Adv. Mat. **20**, 1 (2008).

[Par88] J. E. Parmeter, Y. Wang, C. B. Mullins, W. H. Weinberg, *Electron energy loss spectroscopy of ammonia on Ru(001)*, J. Chem. Phys. **88**, 5225 (1988).

[Pas03] J. I. Pascual, N. Lorente, Z. Song, H. Conrad, H.-P. Rust, *Selectivity in vibrationally mediated single-molecule chemistry*, Nature **423**, 525 (2003).

[Pay92] M. C. Payne, M. P. Teter, D. C. Allan, T. A. Arias, J. D. Joannopoulos, *Iterative minimization techniques for ab initio total-energy calculations: molecular dynamics and conjugate gradients*, Rev. Mod. Phys. **64**, 1045 (1992).

[Per92] J. P. Perdew, J. A. Chevary, S. H. Vosko, K. A. Jackson, M. R. Pederson, D. J. Singh, C. Fiolhais, *Atoms, molecules, solids, and surfaces: Applications of the generalized gradient approximation for exchange and correlation*, Phys. Rev. B **46**, 6671 (1992).

[Per96] J. P. Perdew, K. Burke, M. Ernzerhof, *Generalized Gradient Approximation Made Simple*, Phys. Rev. Lett. **77**, 3865 (1996).

[Pet99] V. F. Petrenko, R. W. Whitworth, *Physics of Ice*, Chapter 11, Oxford University Press, New York (1999).

[Pfn89] H. Pfnür, G. Held, M. Lindroos, D. Menzel, *Oxygen induced reconstruction of a close-packed surface: A LEED IV study on Ru(001)-p(2 × 1)O*, Surf. Sci. **220**, 43 (1989).

[Pus03] R. Pushpa, and S. Narasimhan, *Reconstruction of Pt(111) and domain patterns on close-packed metal surfaces*, Phys. Rev. B **67**, 205418 (2003).

[Qiu04] X. H. Qiu, G. V. Nazin, W. Ho, *Mechanisms of Reversible Conformational Transitions in a Single Molecule*, Phys. Rev. Lett. **93**, 196806 (2004).

[Qui01] P. Quinn, D. Brown, D. P. Woodruff, T. C. Q. Noakes, P. Bailey, *Structural analysis of the Ru(0 0 0 1)(1×1)-O and Ru(0 0 0 1)(2×1)-O structures by medium energy in scattering*, Surf. Sci. **491**, 208 (2001).

[Rep04] J. Repp, G. Meyer, F. E. Olsson, M. Persson, *Controlling the Charge State of Individual Gold Adatoms*, Science **305**, 493 (2004).

[San93] M. Sandhoff, H. Pfnür, H.-U. Everts, *Phase diagram and phae transitions in the system H/Ru(0001): a Monte Carlo study*, Surf. Sci. **280**, 185 (1993).

[San07] P. C. Sanfelix, S. Holloway, K. W. Kolasinski, G. R. Darling, *The structure of water on the (0001) surface of graphite*, Surf. Sci. **532**, 166 (2007).

[San08] B. Santra, A. Michaelides, M. Fuchs, A. Tkatchenko, C. Philippi, M. Scheffler, *On the accuracy of density-functional theory exchange-correlation functionals for H bonds in small water clusters. II. The water hexamer and van der Waals interactions*, J. Chem. Phys. **129**, 194111 (2008).

[Sch97] S. Schwegmann, A. P. Seitsonen, H. Dietrich, H. Bludau, H. Over, K. Jacobi, G. Ertl, *The adsorption of atomic nitrogen on Ru(0001): geometry and energetics*, Chem. Phys. Lett. **264**, 680 (1997).

[Sch98] F. Schwabl, *Quantenmechanik,* 5. Auflage, Springer, Berlin (1998).

[Sha08] A. Shavorskiy, M. J. Gladys, G. Held, *Chemical composition and reactivity of water on hexagonal Pt-group metal surfaces*, Phys. Chem. Chem. Phys. **10**, 6150 (2008).

[Sha09] A. Shavorskiy, T. Eralop, E.Ataman, C. Isvoranu, J. Schnadt, J. N. Andersen, G. Held, *Dissociation of water on oxygen-covered Rh{111}*, J. Chem. Phys. **131**, 214707 (2009).

[Shi07] T. Shimizu, *Water adsorption on Ruthenium (0001) Studied by Scanning Tunneling Microscopy*, Dissertation, UC Berkeley (2007).

[Shi08] T. K. Shimizu, A. Mugarza, J. I. Cerda, M. Heyde, Y. Qi, U. D. Schwarz, D. F. Ogletree, M. Salmeron, *Surface Species Formed by the Adsorption and Dissociation of Water Molecules on a Ru(0001) Surface Containing a Small Coverage of Carbon Atoms Studied by Scanning Tunneling Microscopy*, J. Phys. Chem. C **112**, 7445 (2008).

[Shi08b] T. K. Shimizu, A. Mugarza, J. Cerda, M. Salmeron, *Structure and reactions of carbon and hydrogen on Ru(0001): A scanning tunneling microscopy study*, J. Chem. Phys. **129**, 244103 (2008).

[Sok91] M. Sokolowski, F. Koch, H. Pfnür, *Ordered structures and phase diagram of atomic hydrogen chemisorbed on ruthenium (001)*, Surf. Sci. **243**, 261 (1991).

[Sol02] J. M. Soler, E. Artacho, J. D. Gale, A. García, J. Junquera, P. Ordejón, and D. Sánchez-Portal, *The SIESTA method for ab initio order-N materials simulation*, J. Phys.: Condens. Matter **14**, 2745 (2002).

[Son07] T. Song, P. Hua, *Insight into the adsorption competition and the relationship between dissociation and association reactions in ammonia synthesis*, J. Chem. Phys. **127**, 234706 (2007).

[Sta96] C. Stampfl, M. Scheffler, *Theoretical study of O adlayers on Ru(0001)*, Phys. Rev. B **54**, 2868 (1996).

[Sti97] B.C. Stipe, M.A. Rezaei, W. Ho, *Single-Molecule Dissociation by Tunneling Electrons*, Phys. Rev. Lett. **78**, 4410 (1997).

[Sti99] M. Stichler, D. Menzel, *A systematic investigation of the geometrical structures of four oxygen/nitric oxide coadsorbate layers on Ru(001)*, Surf. Sci. **419**, 272 (1999).

[Sti00] M. Stichler, C. Keller, C. Heske, M. Staufer, U. Birkenheuer, N. Rösch, W. Wurth, D. Menzel, *X-ray emission spectroscopy of NO adsorbates on Ru(001)*, Surf. Sci. **448**, 164 (2000).

[Str91] J. A. Stroscio, D. M. Eigler, *Atomic and Molecular Manipulation with the Scanning Tunneling Microscope*, Science **254**, 1319 (1991).

[Sut08] P. W. Sutter, J.-I. Flege, E. A. Sutter, *Epitaxial Graphene on Ruthenium*, Nat. Mat. **7**, 406 (2008).

[Sut09] P. Sutter, M. S. Hybertsen, J. T. Sadowski, E. Sutter, *Electronic Structure of Few-Layer Epitaxial Graphene on Ru(0001)*, Nano Lett. **9**, 2654 (2009).

[Tat08] M. Tatarkhanov, E. Fomin, M. Salmeron, K. Andersson, H. Ogasawara, L. G. M. Petterson, A. Nilsson, J. I. Cerdá, *The structure of mixed H_2O-OH monolayer films on Ru(0001)*, J. Chem. Phys. **129**, 154109 (2008).

[Tat08b] M. Tatarkhanov, F. Rose, E. Fomin,D. F. Ogletree, M. Salmeron, *Hydrogen adsorption on Ru(001) studied by scanning tunneling microscopy*, Surf. Sci. **602**, 487 (2008).

[Tat09] M. Tatarkhanov, D. F. Ogletree, F. Rose, T. Mitsui, E. Fomin, S. Maier, M. Rose, J. I. Cerdá, M. Salmeron, *Metal- and Hydrogen-Bonding Competition during Water Adsorption on Pd(111) and Ru(0001)*, J. Am. Chem. Soc. **131**, 18425 (2009).

[Ter83] J. Tersoff and D. R. Hamann, *Theory and Application for the Scanning Tunneling Microscope*, Phys. Rev. Lett. **50**, 1998 (1983).

[Ter85] J. Tersoff , D. R. Hamann, *Theory of the scanning tunneling microscope*, Phys. Rev. B **31,** 805 (1985).

[Thi82] P. A. Thiel, F. M. Hoffmann, W. H. Weinberg, *Coadsorption of Oxygen and Water on Ru (001): Vibrational and Structural Properties*, Phys. Rev. Lett. **49**, 501 (1982).

[Thi87] P. A. Thiel, T. E. Madey, *The Interaction of Water with Solid Surfaces: Fundamental Aspects*, Surf. Sci. Rep. **7**, 211 (1987).

[Thi05] M. M. Thiam, T. Kondo, N. Horimoto, H. S. Kato, M. Kawai, *Initial Growth of the Water Layer on (1 × 1)-Oxygen-Covered Ru(0001) in Comparison with that on Bare Ru(0001)*, J. Phys. Chem. B **109**, 16024 (2005).

[Tho06] G. Thomas, G. Parks, *Potential Roles of Ammonia in a Hydrogen Economy*, DOE study (2006).

[Thü08] K. Thürmer, N. C. Bartelt, *Nucleation-Limited Dewetting of Ice Films on Pt(111)*, Phys. Rev. Lett. **100**, 186101 (2008).

[Thü08b] K. Thürmer, N. C. Bartelt, *Growth of multilayer ice films and the formation of cubic ice imaged with STM*, Phys. Rev. B **77**, 195425 (2008).

[Tro96] J. Trost, T. Zambelli, J. Wintterlin, G. Ertl, *Adsorbate-adsorbate interactions from statistical analysis of STM images: N/Ru(0001)*, Phys. Rev. B **54**, 17850 (1996).

[Ver06] A. Verdaguer, G. M. Sacha, H. Bluhm, M. Salmeron, *Molecular structure of water at interfaces: Wetting at the nanometer scale*, Chem. Rev. **106**, 1478 (2006).

[Wan08] B. Wang, M.-L. Bocquet, S. Marchini, S. Gunther, and J. Wintterlin, *Chemical origin of a graphene moire overlayer on Ru(0001)*, Phys. Chem. Chem. Phys. **10**, 3530 (2008).

[Wei04] J. Weissenrieder, A. Mikkelsen, J. N. Andersen, P. J. Feibelman, G. Held, *Experimental evidence for a partially dissociated water bilayer on Ru{0001}*, Phys. Rev. Lett. **93**, 196102 (2004).

[Wid99] W. Widdra, T. Moritz, K. L. Kostov, P. König, M. Staufer, U. Birkenheuer, *Identification of a vibrational Stark shift within an adsorbate layer: NH_3 on Ru(001)*, Surf. Sci. **430,** L558 (1999).

[Wie94] R.Wiesendanger, *Scanning Probe Microscopy and Spectroscopy*, 1^{st} edition, Cambridge University Press (1994).

[Win09] J. Wintterlin, M.-L. Bocquet, *Graphene on metal surfaces*, Surf. Sci. **603**, 1841 (2009).

[Wit97] Chr. Wittneven, R. Dombrowski, S.H. Pan, R. Wiesendanger, *A low-temperature ultrahigh-vacuum scanning tunneling microscope with rotatable magnetic field*, Rev. Sci Instrum. **68**, 3806 (1997).

[Wu94] M. C. Wu, Q. Xu, and D. W. Goodman, *Investigations of Graphitic Overlayers Formed from Methane Decomposition on Ru(0001) and Ru(11$\bar{2}$0) Catalysts with Scanning Tunneling Microscopy and High-Resolution Electron Energy Loss Spectroscopy*, J. Phys. Chem. **98**, 5104 (1994).

[Yan08] S. Yan, J. Y. Lee, J. R. Hahn, *Electric Field Effect on the Vibration of Single CO Molecules in a Scanning Tunneling Microscope Junction*, J. Phys. Chem. B, **112**, 4731 (2008).

[Yan09] D.-S. Yang, A. H. Zewail, *Ordered water structure at hydrophobic graphite interfaces observed by 4D, ultrafast electron crystallography*, Proc. Nat. Acad. Sci. **106,** 4122 (2009).

[Zan04] R. Zangi, *Water confined to a slab geometry: a review of recent computer simulation studies*, J. Phys.: Condens. Matter **16**, S5371 (2004).

[Zha05] A. Zhao, Qu. Li, L. Chen, H. Xiang, W. Wang, S. Pan, B. Wang, X. Xiao, J. Yang, J.G. Hou, Q. Zhu, *Controlling the Kondo Effect of an Adsorbed Magnetic Ion Through Its Chemical Bonding*, Science **309**, 1542 (2005).

[Zha09] H. Zhang, Q. Fu, Y. Cui, D. Tan, and X. Bao, *Growth Mechanism of Graphene on Ru(0001) and O_2 Adsorption on the Graphene/Ru(0001) Surface*, J. Phys. Chem. C **113**, 8296 (2009).

[Zim06] G. Zimbitas, A. Hodgson, *The morphology of thin water films on Pt(111) probed by chloroform adsorption*, Chem. Phys. Lett. **417**, 1 (2006).